Bruno José Oliveira Santos
Licenciado em Ciências de Engenharia Civil

Coherent structures in open channel flows with bed load transport over an hydraulically rough bed

Dissertação para obtenção do Grau de Mestre em
Engenharia Civil – Perfil de Estruturas

Orientador: Professor Doutor Mário Jorge Rodrigues Pereira da Franca,
Professor Auxiliar,
Faculdade de Ciências e Tecnologia,
Universidade Nova de Lisboa

Co-orientador: Professor Doutor Rui Miguel Lage Ferreira,
Professor Auxiliar,
Instituto Superior Técnico,
Universidade Técnica de Lisboa

Júri:

Presidente: Professor Doutor Nuno Manuel da Costa Guerra
Arguente: Professor Doutor João Gouveia Aparício Bento Leal
Vogais: Professor Doutor Mário Jorge Rodrigues Pereira Franca
Professor Doutor Rui Miguel Lage Ferreira

FACULDADE DE CIÊNCIAS E TECNOLOGIA
UNIVERSIDADE NOVA DE LISBOA

Dezembro 2013

Coherent structures in open channel flows with bed load transport over an hydraulically rough bed

O caos é uma ordem por decifrar.

José Saramago

À Quirina

Aos meus pais José e Maria

Acknowledgements

O mérito não é estanque. É com esse pensamento que quero expressar a minha gratidão a todos quantos contribuiram para chegar aqui.

Quero começar por deixar o meu agradecimento ao orientador e co-orientador, respectivamente o Professor Mário Franca e o Professor Rui Ferreira.

Ao Professor Mário Franca agradeço a oportunidade e os ensinamentos, muitos transmitidos ainda antes de se pensar sequer que esta dissertação iria existir. Pela sua generosidade sempre presente, pelas suas indicações e principalmente por me apresentar esta incognita incrivel que é a hidráulica.

Ao Professor Rui Ferreira quero agradecer principalmente a sua confiança, disponibilidade em me acolher e por ter sido um guia essencial ao longo de todo o caminho. O seu rigor, método e sentido critico foram ferramentas imprescindiveis à conclusão desta dissertação.

Agradeço à Quirina por ser incansável no seu apoio, pela ajuda e motivação. Sem ti, nada disto seria possivel. És uma inspiração.

Aos meus pais José e Maria, eu devo tudo. Obrigado por acreditarem sempre, a vossa presença é inestimável.

O meu agradecimento vai também para toda a família, que esteve sempre presente na minha vida e foi parte integrante na minha formação pessoal. Entre todos destaco os meus irmãos Pedro e Helena, e incluo os mais novos, o André, o João e a Rita por serem sempre verdadeiros e me fazerem sorrir tantas vezes.

Não posso deixar de agradecer a amizade de todos aqueles que se têm cruzado no meu caminho. O Vitor pela pequena grande ajuda nas questões de programação, a Joana, o Ricardo, o Pedro e o António por serem sempre um grande apoio e por todos os bons momentos que passamos juntos. Ao Rodrigo, ao Sérgio e ao Jorge pelo companheirismo e pela amizade.

Agradeço também a todos aqueles que contribuiram para a minha formação. Ao longo do meu percurso académico cruzei-me com muitos professores em que cada um deu o seu contributo. É para eles que vai este meu agradecimento.

Deixo ainda o meu obrigado a todos os que de uma forma ou de outra têm contribuido para a formação de uma pessoa melhor.

Este trabalho de investigação foi financiado pela Fundação para a Ciência e Tecnologia através do projecto de investigação PTDC/ECM/099752/2008 e pelo Fundo de Europeu de Desenvolvimento Económico e Regional (FEDER) através do Programa Operacional Factores de Competitividade (COMPETE) FCOMP 01 0124 FEDER 009735.

Abstract

The degradation of forests through the impacts of devastating wildfires increase unprotected soils area which consequently favours soil erosion processes. The sediment production is continuously reaching water courses in these areas which may result in important impacts in the flow morphodynamics and hydrodynamics.

Sediment overfeeding induces important changes in the turbulent structure of the flow, mainly in momentum fluxes and exchange of momentum and mass between different layers in the flow structure, consequently affecting its ecological features.

Coherent structures play an important role on sediment transport and mixing processes which are important in the fluxes that govern the turbulent structure.

This study is aimed at evaluating the impacts of sediment transport on flow hydrodynamics, namely on the statistics characterizing coherent movements.

In order to accomplish the purposed objective, experimental tests were undertook in laboratorial environment where two-dimensional instantaneous flow velocity fields in both directions, streamwise and vertical, were measured through means of Particle Image Velocimetry (PIV) technique.

Two laboratory tests were simulated, consisting on a framework gravel bed with sand matrix and a framework gravel bed with sediment transport imposed at near capacity conditions. For both tests, the quadrant threshold analysis technique was employed and shear stress distribution statistics were analysed and discussed in what concerns their contribution and persistence.

The results show that, in the near bed region, mobile bed conditions make sweep events assume a major role in the shear stress production processes. Also, larger events become less frequent in the pythmenic region, comparing with the immobile bed results.

The impacts of mobile sediment in the near bed region over the flow structure are analysed and discussed in detail through probability density function distributions, in dimensional and non-dimensional data.

Keywords: bursting phenomena; coherent structures; quadrant threshold; PIV; sediment transport

Resumo

A degradação da floresta através de fogos florestais aumenta a área de solos desprotegidos, o que consequentemente é favorável aos processos de erosão do solo. A produção de sedimentos atinge continuamente os cursos de água existentes nessas áreas, o que resulta num impacto importante sobre os processos morfodinâmicos e hidrodinâmicos do escoamento.

O excesso de sedimentos introduz alterações importantes na estrutura turbulenta do escoamento, principalmente nos fluxos de momento e troca de momento e massa entre camadas do escoamento, afectando as suas caracteristicas ecológicas.

As estruturas coerentes têm um papel importante no transporte de sedimentos e processos de mistura que se revelam importantes nos fluxos que controlam a estrutura turbulenta.

Este estudo foca-se na avaliação do impacto que o transporte de sedimentos tem na hidrodinâmica do escoamento, tal como nas estatisticas que caracterizam dos movimentos coerentes.

Visando atingir o objectivo proposto, foram efectuados ensaios em ambiente laboratorial, em que foram medidos campos bidimensionais de velocidade instantânea de escoamento nas direcções longitudinal e vertical, através da técnica *Particle Image Velocimetry* (PIV).

Foram efectuadas duas experiências laboratoriais, uma sobre um leito composto por uma estrutura de seixo com uma matriz de areia e uma outra nas mesmas condições com excepção do facto de haver imposição de transporte de sedimentos. Para ambos os ensaios, foi aplicada a técnica de análise de quadrante e foram analisadas as estatisticas de distribuição da tensão de corte de Reynolds em que foi discutida a sua contribuição e persistencia.

Os resultados mostram que, na região junto ao leito, as condições de leito movél levam a que os eventos de varrimento assumam um papel preponderante na geração de tensão de corte de Reynolds. E também, que eventos de maior escala tornam-se menos frequentes na região pythménica, em comparação com os resultados do leito imóvel.

O impacto da existência de sedimentos móveis, na região junto ao leito, sobre a estrutura do escoamento são analisados em detalhe através de distribuição de função de densidade de probabilidade, para o caso de dados dimensionais e adimensionais.

Palavras-chave: fenómeno bursting; estruturas coerentes; análise de quadrantes; PIV; transporte de sedimentos

Contents

List of Tables

List of Figures

Simbology

Symbol	Description	Dimension
A	Maximum shear stress	$[L^2T^{-2}]$
A_k	Maximum shear stress of event k	$[L^2T^{-2}]$
C_{xk}	Centroid abscissa of each event in the Quadrant threshold analysis method	$[-]$
d_p	Average diameter of the tracer particles	$[L]$
$d_{50}^{(g)}$	Mean diameter of gravel	$[L]$
$d_{50}^{(s)}$	Mean diameter of sand	$[L]$
Fr	Froude number	$[-]$
F_c	Calibration factor	$[-]$
f_A	Normalization factor of maximum shear stress based on average shear stress, $\lvert u\prime w\prime \rvert$	$[-]$
f_{A^*}	Normalization factor of maximum shear stress based on friction velocity, u^*	$[-]$
f_c	Frequency of turbulent structures	$[T^{-1}]$
f_M	Normalization factor of transported momentum based on average shear stress, $\lvert u\prime w\prime \rvert$	$[-]$
f_{M^*}	Normalization factor of transported momentum based on friction velocity, u^*	$[-]$
f_P	Normalization factor of period based on average shear stress, $\lvert u\prime w\prime \rvert$	$[-]$
f_{P^*}	Normalization factor of period based on friction velocity, u^*	$[-]$
g	Absolute gravity acceleration	$[LT^{-2}]$
H	Hole size variable	$[-]$
h	Flow depth	$[L]$
h^*	Reference flow depth for shear stress calculation	$[-]$
h_b	Bins size in the histograms	$[-]$
i	bed slope	$[-]$
k_s	Characteristic roughness height	$[L]$
M	Transported momentum	$[L^2T^{-1}]$
M_k	Transported momentum of event k	$[L^2T^{-1}]$
m	Vertical index in flow velocity fields	$[-]$
N_{maps}	Number of maps collected for each run	$[-]$
n	Horizontal index in flow velocity fields	$[-]$
P	Period	$[T]$
P_c	Period of event k measured between consecutive centroids	$[T]$
P_m	Period of event k measured between consecutive maximums	$[T]$
P_k	Period of event k	$[T]$
$P_{x,i}$	Abscissa from a generic point i in the calibration board and measured in pixel	$[T]$
$P_{y,i}$	Ordinate from a generic point i in the calibration board and measured in pixel	$[T]$

Symbol	Description	Dimension
Q	Flow discharge	$[L^3T^{-1}]$
q_n	Characteristic normalized diameter of light scattering by seeding	$[-]$
q_b	Volumetric sediment discharge	$[[L^3T^{-1}]]$
R^*	Hydraulic radius	$[-]$
Re	Reynolds number	$[-]$
Re^*	Reynolds number characteristic of roughness	$[-]$
r_p	Rate which measures the ability of tracer particles to follow the moving flow	$[-]$
s	Slope of the function	$[-]$
s_k	Stokes number	$[-]$
T	Duration	$[T]$
T_f	Final temperature of the experimental test	$[\theta]$
T_i	Initial temperature of the experimental test	$[\theta]$
T_k	Duration of event k	$[T]$
T_p	Period of turbulent structures	$[T]$
t	Time	$[T]$
U	Depth averaged mean flow velocity in longitudinal direction	$[LT^{-1}]$
u	Longitudinal flow velocity	$[LT^{-1}]$
u^*	Friction Velocity	$[LT^{-1}]$
u_i	Longitudinal flow velocity at a particular point i in the velocity field	$[LT^{-1}]$
u_{rms}	Longitudinal turbulent intensity	$[LT^{-1}]$
$\bar{u}$	Average longitudinal flow velocity	$[LT^{-1}]$
u'	Fluctuation of the vertical flow velocity	$[LT^{-1}]$
u'_i	Fluctuation of the longitudinal flow velocity at a particular point i in the velocity field	$[LT^{-1}]$
$\lvert u'w' \rvert$	Shear stress	$[L^2T^{-2}]$
V	Absolute flow velocity	$[LT^{-1}]$
V_p	Absolute particle velocity	$[LT^{-1}]$
V_sp	Settling velocity	$[LT^{-1}]$
w	Vertical flow velocity	$[LT^{-1}]$
w_i	Vertical flow velocity at a particular point i in the velocity field	$[LT^{-1}]$
w_{rms}	Vertical turbulent intensity	$[LT^{-1}]$
$\bar{w}$	Average vertical flow velocity	$[LT^{-1}]$
w'	Fluctuation of the vertical flow velocity	$[LT^{-1}]$
w'_i	Fluctuation of the vertical flow velocity at a particular point i in the velocity field	$[LT^{-1}]$
x	Longitudinal coordinate	$[-]$
z	Vertical coordinate	$[-]$
Z	Distance to the wall	$[L]$
Z_b	Boundary zero	$[L]$
Z_f	Elevation of impermeable floor supporting particles	$[L]$
Z_L	Elevation of upper bound of logarithmic layer	$[L]$
Z_R	Elevation of lower bound of logarithmic layer or upper bound of roughness layer	$[L]$
Z_s	Elevation of the free-surface	$[L]$
Z_t	Elevation of the deepest through	$[L]$
Z_{ws}	Water elevation	$[L]$

Symbol	Description	Dimension
Z_0	Elevation of the zero of the log-law	$[\mathrm{L}]$
δ	Pythmenic region thickness	$[\mathrm{L}]$
Δd_i	Particle displacement	$[\mathrm{L}]$
Δm	Distance between a pair of points in the calibration board in pixel	$[\mathrm{L}]$
Δp	Distance between a pair of points in the calibration board in meter	$[\mathrm{L}]$
Δt	Time between pulses in PIV technique	$[\mathrm{T}]$
δt	Time between pairs of images in PIV technique	$[\mathrm{T}]$
Δu_i	Derivative of the longitudinal flow velocity at a particular point i in the velocity field	$[-]$
Δx	Distance between a pair of points in the calibration board in the abscissas measured in meters	$[\mathrm{L}]$
Δy	Distance between a pair of points in the calibration board in the ordinates measured in meters	$[\mathrm{L}]$
ζ	Scaling constant	$[-]$
η	Non-dimensional height	$[-]$
θ_R	Rotation angle used to build ellipses in the Phase-space thresholding method	$[\theta]$
λ_b	Bed porosity	$[-]$
λ_l	Wavelength of incident light	$[\mathrm{L}]$
λ_t	Wavelength of turbulent structures	$[\mathrm{L}]$
λ_U	Universal threshold on the Phase-Space thresholding method	$[-]$
μ	Water dynamic viscosity	$\left[\mathrm{ML^{-1}T^{-1}}\right]$
ν	Water kinematic viscosity	$\left[\mathrm{L^2T^{-1}}\right]$
ν^g	Shields parameter of gravel	$[-]$
ν^s	Shields parameter of sand	$[-]$
ρ_f	Fluid density	$\left[\mathrm{ML^{-3}}\right]$
ρ_p	Tracer particles density	$\left[\mathrm{ML^{-3}}\right]$
$\rho^{(w)}$	Water density	$\left[\mathrm{ML^{-3}}\right]$
σ	Generic standard deviation	$[-]$
$\sigma_D^{(g)}$	Geometric standard deviation of gravel diameter	$[-]$
$\sigma_D^{(s)}$	Geometric standard deviation of sand diameter	$[-]$
σ_h	Threshold of the quadrant threshold method	$\left[\mathrm{L^2T^{-2}}\right]$
σ^-	Negative threshold of the quadrant threshold method	$\left[\mathrm{LT^{-1}}\right]$
σ^+	Positive threshold of the quadrant threshold method	$\left[\mathrm{LT^{-1}}\right]$
τ	Characteristics response time	$[\mathrm{T}]$
τ_t	Characteristics flow time scale	$[\mathrm{T}]$
τ_0	Total shear stress	$\left[\mathrm{ML^{-1}T^{-2}}\right]$
$\tau_0^{(1)}$	Total shear stress calculated by the equation of conservation of momentum	$\left[\mathrm{ML^{-1}T^{-2}}\right]$
$\tau_0^{(2)}$	Total shear stress calculated by the total shear stress profile	$\left[\mathrm{ML^{-1}T^{-2}}\right]$
φ	Void characteristic length	$[-]$
$\varphi(z)$	Void function	$[-]$
φ_m	Mean value of the void function	$[-]$
Ω	Area inside the polygon that defines each event	$\left[\mathrm{L^2T^{-2}}\right]$

Acronyms

Acronym	Description
ADV	Acoustic Doppler Velocimetry
CCD	Charge-couple device
CPU	Central Processing Unit
CRIV	Recirculating tilting flume
DTM	Digital Terrain Model
FFT	Fast Fourier Transform
IS	International System
LDA	Laser Doppler Anemometry
PIV	Particle image velocimetry
PNDFCI	National Plan to defend forest against wild fires
PSP	Polyamide Seeding Particles
PVC	Polyvinyl Chloride
SHG	Second Harmonic Generator
2D	Two dimensional
3D	Three dimensional
YAG	Yittrium Aluminium Garnet

Chapter 1

Introduction

1.1 Motivation

Every year, Portugal has been the scene of severe forest fires that keep on destructing ecosystems and the forest itself . According to the Portuguese PNDFCI (National plan to defend forest against wild fires) report, the burnt area has been increasing for the last 25 years. Solely during the summer of 2003, around 425 000 ha of forest were burnt in Portugal. The problem of wildfires represents important expenses in fire-fighting but also with economic, social and environmental impacts, including the loss of human lives.

Forest fires contribute to the natural regeneration process in several ecosystems, by providing a recharge of nutrients into the soil and stimulating the biodiversity (Dawson et al., 2002), however, it also contributes to the degradation of other ecosystems, such as salmonids habitats.

The subsequent change in the topsoil layer due to forest fires impacts on the water resources widely involved in the hydro-geological cycle.

The salmonids, as an example, depend on the dissolved oxygen in the river flow to promote their habitats and reproduction cycle. Oxygen is carried from the surface through turbulent events and then transported to the salmodids eggs by the sub superficial flow which is controlled by the near bed pressure (Ferreira et al., 2010).

Forest fires promote soil erosion which lead to an increasing of sediments reaching rivers. These sediments interact with the flow and have an impact over the processes that govern it.

It is of scientific interest to characterize the impacts of sediment overfeeding over the stream, as the sediment bed load transport which is related to the salmonid habitat.

1.2 Objective

The purpose of this work is to understand coherent structures that govern the flow when in bed-load sediment transport conditions and along the water column. Organized turbulence is going to be compared between hydraulically rough mobile and immobile porous boundaries.

A statistical characterization of the events occurring in four quadrants of the longitudinal plane must be performed in order to study their preponderance in the sediment transport phenomena and

to find a pattern in the event magnitude under these same conditions.

1.3 Methodology

Prior to this research work, several laboratorial experiments were undertaken by Ferreira (2008) and Amatruda (2009). These experiments lead to instantaneous flow velocity data acquired in two orthogonal directions and for two different sets of conditions, recurring to the PIV technique. The initial data comprises instantaneous displacement maps for open-channel flow with and without bed-load transport.

To eliminated spurious data, the instantaneous flow displacement maps are processed using the Phase-Space thresholding method, which was developed by the Goring and Nikora (2002) and later modified by Ferreira et al. (2009). Then it is applied a sensitivity study of transported momentum to the hole size, obtaining the threshold to be used.

Ejection and sweep events must be considered such as the parameters that characterize them. The parameters that characterize these events such as, time persistence of the event, event shear stress, event transported momentum and period between consecutive events, are then computed.

Later, the computed parameters are subjected to a statistical approach aiming to ease its analysis and complete comprehension.

Such results are analysed and discussed, especially focusing on the bed roughness effect and the bed-load transport in the roughness dominated layer in open-channel flow conditions.

1.4 Thesis outline

This thesis is developed in seven chapters. It starts with this chapter where motivation, objective and methodology are presented. The remaining chapters are described as follows:

- Chapter 2 starts by introducing the sediment transport phenomena and follows characterizing the physical system of the flow by explaining how the flow is layered according to its behaviour. An incursion in the coherent structures and bursting phenomena is performed by exposing the phenomena itself and explaining how previous research works in hydrodynamics were conducted along the years.

- Chapter 3 describes the particle image velocimetry method, which is the technique used to achieve the data used in this research work. It initiates with a general description of the method and follows focusing on the most important variables that have to be accounted like correlation methods, its main error sources and the characteristics of the tracer particles, which is a particularly important feature due to its scattering of light properties.

- Chapter 4 describes the laboratory facilities, focusing on the CRIV - Recirculating Tilting

Flume. A detailed description of the instrumentation is also presented.

- In chapter 5 the laboratory experiments are described, such as bed surface and topography. Void distribution and mean flow characteristics are also presented, with detail over the calculations to achieve these indirect characteristics. It also resumes how the data is organized and follows describing how it is analysed, focusing on the filtering method and calibrations. Finally the data treatment is described, with particular attention due to the event detection, data interpolation and event statistics.

- The results are presented in chapter 6. It starts with a description and a map of the chosen positions where the flow is analysed and continues presenting the results of the sensitivity analysis of the transported momentum to the variation of the hole size. Finally, histograms of the analysed parameters are presented, firstly in its real values and then using non-dimensional values eliminating the influence of the total shear stress which is different in both experiments, respectively with and without sediment transport in the near wall region.

- Finally, chapter 7 presents a set of conclusions that can be achieved by analysing the results. It also enumerates a group of comments and ideas to help continuing this research work.

Chapter 2

Organized turbulence in open-channel flows

2.1 Introduction

Throughout the geological time, natural processes have been continuously reshaping the landscape through processes of erosion, transport and sediment deposition.

Sediment transport plays an important role in rivers by providing them a way of being continuously reshaped by their own content. The knowledge and the control over the sediment transport is a matter of extreme interest due to its importance in preventing catastrophes, or simply improving ways of living by controlling floods and providing improvements in management systems to river basins.

Sediments are suitable of being transported in river streams by two main modes which encloses bed-load or suspended-load transport. In the suspended load case, particles are usually finer and carried by fluid turbulence in the flow section. On the contrary, in the bed-load case, particles always stay in contact or very close to the bed and are propelled by rolling and sliding processes.

This thesis is completely focused on sediment bed-load transport in a poorly sorted gravel-bed armoured with sand.

To accomplish the proposed objective, conditions similar to those found in nature, in what concerns flow and bed material, were reproduced in a laboratory flume and 2D instantaneous velocity fields (streamwise and vertical directions) were measured by means of Particle Image Velocimetry (PIV) technique.

Flow velocity fields allow to characterize the flow in what concerns the statistics of the several features that complete the bursting phenomena, which is crucial to study the morphodynamics and hydrodynamics of rivers.

2.2 The bursting phenomena

Bursting phenomena results from a class of coherent structures occurring mainly in the near wall region. It results from a quasi-cycle process that is composed of interactions in the four quadrants, which are sweep and ejection events, respectively in the fourth and second quadrant, mediated by outward and inward events, respectively in the first and third quadrants. These phenomena are responsible for the essential mechanism of generating turbulent energy and shear stress.

The introduction of innovative experimental methods such as hydrogen-bubble technique and hot wire measurements with dye visualization lead to the pioneering works of Kline et al. (1967) and Kim et al. (1971) in the scope of mechanical engineering and later as a subject of civil engineering by Grass (1971).

During these experiments, coherent structures were firstly identified by observing particularly well-organized motions in the laminar layer. Particular attention was due to the near-wall region observing streaks that interact with the outer region of the flow enabling energy and momentum fluxes. These transfers happen through a gradual process of lift-up, oscillation, sweeping and ejection (Kline et al., 1967). Previously, Corino and Brodkey (1969) had estimated the persistence of ejection events, concluding that it contributes to 50 to 70% of the total local Reynolds stress in the near-bed region of a smooth boundary.

Grass (1971) observed that both sweep and ejection events are responsible for the majority of the contribution to the Reynolds stress close to the boundary layer. He also stated that the frequency of sweep events increases with the roughness of the boundary layer. It was then concluded by Grass (1971) that ejections are more contributive than sweep events to the production of shear stress, although the later increases their contribution under rough bed conditions.

Nakagawa and Nezu (1977) made a prediction of the contribution of each sort of event to the process of shear stress production. To achieve that in terms of quantitative results, it was used the quadrant threshold method which will be applied in the scope of the present work and that was developed by Willmarth and Lu (1972) and Lu and Willmarth (1973) when they studied the same phenomena in a wind tunnel. These experiments confirmed the results of Grass (1971), where it was noticed that sweep events become more frequent when the bed roughness is increased.

Major advances were made in sediment transport research with the works of Gyr and Schmid (1997) using Laser Doppler Anemometry (LDA) measurements over a smooth sand bed. This research work concluded that the presence of intense intermittent sediment transport increases the extreme values of shear stress while the flow becomes more organized in the second and fourth quadrants, mainly increasing the importance of sweep events to turbulence production. The period between events of the second and fourth quadrants decreases considerably in the presence of sediment transport, producing more frequent ejection and sweep events.

Results from Sechet and Le Guennec (1999) show also that the bursting phenomena is responsible for bed load sediment transport. However, there is not a clear evidence on the importance of each sort of events, namely, ejection and sweep events.

More recent results using applications of LDA and PIV, such as those of Ferreira et al. (2009), have been completing the knowledge over sediment transport. The work of Ferreira et al. (2009) introduces improvements in the quadrant threshold analysis which is explained in detail in chapter

2.4 as it was applied in the scope of the present work. It compares the organized turbulence in mobile and immobile bed conditions over a rough boundary, using LDA which operates at a frequency of 240 Hz and which could not clarify if the increasing mobility of sediments is a cause or an effect of the increasing intensity of the coherent structures.

2.3 The physical system

2.3.1 Interactions in the boundary layer

Boundary layer theory is important to explain the behaviour of the flow over a surface, whether it is an hydraulically smooth or rough walled boundary.

Whenever a fluid is in contact with a solid boundary, there is a thin layer of water that goes from still water to the mean flow velocity in the upper region of the same layer (Schlichting, 1968). This is denominated by boundary layer and because it presents a high rate of increase in the fluid velocity, it is extremely important in the shear stress production processes. The boundary layer thickness is considered to be the region in which the fluid velocity increases from zero, at the surface of the obstacle, to 99% of the external mean flow velocity.

The boundary layer over a rough bed may be characterized as either, laminar or turbulent. The classification of hydraulically smooth or rough flow is applied when in turbulent conditions.

In laminar flow conditions, all rough walls produce the same resistance as the equivalent smooth wall. Although the flow is turbulent, it may behave as smooth walled if within a certain range of Reynolds numbers or as hydraulically rough when higher Reynolds numbers dominate the stream (Campbell, 2005). There is also a transitional layer controlled by intermediate Reynolds numbers, between the hydraulically smooth and the rough walled conditions. Table 2.1 shows the relation between the regime that dominates in the boundary layer and the set of Reynolds numbers, Re^*, that characterise it.

Tabela 2.1: Boundary layer regime and the correspondent Reynolds numbers (Re^*) that characterise it (Nezu and Nakagawa, 1993).

Regime	Reynolds numbers
Hydraulically smooth	$0 \leq Re^* \leq 5$
Intermediate regime	$5 \leq Re^* \leq 70$
Hydraulically rough	$70 \leq Re^*$

The hydraulically smooth regime occurs when all protrusions are kept inside the viscous sub-layer, whose thickness scale is the ratio between kinetic viscosity and friction velocity, $\frac{\nu}{u^*}$, while in the rough walled regime, all protrusions reach the outside of the laminar sub-layer and the flow resistance becomes quadratic, being mostly produced by form drag. As stated before, the intermediate regime presents some protrusions outside the laminar sub-layer and a small resistance is produced by form drag (Schlichting, 1968).

2.3.2 Layering the flow

Nikora et al. (2001) proposed a layering system applied to the flow field in open-channels which is composed of five flow layers. This was based on the system previously defended by Nezu and Nakagawa (1993) in which the open-channel flow was divided in three layers, namely, *(i)* wall region layer, *(ii)* free-surface region layer and *(iii)* intermediate region layer. This is a simple model as it considers that there is a region where the wall governs the flow, while in the opposite region it is governed by the free-surface. The intermediate region is where both influences are noticed.

Based on an approach considering the double-average methodology, Nikora et al. (2001) proposed two layering systems, for impermeable beds and for permeable beds, respectively shown in Fig. 2.1 and Fig. 2.2.

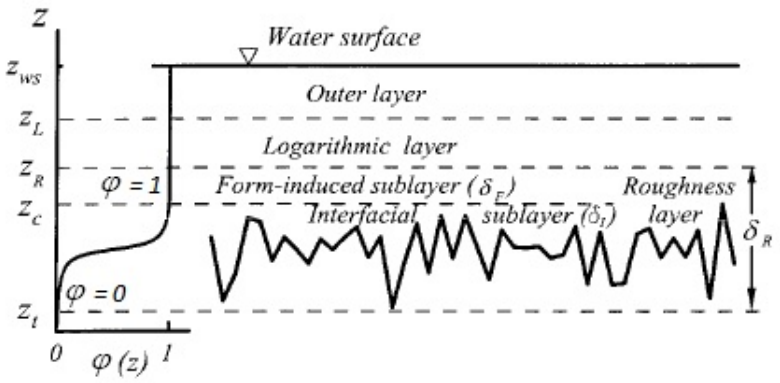

Figure 2.1: Layering system proposed by Nikora et al. (2001) for impermeable rough beds in open-channel flow conditions. Z stands for the distance to the bed, z_c stands for the elevation of highest roughness crests, Z_f is the elevation of impermeable floor supporting particles, Z_L is the elevation of upper bound of logarithmic layer, Z_R is the elevation of lower bound of logarithmic layer, z_t is the elevation of the deepest through, Z_{ws} stands for free surface elevation and φ is the void function.

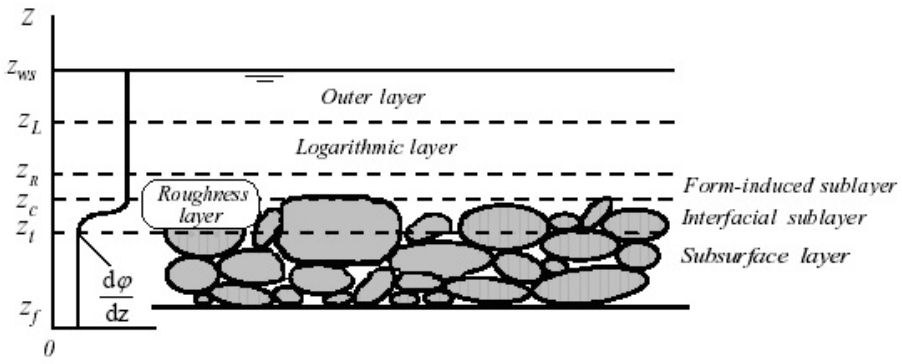

Figure 2.2: Layering system proposed by Nikora et al. (2001) for permeable rough beds in open-channel flow conditions.

(i) Subsurface layer

This layer is particular for permeable beds and it confines the region where the flow occurs due to the permeability of the bed. Its scales lay on the friction velocity, u^*, and the void characteristic length, φ, and is being driven essentially by gravity forces in cooperation with the flow from the

overlaying layers. The upper limit of this layer stands where $\frac{d\varphi}{dz} = 0$ with $\varphi(z)$ representing the void function. In this region the void function, φ, stands between 1 at its top and the bed porosity, λ_b at the bottom.

(ii) Interfacial sub-layer

The interfacial sub-layer is placed between the lowest trough, z_t, and the highest crest, z_c and its thickness is defined by $\delta = z_c - z_t$. In this sub-layer the void function, $\varphi(z)$, varies from 1 to 0 in impermeable bed conditions and from 1 to λ_b in permeable bed conditions. While the viscous stresses stand negligible, the flow is governed by Reynolds and form-induced stresses.

The characteristic scales that govern the flow in this sub-layer are the friction velocity, u^*, and the characteristic length of the bed topography.

(iii) Form-induced sub-layer

The form-induced sub-layer owes its name to the form-induced stress that governs the flow in this region where pressure and viscous drag reach zero. As this sub-layer stands right above the highest crests level, it is indirectly influenced by the roughness due to the flow separation from the rough elements standing in the interfacial sub-layer.

It is considered that both, the interfacial sub-layer and the form-induced sub-layer result in the roughness layer because it is highly influenced by the roughness of the bed.

(iv) Logarithmic layer

The logarithmic layer owes its name to the logarithmic formula, which is followed by the distribution of the longitudinal flow velocity, u. However, the existence of this layer demands that the flow depth is much greater than the characteristic roughness height, $h >> k_s$. According to Raupach et al. (1991) and Nezu and Nakagawa (1993), the logarithmic layer is placed in the flow region delimited by $(2to5)k_s \leq z - z_t \leq 0.2h$. The flow in this layer presents similarities with the same layer in smooth or hydraulically smooth bed conditions.

At this level, as in the outer layer, the viscous effects and the bed roughness effects are neglected. However, the characteristic scales are different form those in the outer layer, as they are the distance from the bed, z, the friction velocity, u^*, and a set of characteristic scales of the bed topography.

(v) Outer layer

Because the outer layer is in the near-surface region, the flow in this layer is highly governed by the influence of the air, rather than the wall. That is why the flow presents a similar behaviour in both rough or smooth wall boundary conditions and the viscous effects and the direct effects of the bed roughness are negligible.

The characteristic scales in the outer layer are the maximum flow velocity, U_{max}, friction velocity, u^*, flow depth, h, and the distance from the bed.

The presence of coarse sediment entrained in the flow introduces some differences in the stream structure. Due to this, Ferreira et al. (2008) proposed a new model based on the one defended by Nikora et al. (2001), but more suitable for bed-load conditions over a rough wall.

This system was then subjected to improvements undertook by the same author in order to achieve a better fit to the characteristics of the flow in the same conditions. The proposed model presents characteristics comparable to the system proposed by Nezu and Nakagawa (1993), keeping the same three regions, in which the intermediate region results from the overlapping between both outer and inner regions and where log-law is valid. Both pythmenic and hyporeic regions are also introduced in the near wall region as previously proposed by Ferreira et al. (2008).

The main particularity in this model is that the layering boundaries become flexible as the flow is divided in four regions where overlapping regions are considered between each neighbouring pair. The main reason to support this model is that the phenomena that characterizes it does not ceases to exist abruptly, but through a region where characteristics from both layers co-exist. Fig. 2.3 represents this flexible model proposed by Ferreira et al. (2012).

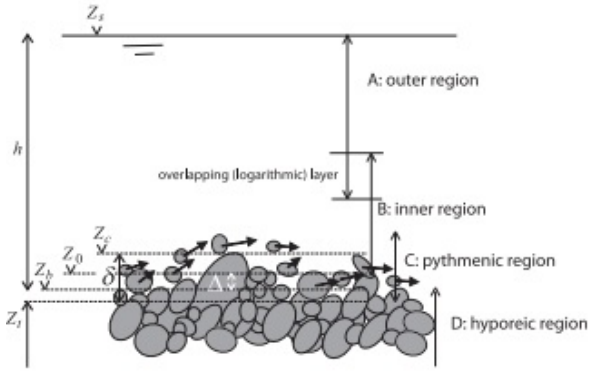

Figure 2.3: Flow structure proposed by Ferreira et al. (2012) for permeable rough beds with sediment bed-load in open-channel conditions. h stands for the flow depth, Z_b stands for the boundary zero elevation, Z_c stands for the highest crest elevation, Z_s stands for the elevation of the free-surface and Z_t is the elevation of the deepest through

As previously stated, the outer layer congregates the same characteristics as the ones described in the model proposed by Nikora et al. (2001).The inner region is comprises the same characteristics of the form-induced sub-layer and the logarithmic layer. In this region, the flow is directly governed by the bed roughness in its lowermost region and indirectly in its uppermost region, where the profile of the longitudinal flow velocity is logarithm.

The overlapping between both outer and inner regions results in the logarithmic region, as the vertical profile of the longitudinal velocity logarithmic and it is governed by characteristics from both neighbouring regions.

Layers in the near-wall region are described in detail as followed:

Pythmenic region

The flow in the pythmenic layer is governed by the wall micro-topography. The overlapping

region between pythmenic and inner layers results in a region at the highest crests elevation where the interaction between characteristics from both regions ignites strong momentum fluxes in vertical direction.

The porosity at the bottom of this layer is the bed porosity, λ_b, and it reaches the maximum value of 1 at the top of the layer.

Hyporeic region

The hyporeic region is placed below the pythmenic layer where the flow depends on the void function, that will be described in chapter 5.2.2. The hydraulic gradient, acceleration of gravity and fluid viscosity and density are the remaining factors that govern the flow in this region. The region composed of both hyporeic and pythmenic regions can be described as the roughness region.

2.4 Quadrant threshold analysis

Along years of investigation in river flow hydrodynamics several methods of analysis have been continuously developed by investigators to improve knowledge on the structure of the flow.

The conditional sampling and detection criterion applied in the scope of this thesis is the quadrant threshold analysis, regarding its conceptual simplicity. This technique is described in Ferreira (2008) which is based on previous works developed in the second half of the last century by Corino and Brodkey (1969), Willmarth and Lu (1972), Lu and Willmarth (1973), Nakagawa and Nezu (1977) and detailed in Nezu and Nakagawa (1993).

The method itself is based on the fluctuation of the instantaneous flow velocity fields, represented by u' and w', respectively corresponding to the two orthogonal components of the flow. This is calculated by subtracting the mean flow velocity, from the instantaneous flow velocity values measured during the experiments, as shown by equations 2.1 and 2.2.

$$u_i' = u_i - \overline{u} \tag{2.1}$$

$$w_i' = w_i - \overline{w} \tag{2.2}$$

where u' and w' are the flow velocity fluctuation, respectively in the longitudinal and vertical directions. The $\overline{u}$ and $\overline{w}$ are the mean flow velocities in both longitudinal and vertical directions while u and w stand for the instantaneous flow velocities measured during experiments.

The quadrant threshold analysis technique initiates by plotting the u', longitudinal flow velocity fluctuation, against the w', vertical flow velocity fluctuation, and then separating the events based upon the quadrant where they occur. The relative contribution of the flow velocity in each direction to the shear stress is distributed in four quadrants.

Based on that, an outward event is represented in the first quadrant and occurs when $(u' > 0 \wedge w' > 0)$, an ejection event appears in the second quadrant and occurs when $(u' < 0 \wedge w' > 0)$, an inward event stands in the third quadrant and occurs when $(u' < 0 \wedge w' < 0)$ and a sweep event occurs in the fourth quadrant with $(u' > 0 \wedge w' < 0)$.

An example of the instantaneous flow velocities fluctuation is shown in figure 2.5.

To neglect the symmetrical data that occurs inside a certain nutshell centred in the Cartesian referential origin, a threshold must be considered. This threshold establishes a filter to consider only the important data, outside of the hole region, mainly resulting from ejection and sweep events. It is represented by σ_h and its absolute value is kept in all four quadrants.
Equation 2.3 shows how σ_h is calculated.

$$\sigma_h = H \times u_{rms} \times w_{rms} \tag{2.3}$$

where H is the value that controls the hole size and the turbulent intensities associated to the longitudinal and normal directions, are respectively represented by u_{rms} and w_{rms}. The u_{rms} and w_{rms} are achieved using equation 2.4.

$$x_{rms} = \sqrt{\frac{1}{n} \times \sum_{n} x^2} \tag{2.4}$$

where x represents the velocity in a generic direction and n represents the dimension of the sample.

This can be also represented in time series, where the $u'w'$ is plotted against time, resulting in a better visualization of the events but making it hard to identify which kind of event is represented in the series. This can be solved by joining the u', w' and $|u'w'|$ in the same time series and according to the visualization of these three time series it is then possible to correctly identify every single event, as it is shown in figure 2.4.

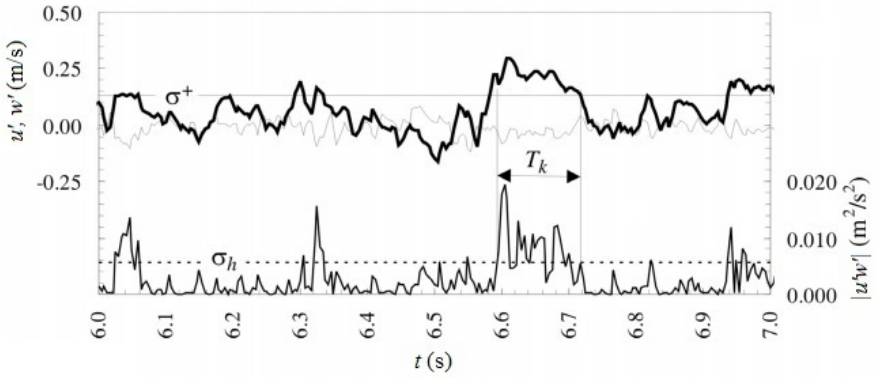

Figure 2.4: Top: Detail of u' and w'. Bottom: Detail of $|u'w'|$ (Ferreira et al., 2009).

In order to avoid discarding important events that appear in the data as a sequence of minor events some improvements have to be performed. This problem cannot be solved by reducing the threshold hole size because it would only allow to the correct identification of large events, however it would not prevent the incorrect inclusion of small events that are only simple oscillations due to the isotropic turbulence.

The method applied in the scope of this thesis remains attached to the modified proposal of Ferreira et al. (2009). It is focused on the observation that the persistence of u' above a certain threshold is well correlated with the persistence of the event. Figure 2.4 elucidates this issue, where it can be observed that there are a set of events within a short time interval, around 6.6 s to

6.7 s, which in normal conditions would be considered as independent events. Although, in the same time interval it is also observed that the value of u' is kept at high values, above a certain threshold. This is the criteria to aggregate all events occurring during this same time interval into a single event.

Based on that, Ferreira et al. (2009) establishes a vertical threshold σ^- if $u^{'} < 0$ and σ^+ if $u^{'} > 0$ in the quadrant analysis plot, when using data acquired by Acoustic Doppler Velocimetry (ADV). Equations 2.5 and 2.6 show how these values are calculated and figure 2.5 shows graphically the threshold system used over the flow velocity fluctuation data.

$$\sigma^+ = 2.5 \times u_{rms} \tag{2.5}$$

$$\sigma^- = -2.5 \times u_{rms} \tag{2.6}$$

It is commonly adopted that $\sigma_h = \sigma_h^I = \sigma_h^{II} = \sigma_h^{III} = \sigma_h^{IV}$ and the domains that identify the occurrence of each event are described as:

- Outward interactions: $Q_{out} = \{u', w' \in \mathbb{R} : u' > 0 \wedge w' > \frac{\sigma_h}{u'} \wedge u' < \sigma^+\}$;
- Ejection interactions: $Q_{ej} = \{u', w' \in \mathbb{R} : u' < 0 \wedge \{w' > \frac{\sigma_h}{|u'|} \vee u' < \sigma^-\}\}$;
- Inward interactions: $Q_{in} = \{u', w' \in \mathbb{R} : u' < 0 \wedge w' < 0 \wedge |w'| > \frac{\sigma_h}{|u'|} \wedge u' > \sigma^-\}$;
- Sweep interactions: $Q_{sw} = \{u', w' \in \mathbb{R} : u' > 0 \wedge \{\{w' < 0 \wedge |w'| > \frac{\sigma_h}{u'}\} \vee u' > \sigma^+\}\}$.

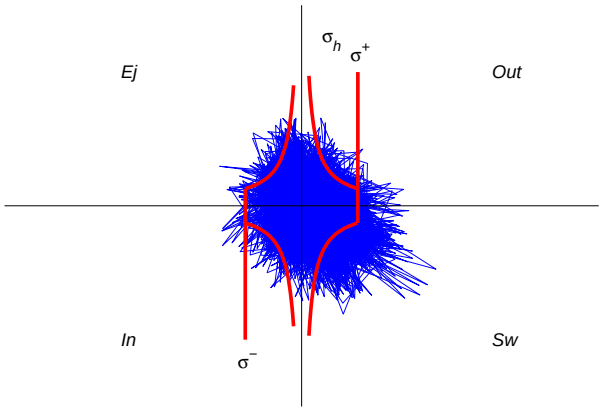

Figure 2.5: Example of a quadrant plot of the instantaneous flow velocity with thresholds. Obtained with bed load conditions in the overlapping between hyporeic and pythmenic regions and at the deepest position into the through.

Chapter 3

Particle Image Velocity

3.1 Principles

The Particle Image Velocimetry technique is based on the flow digital image processing and it is commonly addressed as non-intrusive because it is one of the less intrusive known techniques, as it only uses tracer particles in the stream. These tracers are illuminated by a pulsed light sheet in subsequent shots allowing to trace the stream turbulent structures.

In order to capture the tracing particles in a certain plane, the pulsed laser light is shaped into a thin light sheet by means of cylindrical and spherical lenses. While the tracer particles are being illuminated by the light sheet, they are captured by the camera, registering its positioning in two consecutive time instants.

This technique was incredibly improved in recent years, mainly due to the development of digital cameras and charge couple device technology, pulsed laser light and computer processing capabilities. Its main advantage is that it provides instantaneous velocity fields instead of punctual measurements or profiles in a single direction.

The method is mainly focused on the determination of displacement fields along a known time interval. This time interval must be short when compared to the minor time scales characteristics of the flow, in order to consider small displacements.

By knowing the particles displacement (Δd_i), and the time interval between two consecutive laser pulses (Δt), both components of instantaneous flow velocity are suitable to be calculated, as shown in equations 3.1 and 3.2.

$$u(x,z) \simeq \frac{(x+\Delta d_x)-x}{\Delta t} \tag{3.1}$$

$$w(x,z) \simeq \frac{(z+\Delta d_z)-z}{\Delta t} \tag{3.2}$$

The following Fig. 3.1 elucidates schematically how the method works.

The PIV technique enables the registry of wide areas in the flow velocity fields, allowing the wide spatial resolution, while the time resolution is limited by the shooting speed of the laser pulse pairs (Raffel et al., 1998; Sveen and Cowen, 2004; Tropea et al., 2007).

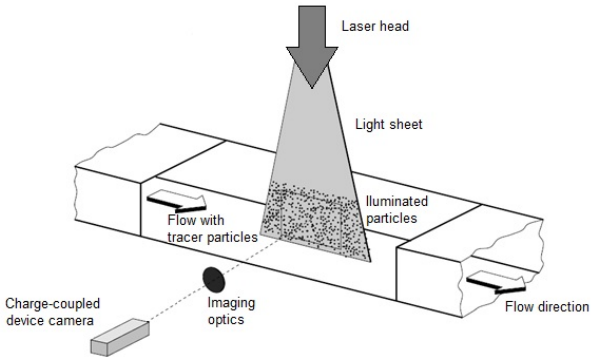

Figure 3.1: PIV experimental setup. Adapted from Raffel et al. (1998).

It is of extreme importance to synchronize the camera with the laser beam, because they must be adjusted to a time interval adequate to the flow conditions. The camera may capture an image pair that occurs in a reduced time frame, so that the same set of particles is registered in both the images. This is possible to achieve recurring to a CCD high speed shutter camera, allowing the capture of images continuously and within a very short exposure time when compared to the time between two consecutive pulses (Δt). Fig. 3.2 represents schematically the synchronization of the laser beam with the CCD camera (Raffel et al., 1998).

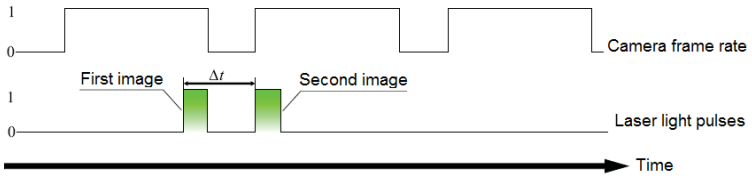

Figure 3.2: Synchronization of the CCD camera with the laser pulses. From Lory (2011).

As represented in Fig. 3.2, the first laser pulse corresponds to the closing of the camera shutter and the next light beam corresponds to the opening of the camera shutter (Raffel et al., 1998). To help with this, there is a synchronization box in the laboratory, where both the CCD camera and the laser head are connected allowing to synchronize them by using a software in a personal computer.

The time interval between each frame pair is controlled by the user as it is input in the beginning of the experiments and kept constant during all procedure. If the first image frame is captured in the time instant t and the second image frame is captured in the time instant t, the time interval, Δt, results from the 3.3.

$$t' = t + \Delta t \tag{3.3}$$

The analysis of each image pair allows to compute the tracing particles displacement, in a certain direction, as exemplified in Fig. 3.3. This calculation is performed recurring to a correlation function that uses the Fast Fourier Transform, FFT, pixel by pixel, in tiny sub-areas designated by interrogation areas (Westerweel, 1997; Sveen and Cowen, 2004).

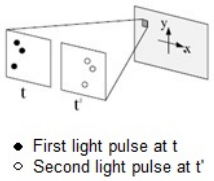

Figure 3.3: A pair of images in the same frame position, results in an average displacement in an interrogation area (Raffel et al., 1998).

An error is introduced when dividing the image frame in interrogation areas because this implies that the same particles are located inside the same interrogation area for both images of the same pair. This error grows with the increasing of the interrogation areas number inside the same image frame, which is the same as increasing the spatial resolution.

The Dynamic Studio software computes each interrogation area separately in correlation maps based in the correspondent image pair, interpreting the correlation function peak as being the average displacement vector of the correspondent interrogation area.

3.2 Correlation methods

A correlation method is a method of analysis based on a statistical approach that results in the most probable correspondence for each particle image pair between each captured pair of frames.

Regarding each interrogation area, the correlation methods set that for a particle image in the first frame, all the particle images in the remaining frame are equally probable to be its pair, representing a certain potential displacement. This is processed to all the particles and then these displacements are represented in a histogram. After setting this procedure for all particle images placed within the interrogation area, the effective displacement will be dominant over every other displacement.

To validate this procedure, there have to be two important requirements: The particle displacement inside each interrogation area have to be near uniform and each interrogation area have to contain a considerable number of particle images.

The Dynamic Studio software works with three different correlation methods,namely, the cross-correlation, the average-correlation and the adaptive-correlation, and the user must choose the most suitable method for the characteristics of the laboratorial experiments undertaken.

A correlation analyses results in a correlation plot such as the one in Fig. 3.4, where the coordinates of the peak correspond to the mean values of displacement in that interrogation area.

The cross correlation method is more often used as it improves the signal-to-noise ratio and eliminates the ambiguity regarding flow direction (Westerweel, 1997; Raffel et al., 1998; Campbell, 2005).

The cross correlation method is more often used as it improves the signal-to-noise ratio and eliminates the ambiguity regarding flow direction (Westerweel, 1997; Raffel et al., 1998; Campbell, 2005).

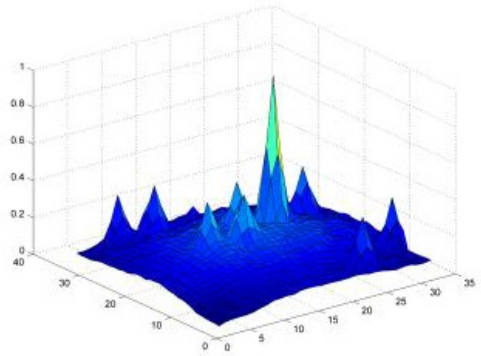

Figure 3.4: Example of a correlation plot. The peak corresponds to the coordinates where the mean displacement estimation stands (Tropea et al., 2007).

These experiments were undertaken using the adaptive-correlation method, which results from improving the cross-correlation method by providing accuracy based on an adaptive interrogation area. This interrogation area is continuously decreased for a certain number of steps or until achieving a certain interrogation area previously introduced.
When achieving a first approach based on the simple cross-correlation method, the interrogation area becomes smaller and it is re-centred based on the highest peak.

This correlation method is particularly recommended in measurements where the flow velocity gradients are not negligible. However, the adaptive-correlation methods time consuming, around 3 times more than the simple cross-correlation method, under the same conditions (Simão et al., 2009).

Other methods are being developed in recent years, such as the adaptive central difference interrogation algorithm and adaptive forward difference algorithm. These methods allow maximizing the spatial resolution of the PIV technique.

The great advantage of using this technique, particularly the adaptive central difference interrogation algorithm, is because it improves accuracy as it produces better results when measuring flow near the boundaries and it produces results with higher signal-to-noise ratios, when compared to the simple cross-correlation (Wereley and Meinhart, 2000). These modified cross-correlation algorithms prove to be very helpful when high accuracy measurements are demanded.

3.3 Errors in PIV

In PIV measurements it is important to know and understand the possible error factors, in order to control them and minimize the spurious data as much as possible.
The most common limitations in PIV are related to camera damages, non-homogeneous laser light sheet, insufficient particles inside the interrogation areas or it can be limited by phenomena like:

- In-plane loss of pairs

The in-place loss of pairs occurs when tracer particles leave the interrogation area because they are a lot faster than the mean velocity within the image frame. This phenomenon contributes to lower the flow velocity estimation because the faster particles are not considered in the correlation function.
In order to prevent the in-plane loss of pairs there may be applied a sub-area in the borders of the interrogation area before performing the correlation method (Ferreira, 2011).

- Velocity gradients

  The velocity gradients phenomenon is also a contribution to the in-plane loss of pairs and it happens when the velocity is not uniform inside the interrogation area. Therefore not all the tracer particles inside de interrogation area correlate equally well. This error becomes significant when the displacement of tracer particles due to local flow gradients becomes larger than the diameter of the particle (Tropea et al., 2007).

- Out-of-plane loss of pairs

  This phenomenon results from particle movements in the camera axis, because tracer particles may enter or leave the exposure sheet between the two pulses losing the correspondent pair. This results in a reduction of the signal-to-noise ratio and it is a PIV limitation that can be improved by simply adjusting the light sheet thickness (Tropea et al., 2007). Fig. 3.5 exemplifies the light sheet intensity profile where particles must stand to be captured by the camera. The light intensity is not constant in its whole thickness, which may result in particles less illuminated and therefore, with an inferior contrast in the captured image.

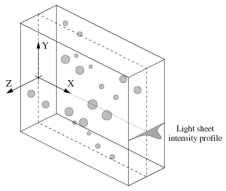

Figure 3.5: Laser sheet thickness (Raffel et al., 1998).

- Peak-locking

  Peak-locking is mainly caused by improper sub-pixel estimation when the input data is distributed asymmetrically around the maximum peak and therefore resulting in a displacement bias error (Tropea et al., 2007). It can be seen in Fig. 3.6 that there is not a clear peak, but the noise is dominating a possible true peak.

- Computational limitations

  The use of a FFT, Fast Fourier Transform, helps to improve the computational time but it implies that the image data has a periodicity and it reduces the calculations accuracy if compared to a direct spatial correlation method.

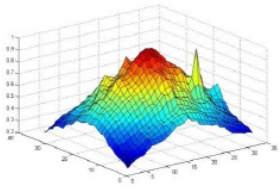

Figure 3.6: Example of a peak-locking phenomena in the correlation plot. The true peak is wrapped between noise (Ferreira et al., 2010).

The size of the interrogation area is of extreme importance because there have to be achieved a compromised between the accuracy and the spatial resolution. Using larger interrogation areas has the advantage of empowering the accuracy and it is very useful for larger motions but the large velocity gradients affect the results. On the other hand, choosing smaller interrogation areas improves the spatial resolution and it is less affected by the velocity gradients but raises inaccuracy and tracer particles must be smaller.

The choice of the interrogation area size depends on the characteristics of the flow and on the equipment available. However, a compromise must be achieved between the interrogation area size and the seeding quantity inserted in the flow, too.

In order to have a good particle density and homogeneity in the PIV images, Raffel et al. (1998) refers that in each interrogation area must be 12 seeding particles and its displacement may not be higher than 25% of the interrogation area side.

However, in the experiments previously performed at this laboratory with similar flow conditions, a number of 5 particles per interrogation area has been producing good results. It corresponds to around 5^6 seeding particles per square meter of fluid.

This is fundamental, regarding the choice of the interrogation area size. It means that when choosing a smaller interrogation area it is mandatory that the seeding quantity is increased also, in order to achieve the number of seeding particles needed per interrogation area.

3.4 Tracer particles

Choosing the right seeding or tracer particles is a factor of extreme importance to achieve reliable data. The seeding must represent precisely all flow motions because they are responsible for the achievement of punctual displacements by registering its successive position.

The tracer particles behaviour is mainly influenced by external forces, such as, gravity, centrifugal and electrostatic, and by its own shape, diameter and specific mass. It is also influenced by the fluid characteristics, such as fluid density and dynamic viscosity.

Although the particle shape affects the flow resistance, it is neglected. All the particles are assumed to be spherical due to its small size, which is of around 10 to 80 μm.

The contact between particles when suspended in the flow is neglected because under concentrations around 10^9 particles/m^3 it is known that the distance between particles is around 1000 times its own diameter.

According to Prasad (2000) there are two main conditions that tracer particles must satisfy in order to be used in PIV measurements. It has to follow the flow streamlines without slipping and they must be efficient light scatterers because if they are not, it must be compensated by improvements in the laser and camera technology which are very expensive.

The main condition for the particles to follow all flow fluctuations is the settling velocity under gravity in stagnant water. Assuming that the process is governed by Stokes drag, thus the settling velocity is given by equation 3.4.

$$V_{sp} = \frac{g \times d_p^2 \times (\rho_p - \rho_f)}{18 \times \mu} \tag{3.4}$$

where V_{sp} stands for the settling velocity, g represents the gravity acceleration, d_p is the particle diameter, ρ_p and ρ_f are the density of the particles and fluid, respectively and the μ represents the fluid dynamic viscosity.

If the V_{sp} of a certain sort of particles is negligible when compared to the flow velocity, then it is warranted that these particles can represent perfectly all flow fluctuations.
Melling (1997) have also used a solution, based on Hjemfelt and Mockros (1996) results, to evaluate the seeding particles ability to follow the flow without slipping. They applied the equation 3.5 to evaluate if the seeding is good enough to be used in PIV measurements.

$$\frac{\overline{V_p^2}}{\overline{V^2}} r_p = (1 + \frac{2 \times \pi \times f_c}{18 \times \mu})^{-1} \tag{3.5}$$

where, ν, represents the kinetic fluid viscosity and f_c is the frequency of turbulent structures.
It relates the absolute particle velocity, V_p to the absolute flow velocity, V. Thus, if $\rho_p = \rho_f$ then, $V_p = V$ and the particles follow the fluid motion exactly, because $r_p = 1$ (Chao, 1964). Melling (1997) stated that it is acceptable that r_p stand between 0.95 and 1.

Because it is difficult and considerably expensive to acquire particles with such characteristics, it is thus considered that $r_p = 0.95$ represents a considerable significance. And r_p is then compared to the frequency of turbulent structures value, f_c, achieving the relation represented in Fig. 3.7, which valid to the tracer particles used.

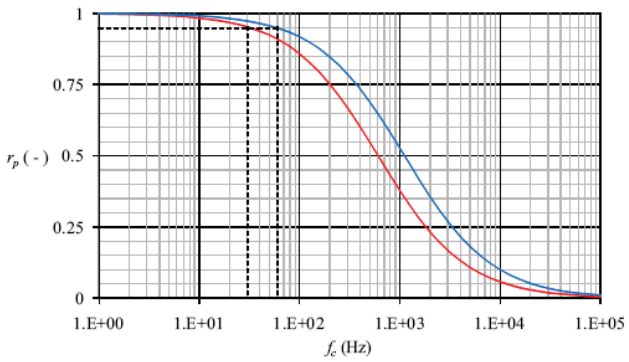

Figure 3.7: r_p plotted against f_c for particles of PSP (left) and DECOSOFT 60 (right), with diameters of 50 and 60 μm, respectively (Lory, 2011).

Fig. 3.7 shows the example of seeding particles with 50 and 60μm, respectively, PSP and DECOSOFT 60. There is possible to notice that the 0.95 significance is related to a frequency f_c of 50 Hz. The curves were achieved with a flow average velocity, $\overline{u}$, of 0.11 m/s and a wavelength of turbulent structures, λ_t of 2.2 mm, that corresponds to the double of the interrogation area (around 1.1 mm). It is possible to observe turbulent structures by using this interrogation area and wavelength according to Nyquist (Tropea et al., 2007). The turbulent structures frequency may then be calculated by inverting the period (T_p), as shown in equations 3.6 and 3.7.

$$T_p = \frac{\lambda_t}{\overline{u}} \tag{3.6}$$

$$f_c = \frac{1}{T_p} \tag{3.7}$$

Recently, there is being used another criteria, related to the particle Stokes number, S_k, that results from the ratio between the characteristic response time, τ, and the characteristic flow time scale, represented by τ_f. It states that if $S_k < 0.1$ then the tracing particle is suitable to be used in the flow with a minimum error of less than 1 (Tropea et al., 2007).

However, these experiments were undertaken using pepper as seeding. The use of these tracers was subjected to a study performed by Ferreira (2008) where two options were available, pollen and pepper. These possibilities were analysed in its dimensions, fall velocity in still water, shape and capacity of following the flow. It resulted in the conclusion that pepper would constitute a reliable seeding to perform those experiments. Further details are presented in Ferreira (2008).

3.5 Light scattering

To represent the fluid-mechanical requirements it is mandatory that the tracer particles are as small as possible, but regarding the light scattering they must be large enough to achieve an high signal-to-noise (SNR) of the scattered light signal.

The light-scattering is of extreme importance to achieve a good contrast and then a good signal quality of the captured images.

For PIV purposes the CCD camera is normally positioned at an angular position of 90° from the light sheet plan. Thus, it is not only important to get a good signal-to-noise ratio but it is extremely important to achieve a scattered light intensity from the seeding particles in its cross section.

Mie scattering theory focuses on the particle light scattering ability. It is suitable of being applied in the particular case of spherical particles, with diameter, d_p, which is larger than the wavelength of the incident light, λ_l (Raffel et al., 1998; Tropea et al., 2007).
It states that the light scattering depends on the particle diameter, light wavelength and refractive index of the tracer particle.

The Mie theory considers the normalized diameter, q_n, which is defined by equation 3.8.

$$q_n = \pi \times \frac{d_p}{\lambda_l} \tag{3.8}$$

The best practice is to use the largest tracer particle which can represent the flow characteristics without excessive slip because it maximizes the light scattering and provides better results (Prasad, 2000).

Fig. 3.8 and 3.9 show how the light scattering increases with the increasing of the particle diameter. In this case there were used glass spheres with 1 μm and 10 μm and a light wavelength 532 nm (Raffel et al., 1998).

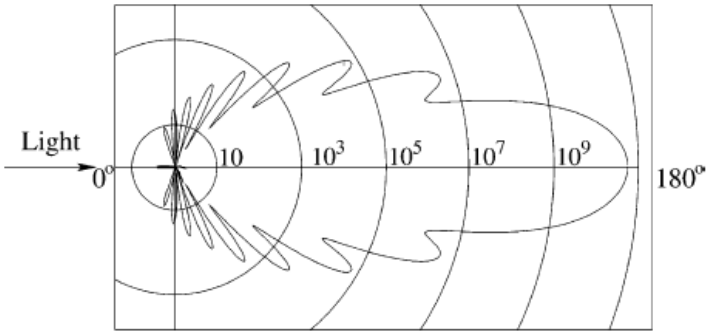

Figure 3.8: Light scattering resulting from a glass spherical particle in water, with a diameter of 1 μm. Adapted from Lory (2011).

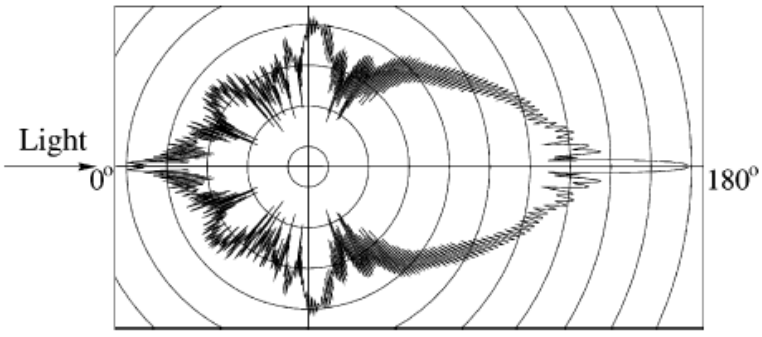

Figure 3.9: Light scattering resulting from a glass spherical particle in water, with a diameter of 10 μm. Adapted from Lory (2011).

It is also a fact that the scattering efficiency depends a lot on the ratio between the refractive index of the particles to that of the fluid. In certain cases the seeding particles may be silver coated or coated with fluorescent characteristics in order to switch the refractive light to a different wavelength to the water, and consequently increasing the contrast.

The use of pepper as seeding provides reliable results as stated in (Ferreira, 2008).

3.6 Other aspects of tracer particles

Other factors that may be important when choosing the seeding are related to the environment, operator and equipment security. The particles must not be toxic, hazardous, preventing the operator from respiratory disorders and it must not be corrosive or abrasive when in contact with the equipment.

Chapter 4

Facilities

4.1 Introduction

To accomplish the main goal of this thesis, turbulent parameters that characterize the flow are going to be processed based on instantaneous flow displacement maps achieved in laboratorial experiments. The turbulent quantities, essential to allow the flow characterization derive from instantaneous flow displacement maps, bi-dimensional, that were achieved by means of a 2D Particle Image Velocimetry system (PIV).

All the laboratorial activities related to this thesis were performed in the Laboratory of Hydraulics and Environment of Instituto Superior Técnico. An exhaustive description of the laboratorial equipments is done in the following sub-chapters, specially focusing on the PIV system and on the Hydraulics Tilting and Re-circulating Flume (CRIV). Fig. 4.1 shows a general view of the flume while Fig. 4.3 represents a schema of the CRIV.

4.2 Laboratorial Facilities

The CRIV is placed at the CEHIDRO/IST and it consists of a prismatic flume, sustained in a steal structure and that includes a recirculation circuit.

The flume has a square cross section with 409 mm wide, 300 mm in height. Its effective length was 10 m at the date of these experiments, although, it was recently upgraded to 12.5 m. The CRIV includes a support bar placed above the structure that is useful to slide a support carriage, shown in Fig. 4.2, which helps during the experiments, measurements and calibrations that are performed throughout the flume. It is composed by 10 glass panels, 0.5 m height, in each sidewall, that keep the fluids inside the flume and allow to acquire experimental data recurring to measurement means based on flow visualization.

The main structure is composed of a beam with 12.5 m length supported by columns and the upstream column is suitable of being raised or lowered in order to adjust the flume slope. The slope is adjustable through means of a motorized system, shown in Fig. 4.4, that elevates or lowers the flume sustaining column in the upstream extremity. The slope adjustment ranges between $-1/200$ and $+1/40$.

Figure 4.1: General view of the recirculating tilting flume at the Laboratory of Hydraulics and Environment of Instituto Superior Tecnico.

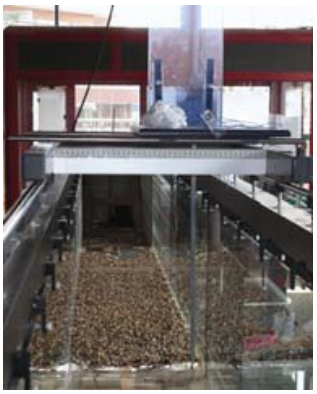

Figure 4.2: Support carriage that slides along the flume to help during measurements.

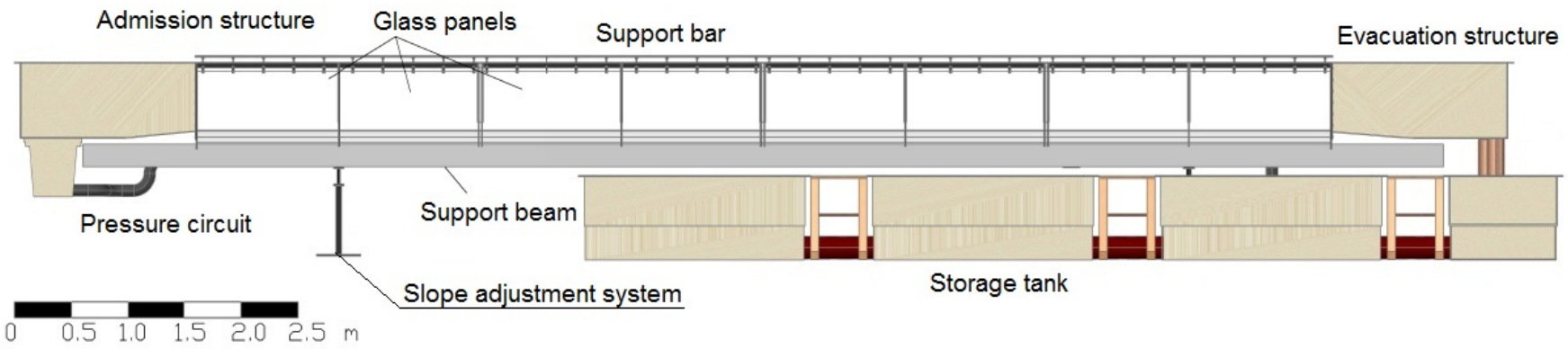

(a) criv1

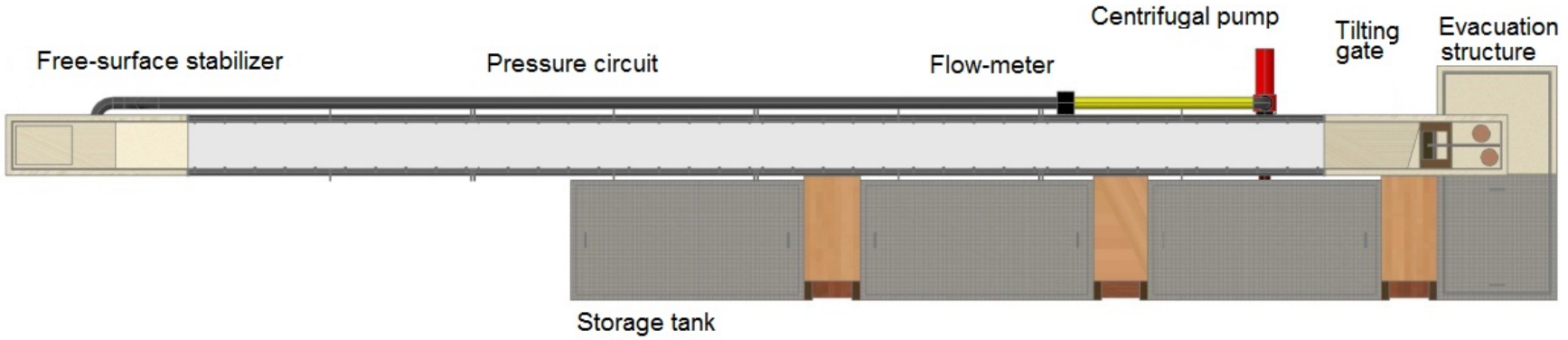

(b) criv2

Figure 4.3: Schematics of the recirculating tilting flume and its main components. a) Plan view; b) Side view. Adapted from Ricardo (2008).

Figure 4.4: Slope adjustment structure composed by an electric motorized system.

The recirculation circuit is composed of four inertial tanks that store a total volume of around $1.1\,m^3$ each, shown in Fig. 4.5 and by a pressure circuit that allows to control the flow rate introduced in the flume. The tanks are set in a line, connected through PVC pipes with 200 mm of diameter set near the bottom of each tank and working like connected vessels.

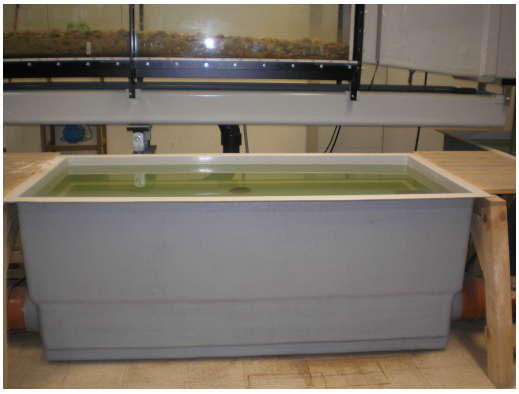

Figure 4.5: Example of one of the four storage tanks.

The pressure circuit is composed of a centrifugal pump, shown in Fig. 4.6(a), which drives the stored water into the flume admission structure. This flow is conducted through 100 mm of diameter PVC pipes, set parallel to the channel. The centrifugal pump is able to raise a maximum flow of $220\,m^3/h$.

This circuit is equipped with an isolation valve and a check valve upstream the pump and in the downstream section to control the flow. An electromagnetic digital flow-meter, presented in Fig. 4.6(b), which is installed in the compression circuit, allows measuring the flow rate introduced into the flume.

There must be highlighted that the centrifugal pump is fed from an intermediate tank to avoid collecting air or sediments and consequently introducing them into the flow.

The CRIV is equipped with an admission and an evacuation structure in the upstream and downstream extremes, respectively. The admission structure enables to feed the flume with the water flow and it is composed by the channel inlet and a free-surface stabilizer. This stabilizer is a simple wooden board aiming to reduce significantly the free-surface oscillations generated by the pressure circuit. This structure is fed vertically through a PVC conduct with 100 mm of diameter.

(a) (b)

Figure 4.6: (a) Centrifugal pump used during the experiments. (b) Digital flow-meter used to measure the flow rate inserted in the flume.

Downstream, the evacuation occurs due to gravity and to the first storage tank, through two circular holes in the threshold of the evacuation structure, as shown in Fig. 4.7(a). The evacuation structure is equipped with a tilting gate, presented in Fig. 4.7(b), which allows a precise regulation of the stream free surface elevation, useful to adjust slow streams.

(a) (b)

Figure 4.7: (a) Downstream evacuation pipes. (b) Tilting gate used to adjust the free surface elevation.

Since the channel cannot recirculate sand sediments, its introduction into the flow is performed by means of a convey belt which is equipped with an electric motor including drive control and that allows to set its speed between 0 and 270 rpm. The convey belt includes a structure that allows to input a sediment layer of adjustable thickness and width, thus controlling the sediment quantity introduced into the flow. This also allows depositing an equivalent amount of sediments along the whole width. The sand sediment input is performed 2.5 m downstream from the admission structure.

This structure also incorporates a polystyrene board aiming to stabilize the small superficial waves caused by the introduction of sand sediments in the stream.

4.3 Instrumentation

During these experimental works there were registered several measurements, such as, free-surface elevation, water temperature and were acquired the bed topography maps and bi-dimensional instantaneous flow displacement maps. This chapter intends to describe the equipment that was used to undertake these measurements.

Laser safety goggles, presented in Fig. 4.8, were used during the experiments as a protection against the dangerous laser wavelengths applied in the laboratorial experiments with PIV equipment.

The free-surface elevation was measured using a conventional ruler with a precision of 0.5 mm, represented in Fig. 4.9(a).

Figure 4.8: A pair of laser safety glasses.

A digital thermometer, represented in Fig. 4.9(b), was used to determine the water temperature. The water temperature is important to estimate the water viscosity.

(a)

(b)

Figure 4.9: (a) A 0.5 mm precision ruler used to measure the free-surface elevation. (b) Digital thermometer.

The point gauge with 0.1 mm of precision represented in Fig. 4.10 was employed in the bed topography determination.

Figure 4.10: Point gauge, with 0.1 mm, used to determine bed topography.

To acquire the bed topography map, a point gauge mounted on rails was used over a point grid in the bed. This grid is placed over the measurement sections and it is equally spaced with a density of 1 sample/cm^2. This scheme helps setting the measurement points over its nodes. By manually operating the point gauge and using a 0.5 mm precision ruler, it was created a grid of elevations that allows achieving an estimate of the bed topography.

A Particle Image Velocimetry (PIV) setup was used to measure the two-dimensional instantaneous flow displacement maps. PIV is considered to be a non-intrusive method widely used in instantaneous flow velocity measurements of high spatial heterogeneity (Ferreira, 2011) and it is composed of:

i) Laser head with lenses, represented in Fig. 4.11(a)

ii) CCD camera (charge-couple device), represented in Fig. 4.12

iii) A power supplier, represented in Fig. 4.11(b)

iv) Software-controlled acquisition system namely DynamicStudio by Dantec

(a) (b)

Figure 4.11: (a) Laser head mounted on the support carriage. (b) Power supply used in the experiments.

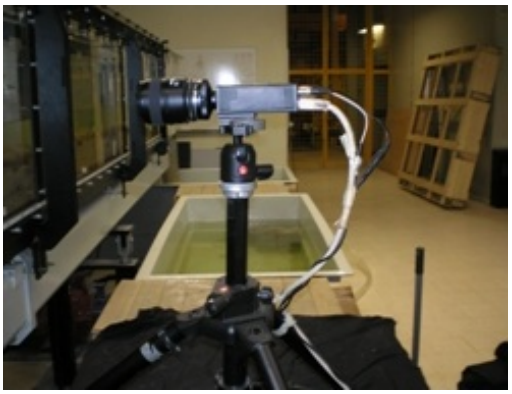

Figure 4.12: CCD camera on a tripod.

The PIV setup is composed of a Nd:YAG (YAG Cristal - Yittrium Aluminium Garnet - infiltrated with Neodymium ions) laser provided by Dantec. This laser emits fundamental light in the infra-red gamma (IV) which is not visible by bare eye. However, there is a system, set in the laser head, that changes the near-IR light into green visible light. This system is denominated SHG (Second Harmonic Generator) and consists of a nonlinear crystal that doubles the frequency of the Nd:YAG laser emission. It converts the infra-red light, wavelength 1064 nm into wavelength 532 nm green light (Raffel et al., 1998). This change in the laser wavelength is performed aiming to achieve good safety conditions and is complemented by using the safety goggles presented earlier in Fig. 4.8 of this chapter.

The laser head is placed over the flume, in the support carriage, being allowed to slide along the whole channel effective length. It is equipped with an optical system which includes spherical and cylindrical lenses that generate a light sheet by diverging the beam through the cylindrical

lens and controlling its thickness through the spherical lens (Tropea et al., 2007). By these means it is possible to adjust the beam alignment and to generate a light sheet that illuminates each measuring site. Fig. 4.13 shows an example of a light sheet.

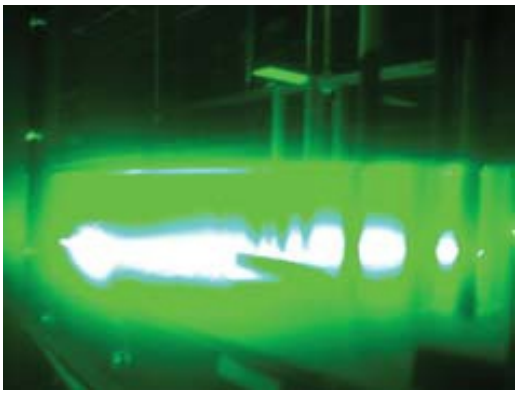

Figure 4.13: Example of a laser light pulse. From Lory (2011).

The CCD camera captures the plane illuminated by the laser sheet in a 1600×1200 frame and registers the seeding positioning in the flow, repeating the procedure at a high rate. This camera is widely used in scientific experiments mainly due to its accuracy but also because it stores the collected images in a digital format, which allows data to be processed later by other devices or software.

The laser beam is generated and controlled by the PIV power supplier, represented in Fig. 4.11(b). This component is suitable of being controlled by the acquisition software, DynamicStudio.

Chapter 5

Primary data and data analyses

In this chapter it is intended to describe the available data and the conditions in which they were achieved. It is followed by a detailed description on how it is organized and manipulated, until achieving the parameters that will be analysed in chapter 6. The available data results from the experiments undertook by Ferreira (2008) and Amatruda (2009), where a more detailed description of the laboratorial experiments can be found. This thesis relies on a different approach over these same experiments. It starts by characterizing some important conditions in which the laboratory experiments were performed. Then it focus on data computation of the parameters that characterize the flow and which are analysed in the scope of this thesis.

5.1 Laboratory experiments

Two experimental tests were undertaken to achieve instant flow velocity maps, under uniform flow conditions, aiming to study the near-bed sediment transport, namely S3 and S4, respectively in mobile bed and immobile bed conditions.
In both tests the coarse-gravel elements were forming a 3D structure in the bed, whose interstices were filled with sand. This was achieved by water-working the bed during 30 hours to completely assure the armouring conditions. By filling the interstices, the thickness of the pythmenic layer is reduced and consequently the porosity in the substratum is reduced too.
In test S4 the filling sand is well stored below crests and in-between pebbles. There is no sediment transport in the near-bed region, under the imposed flow conditions, while in test S3 the sand presence in the bed was slightly increased, until the sand discharge achieves minimum transport capacity.

Table 5.1 shows the main characteristics which were controlled for each test, S3 and S4, where Q stands for flow discharge, i is the bed slope, q_b is the volumetric sediment discharge and the bed materials characteristics are the mean diameter, d_{50}, and the geometric standard deviation, σ_D. Values with superscript indication of (s) and (g) stand respectively for sand or gravel.

Tabela 5.1: Main characteristics of experiments S3 and S4 (Amatruda, 2009).

Test	$Q\,(\mathrm{l/s})$	$i\,(-)$	$q_b\,(\mathrm{l/s})$	$d_{50}^{g}\,(\mathrm{mm})$	$\sigma_D^g\,(\mathrm{mm})$	$d_{50}^{s}\,(\mathrm{mm})$	$\sigma_D^s\,(-)$
S3	23.3	0.0044	4.77×10^{-3}	28	1.4	0.9	1.6
S4	16.7	0.0044	2.08×10^{-3}	28	1.4	0.9	1.6

5.2 Characteristics of the bed surface

In both tests, namely S3 and S4, the bed was build respecting natural environment conditions. The pebbles used to compose the gravel bed have diameters between 0.5 and 7.0 cm. The mobile sediment used in these experiments was sand with a mean diameter of $d_{50}^{(s)} = 0.8\,\mathrm{mm}$ and geometric standard deviation of $\sigma_D^{(s)} = 2.6$.

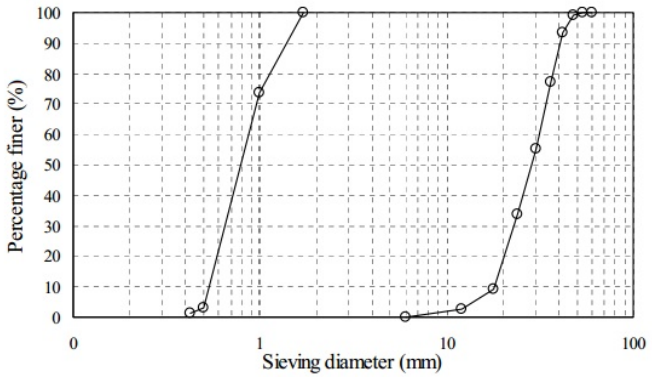

Figure 5.1: Grain size distribution of the sand (left) and coarse-gravel (right) (Ferreira, 2008).

Fig. 5.1 represents the finer sediments at the left and the coarse-gravel at the right. The finer sediments were measured using dry-sieving sand samples, by Nogueira (2007) and Ferreira (2008), who determined the coarse-gravel grain size distribution directly measuring a set of 110 samples with a 0.1 mm precision calliper gauge. The bed is characterized by the parameters shown in Table 5.2, such as, the value of the elevation of the lowest trough, z_t, the elevation of the highest crest, z_c, the thickness of the pythmenic layer (Ferreira et al., 2010), $\delta = z_c - z_t$, the bed porosity, λ_b and the mean value of the void function, φ_m, which characterizes the rate of space that is occupied by the fluid in a sectional area of the flow. For further details consult sub-chapter 5.2.2.

Tabela 5.2: Geometrical characteristics of the bed (Amatruda, 2009).

Test	$z_t\,(\mathrm{m})$	$z_c\,(\mathrm{m})$	$\delta\,(\mathrm{m})$	$\varphi_m\,(-)$	$\lambda_b\,(-)$
S3	0.107	0.146	0.039	0.7197	0.22
S4	0.090	0.144	0.053	0.6570	0.34

The geometric values were measured using the flow structure criterion shown in Fig. 2.3 from chapter 2.3.2, which was proposed by Ferreira et al. (2012).

5.2.1 Bed Topography

The bed topography in the measurement area was taken into account by determining a Digital Terrain Model (DTM). To achieve that, it was used a 0.1 mm precision point gage, to measure the elevation of points in a mesh over the measurement area. This grid was build of squares with 5 mm of side, along both directions. Fig. 5.2 shows the measurement area, painted in black to reduce reflection when using the PIV system.

Figure 5.2: Measurement area, adapted from Ferreira (2008).

5.2.2 Void Distribution

Void fraction measures the rate of space occupied by water, within a cross-sectional area of the channel including the voids in-between the lowest trough and the highest crest. It basically depends on the sectional area of the pythmenic layer that is occupied by water, as the volume above the same layer fully corresponds to water. It is usually represented by its average value, measured along the channel.

The works undertook by Ferreira (2008) aimed at the estimation of the void function, starting by calculating it using a Perspex box, due to its simplicity, for a gravel bed framework. Based on this much simpler case, it was then extrapolated to the conditions of S3 and S4, gravel and sand bed.

It was verified that the void function can be estimated by a negative exponential expression, such as the Gaussian curve represented in equation 5.1.

$$\varphi(\zeta) = \lambda_b + \int_0^{\zeta} A' \cdot e^{\frac{1}{2}(\frac{\eta - B'}{C'})^2} d\eta \tag{5.1}$$

where the value of λ_b represents the porosity of the bed substratum, η is the non-dimensional height and A', B' and C' are constants that are chosen based on the experimental curve, obtained with the Perspex box. The curve that best fits the experimental points for gravel bed framework is presented in equation 5.2.

$$\varphi^{S_0}(\zeta) = \lambda_b^{S_0} + \int_0^{\zeta} 1.55 \cdot e^{\frac{1}{2}(\frac{\eta - 0.57}{0.16})^2} d\eta \tag{5.2}$$

The void distribution for tests S3 and S4 were then synthesized from the one of the gravel framework, using the elevation of the bed deposits and the porosity of the sand. Ferreira (2008) and Amatruda (2009) achieved the following fitting curves, estimating the void distribution function.

$$\varphi^{S_3}(\zeta) = \lambda_b^{S_3} + \int_0^{\zeta} 1.25 \cdot e^{\frac{1}{2}(\frac{\eta-0.20}{0.35})^2} d\eta \tag{5.3}$$

$$\varphi^{S_4}(\zeta) = \lambda_b^{S_4} + \int_0^{\zeta} 1.54 \cdot e^{\frac{1}{2}(\frac{\eta-0.571}{0.17})^2} d\eta \tag{5.4}$$

The mean void fraction, φ_m, previously shown in table 5.2, is then calculated by integrating the void distribution function as shown in the following equation 5.5

$$\varphi_m = \int_0^1 \varphi(\eta) \cdot d\eta \tag{5.5}$$

5.3 Mean Flow Characteristics

Uniform flow conditions were achieved by adjusting the downstream gates of the channel. Table 5.3 lists the characteristics related to the mean flow in both tests.

Tabela 5.3: Mean flow characteristics of tests S3 and S4 (Amatruda, 2009).

Test	Z_s (m)	h (m)	h^* (m)	U (m/s)	τ_0^1 (Pa)	$u^{*(1)}$ (m/s)	τ_0^2 (Pa)	$u^{*(2)}$ (m/s)
S3	0.234	0.127	0.116	0.648	3.218	0.057	3.060	0.057
S4	0.246	0.156	0.137	0.557	4.301	0.066	3.924	0.062

The Z_s represents the free surface elevation, while h stands for the flow depth, $h^\star$ is a reference flow depth for shear stress calculation purposes and is calculated as shown in equation 5.6, U is the depth averaged mean flow velocity in the stream direction, calculated in 5.7, where Q stands for the flow discharge and D is constant and represents the flume width of 0.409 m.

$$h^\star = h - \delta(1 - \varphi_m) \tag{5.6}$$

$$U = \frac{Q}{D \cdot (Z_s - z_c)} \tag{5.7}$$

The value of τ_0 stands for the total shear stress of the flow and it is calculated in two different approaches. In one hand, $\tau_0^{(1)}$ is achieved by the equation of conservation of momentum, as presented in equation 5.8. In the other hand, it is estimated from the total shear stress profile, represented by $\tau_0^{(2)}$.

$$\tau_0^{(1)} = \rho^w g R^* i \tag{5.8}$$

$\rho^{(w)}$ stands for the water density, g is the acceleration of gravity, i is the bed slope and R^* is the hydraulic radius calculated by equation 5.9.

$$R^* = \frac{D \cdot h^*}{2 \cdot h^* + D} \tag{5.9}$$

To achieve $\tau_0^{(2)}$ it is considered the profile of total shear stress of the flow, as presented in Fig. 5.3. This profile is subjected to a liner regression in the linear segment and then extrapolated to the level of the mean void function level, estimating the value of total shear stress of the flow, $\tau_0^{(2)}$.

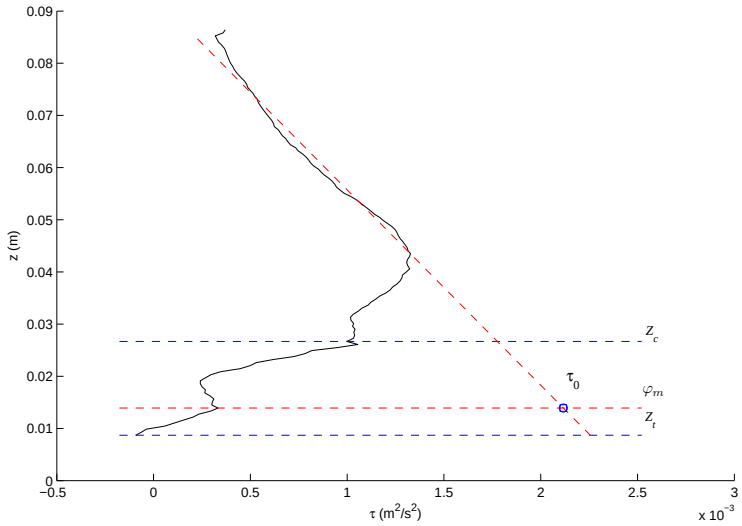

Figure 5.3: Extrapolation of $\tau_0^{(2)}$ from the total shear stress profile

The value u^* represents the friction velocity, as it depends on the value of τ_0 , it results also in two values, superscripted with (1) and (2), and it is calculated as shown in equation 5.10.

$$u^* = \sqrt{\frac{\tau_0}{\rho^{(w)}}} \tag{5.10}$$

The mean flow is also suitable of being characterized by non-dimensional parameters, which are presented in Table 5.4. These values are Froude number, Fr, in equation 5.11, Reynolds number, Re, in equation 5.12, and the Shields parameter, in equation 5.13, for both gravel and sand sizes, respectively.

Tabela 5.4: Non-dimensional parameters of experiments S3 and S4 (Amatruda, 2009).

Test	Fr	Re	ϑ^g	ϑ^s
S3	0.61	76606	0.008	0.223
S4	0.45	86843	0.009	0.269

$$Fr = \frac{U}{\sqrt{g \cdot h}} \tag{5.11}$$

$$Re = \frac{U \cdot h}{\nu} \tag{5.12}$$

$$\vartheta^i = \frac{u_*^2}{(\frac{\rho^{(i)}}{\rho^w} - 1) \cdot g \cdot d_{50}^i} \tag{5.13}$$

where U represents the depth-averaged mean flow velocity, g is the acceleration of gravity, h is the flow depth, ν is the viscosity of the water, u_* stands for friction velocity, ρ^w is the water density, ρ^i is sand or gravel density, and d_{50}^i is the mean diameter of sand or gravel.

Table 5.5 shows the water temperature during the experiments, S3 and S4, where T_i and T_f are standing for the water temperature when the test started and finished, respectively.

Tabela 5.5: Water temperature measured at the beginning and at the end of experiments S3 and S4 (Amatruda, 2009).

Test	T_i (°C)	T_f (°C)
S3	21.3	21.6
S4	24.8	26.2

5.4 Data Organization

Two main sets of data were acquired, on one hand in water flow conditions that implies the bed-load sediment transport, named S3, and in the other hand, the comparison conditions, without bed-load sediment transport but still with an armoured bed composed by sand, which was named S4.

Both measurements were performed between the 6.62 m and 6.84 m of the channel, measured from the channel inlet, and the camera was positioned in the right channel sidewall, as shown in Fig. 5.4.

To ensure that the camera was always accurately placed in the described longitudinal locations a calibration board, using plain squared paper, was placed in the right side channel wall as shown in Fig. 5.5. The distance from the inlet to the calibration board was measured, which is of 6.62 m and as the board uses plain squared paper, it is possible to measure any distance regarding the camera longitudinal positioning. As the camera keeps a perpendicular angle to the channel sidewall and using this calibration board, it is possible to determine the exact coordinates of all points in the images.

Five lateral laser sheet positions were obtained at each camera location, however, this thesis focus on the central longitudinal position, namely P1, and in the central lateral position, at 20.5 cm, coinciding with the flume axis. These distances were measured from the channel right sidewall, with a 0.5 mm precision ruler, shown in Fig. 4.9(a).

The PIV equipment has limitations in the data storage capacity of the workstation buffer. Taking this limitations into account and regarding to collect the maximum amount of data, several data acquisitions were performed for the same camera longitudinal positioning and laser sheet, without altering any conditions. Each data acquisition is named *run* and encloses instantaneous

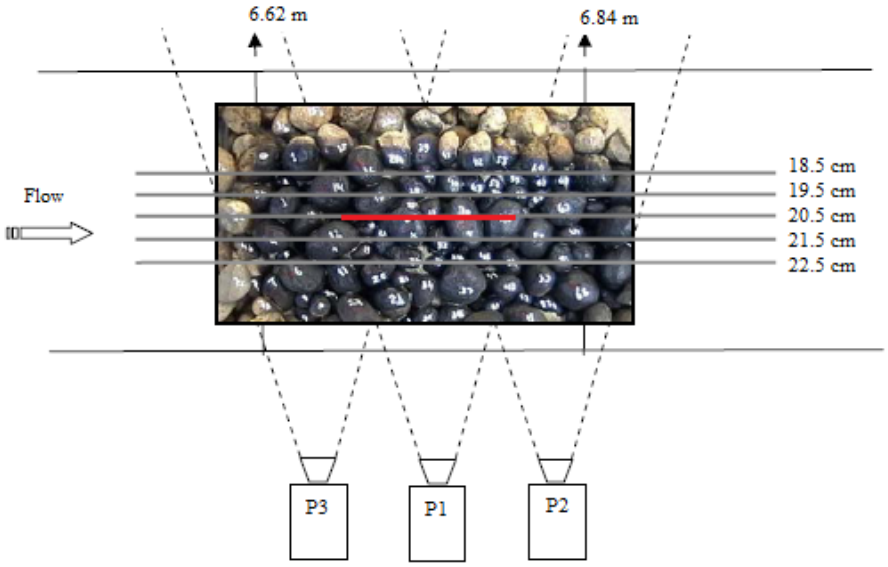

Figure 5.4: Camera position. Adapted from Ferreira (2008).

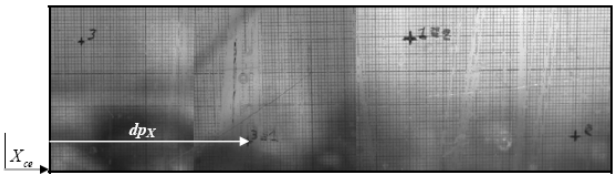

Figure 5.5: Calibration board used to set the longitudinal position of the camera (Ferreira, 2008).

flow displacement fields for hundreds of time instants.

Table 5.6 shows the organization of the collected data, such as, acquiring position, number of runs and number of maps in each run. The number of maps represents the number of laser pulse pairs. Each image pair corresponds to a single time instant in which there was obtained a displacement map.

Tabela 5.6: Some positioning and size characteristics of the acquired data

	Long. position	Lat. position	Nr. of runs	Nr. of maps
S3	P1	20.5	8	525
S4	P1	20.5	8	463

As the *Dynamic Studio* is the software used to acquire data in the laboratory, raw data is in its former format. These data are organized in a column for each run, as if the data file was scanned column after column, before concatenating them in a single one. The *Dynamic Studio* organizes the displacement data separating them in the two orthogonal directions and in a single file to each direction, time instant and run when it was performed.

To manipulate the data using with Matlab, the files must be exported to $^*.mat$ files. This is a time consuming task because it must be done very carefully, in order to avoid any mistake in the naming of each file and in its organization in directories.

When Matlab imports the data, it is set in two-dimensional matrices, each matrix representing the displacement in each direction, time instant and for its respective run.

5.5 Data Analysis

The data analysis is a time-consuming process that requires a thought virtual space management, since the data computation requires a considerable computer processing capacity and storage equipment. To perform this work it was used a common computer equipped with a 3.10 GHz dual-core CPU using Matlab R2009b x64, in a windows 7 environment.

This work can be divided in 3 stages, the data export stage, the despiking stage and the data treatment stage. In the first stage all raw data from Dynamic Studio was exported into **.mat* files that can be manipulated later using Matlab. This task took a considerable amount of time and it was performed for each test and run in the same camera position, resulting in a set of data with almost 3 Gb.

After having all the data in Matlab files, the second stage starts by using the Goring and Nikora filtering method (Goring and Nikora, 2002), described which will be presented in chapter 5.5.3. Before the method itself finishes, there must be performed a calibration and mask operation, as described ahead. The Goring and Nikora method cleans the data from every spurious vector persisting in the flow velocity field. The described task spends a lot of time because there is a considerable amount of data and the process itself is very refined. Using the available equipment it spends around 6 hours to clean each set of data, which encloses data from 8 runs of the same test, S3 or S4.

Data treatment is processed in the last stage, where the data is subjected to a quadrant threshold analysis, as described in 2.4, analysing the influence of the threshold and performing a statistical analysis of the parameters that characterize the flow, under a constant threshold.

5.5.1 Linear Image Calibration

The image calibration must be performed because the CCD camera uses pixels to measure distances. In hydraulics research I.S. units are commonly used and there must be set a correspondence between pixels and meters.

A calibration factor was computed for each experimental test and camera position, and the same factor is used in every run acquired in these conditions.

Before starting each laboratorial experiment, it was suspended a square ruler in the precise position where the laser sheet was going to be set and a picture of it was stored, as shown in Fig. 5.6. Because this square ruler is scaled in the two directions, it is possible to obtain the distance between two points in meter and the Matlab script can identify the coordinates of both points in pixel. With this data, the distance between the two points can be calculated both in meter and pixel, as shown in equations 5.14 and 5.15. The calibration factor is achieved by using the equation 5.16.

$$\Delta_m = \sqrt{(\Delta_x)^2 + (\Delta_y)^2} \tag{5.14}$$

$$\Delta_p = \sqrt{(p_{x,2} - p_{x,1})^2 + (p_{y,2} - p_{y,1})^2} \tag{5.15}$$

$$F_c = \frac{\Delta_m}{\Delta_p} \tag{5.16}$$

where Δ_m and Δ_p are standing for the distance between both points, respectively in meter and pixel. Δ_x and Δ_y are the distances in both orthogonal directions. $p_{x,1}$, $p_{y,1}$, $p_{x,2}$ and $p_{y,2}$ are the coordinates of both points, p_1 and p_2, in pixel. The calibration factor is represented by F_c. Four pairs of points were picked in points where the coordinates are known in meters aiming to collect four representative calibration factors.

These calibration factors are used to calculate its average and its standard deviation, resulting in a single value to use for that particular position. So that the camera effects are overcome, it is recommendable that the user picks points as far as possible and in an oblique segment, improving the values achieved through the Pythagoras theorem.

Fig. 5.6 shows an example of a pair of points picked by the user, to be considered in the calibration factor calculations.

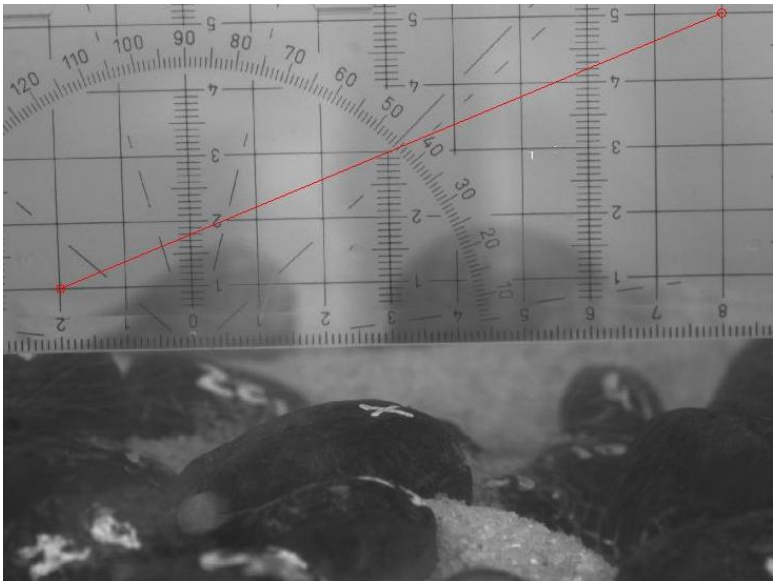

Figure 5.6: Example of a calibration image with a pair of points marked for calibration purposes.

This procedure demands that the camera magnification must be constant during the experiments in the same camera and laser sheet position.

The Matlab script demands for at least four pairs of points but allows the user to repeat the procedure for innumerous times if he finds that the standard deviation is too high. The calibration factor results in meter per pixel and it is saved as a variable to be applied right after the Goring and Nikora (2002) despiking method.

5.5.2 Masking the fields

As the calibration factor, a single mask is used for every run in each camera position. The masked field is important to neglect spurious data which mainly correspond to the field boundaries. In this process the user draws polygons in order to create a filter that, when applied, eliminates the still boundaries. Fig. 5.7 shows an example of a polygon used to mask a displacement matrix.

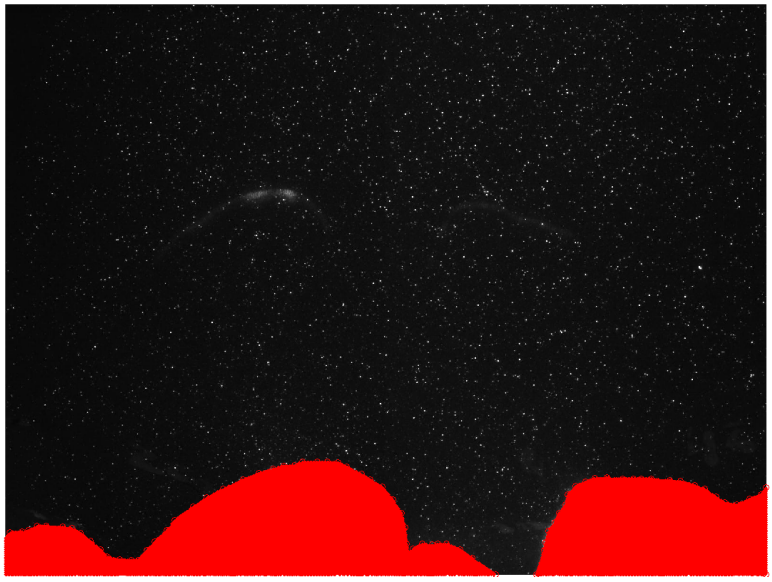

Figure 5.7: Example of a mask used to neglect the bed roughness where it is known that any displacement in the data represents spurious data. The filtering mask in represented in red and fits the bed roughness.

This mask helps the data filtering process because the system simply does not consider the data in these locations. It also helps by improving the computer processing time and avoiding the continuous reappearance of spurious data, in a way that may be understand later, in the sub-chapter 5.5.3.

By picking points in a provided image, the user defines a polygon. Based on that polygon, the script builds a matrix with zeros and ones, setting the zeros in the positions inside it and the ones in the field outside the polygon. When this matrix is layered over the initial matrix, it eliminates the spurious data, helping in the data filtering process.

The filtering mask is stored as a variable and applied before the data filtering begins. This automatically eliminates the data that correspond to the points where no displacement is allowed, mainly due to the presence of gravel in the rough channel bed.

5.5.3 Data Filtering

The existence of spurious data resulting from the experiments undertook in the laboratorial environment lead to the development of several methods to handle it. Goring and Nikora (2002) developed an algorithm aiming to solve the problem of spurious points on ADV (Acoustic Doppler Velocimetry) data related to turbulence velocities in streams, which they called the phase-space thresholding method.

The phase-space thresholding method is an innovative method to deal with spurious points in

ADV data but results from three previous concepts: the differentiation enhances high-frequency components of a signal; the expected maximum of a sequence of random numbers is given by the universal threshold; and the good data is comprised inside a three dimensional phase-space cluster. This method was then adapted by Ferreira et al. (2009) to despike PIV data.

The method itself involves two steps. The first step stands for the detection of spurious spikes and then these spurious data is replaced by reliable data in a second step.

The algorithm starts by computing the mean values of instantaneous flow along the time and subtracting them from the effective values. After the data is subjected to this filtering process, these mean values are added to the remaining data.

Focusing on the detection problem, it was observed that when plotting velocities against its first and second order derivatives, the data remains in a three dimensional nut shell. It was obvious to the authors that an ellipsoid could be used to threshold the data detecting spurious points.

The construction of the so called ellipsoid results from a theoretical result from normal probability distribution theory. It defends that for a white Gaussian signal the expected absolute maximum is calculated by equation 5.17.

$$\lambda_U = \sqrt{2 \cdot ln(n_i)} \tag{5.17}$$

where λ_U is the so called Universal threshold and n_i is the number of iterations. When using a normal signal characterized by a certain standard deviation, σ, and with a mean value of zero, the expected maximum is calculated by equation 5.18.

$$\lambda_U \sigma = \sqrt{2 \cdot ln(n) \cdot \sigma} \tag{5.18}$$

The variables here, are the flow velocity time series u_i and, the first and second order, derivatives of it, respectively Δu_i and $\Delta^2 u_i$, calculated by equations 5.19 and 5.20.

$$\Delta u_i = (u_{i+1} - u_{i-1})/2 \tag{5.19}$$

$$\Delta^2 u_i = (\Delta u_{i+1} - \Delta u_{i-1})/2 \tag{5.20}$$

By computing its standard deviation it is possible to build a Universal threshold based on a three dimensional nut shell that may stand as the final boundary between good and bad data.

To build the ellipses it is even needed a rotation angle applied to it. The angle θ_R is calculated by equation 5.21, as shown above.

$$\theta_R = tan^{-1}\left(\frac{\sum u_i \cdot \Delta^2 u_i}{\sum u_i^2}\right) \tag{5.21}$$

The method principle is supported by the premise that reliable data lies within the cluster and every point that lies outside the same cluster is considered suspicious of being a spike. The

Fig. 5.8 shows a set of bad data *(a)* and a set of good data *(b)* achieved after using the so called phase-space thresholding method (Goring and Nikora, 2002).

In the spike replacement process there is not a so called perfect criterion because data cannot be truly replaced. This is a process that has to be done aiming to avoid damaging the reliable data at all costs. A very well accepted method is to replace the spikes by the smoothed estimate based on the neighbour points, but any criterion is suitable of being accepted. This particular criterion is suitable of reproducing spurious points from the spike itself.

According to Goring and Nikora (2002), the best option, when dealing with ADV data sampled at 25 to 100 Hz, is to use a third order polynomial through 12 points on either side of the spike. However, in the scope of this thesis the data was achieved through PIV means at a rate of 15 Hz, thus, it was applied a replacement criteria based on the average value calculated among the closest points.

It has to be highlighted that therefore the spike replacement is presented has an independent phase in the process, it is truly made in between spike detection iterations. Thus, each spike replacer is being evaluated in the subsequent iteration, under a new thresholding ellipsoid which is based on the remaining data, and is always suitable of being replaced again.

This method has the problem that, when there is a set of points that are suitable of being considered has spikes, they are well defined has spikes but cannot be replaced at all. When a spike is replaced in an iteration, this replacement criterion is influenced by its neighbours, that are spikes themselves, and there is a pathological problem because the replacer point is always continuing to be a spike in the subsequent iteration. This is why the number of spikes tends to a certain number of unresolved points instead of tending to zero and the number of iterations must be somehow limited.

5.5.4 Data treatment

The data resulting from the filtering process is reshaped into two three-dimensional matrices, representing the displacement where the two orthogonal axes stand for the spatial position and third direction represents the time. It means that each matrix slice represents the flow displacement field in a specific instant.

The previously computed calibration factor is then applied to the displacement matrices, in order to put all the data in I.S. units, meters in this case.

Several variables are stored in a $^*.mat$ file, including the proper matrices that represent the local displacements for each orthogonal direction, the calibration factor, the time-step between each point in the third direction of the matrices which is $\delta t_s = 1/15\,\mathrm{s}$, the time-step between each pair of images which is $\Delta t_s = 750\,\mu\mathrm{s}$, the number of runs for that particular experiment and the position code that is useful to name and identify files, among several other less important variables.

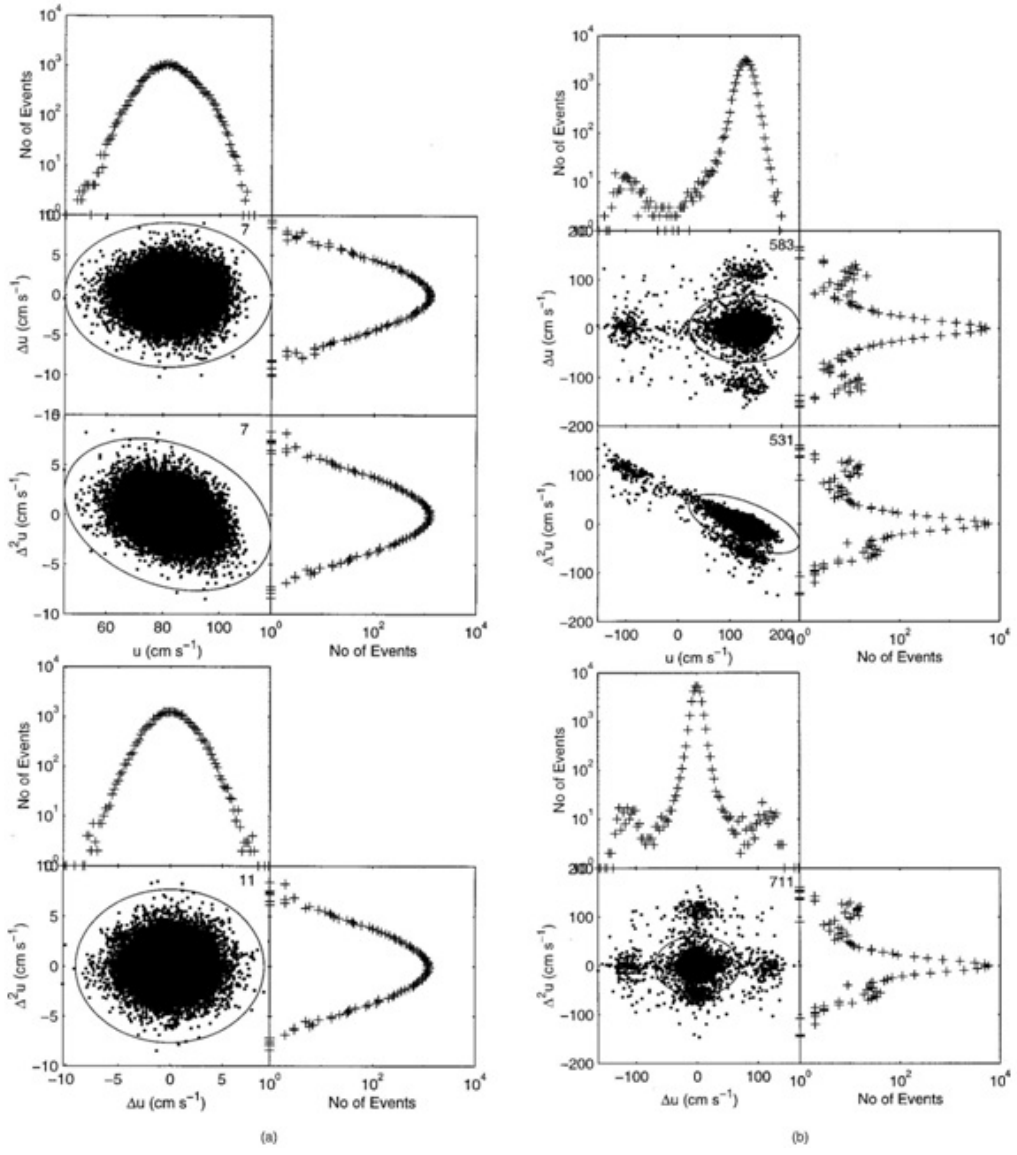

Figure 5.8: Already despiked data, at the left, is compared to raw data, at the right (Goring and Nikora, 2002).

Event detection

The Matlab script that computes the turbulent quantities starts by loading the respective run file, including the instantaneous displacement field matrices. The instantaneous flow velocity fields are calculated using equations 3.1 and 3.2, shown in chapter 3.1.

These matrices are commonly addressed as instantaneous flow velocity time series because the matrix third direction represents time and going through that direction, the happenings along the *"run"* duration may be noticed.

The first task lays on computing the average flow velocity field, which is calculated along the third component of each matrix and results in a pair of two-dimensional matrices, $\overline{u}$ and $\overline{w}$, as shown in equations 5.22 and 5.23.

$$\overline{u} = \frac{1}{N_{maps}} \cdot \sum_{i=1}^{N_{maps}} u_i(x,z) \tag{5.22}$$

$$\overline{w} = \frac{1}{N_{maps}} \cdot \sum_{i=1}^{N_{maps}} w_i(x,z) \tag{5.23}$$

where $\overline{u}$ and $\overline{w}$ stand for the average velocity fields, respectively. N_{maps} is the number of maps, which corresponds to the length of the matrix in the third direction and it is shown in Table 5.6, while $u(x,z)$ and $w(x,z)$ represent the flow velocity in each position in the matrix u and w.

The average calculations must consider that several positions in the matrices have *NaN* values (Not a Number) which introduces an error in the average. These elements which are introduced through the mask applied earlier, must be neglected in the calculation of the average. The obtained average maps $\overline{u_r}$ and $\overline{w_r}$ are then subtracted from every slice of the u and w matrices, achieving the fluctuation instantaneous flow velocity fields, u' and w', as shown in equations 5.24 and 5.25.

$$u' = u_i - \overline{u} \tag{5.24}$$

$$w' = w_i - \overline{w} \tag{5.25}$$

It is built a three-dimensional matrix, $u'w'$ by multiplying the u' by w', element by element. This corresponds to a shear stress time series along the third matrix axis, for every spatial position of the matrix.

The quadrant threshold analysis is initiated by calculating the constants involved. These constants are σ_h, σ^+ and σ^- and they represent the thresholds that establish the boundaries between the considered data and the negligible data, which stands in the isotropic region, by applying the criteria presented in chapter 2. These values are computed for each matrix spatial position and are presented in the form of bi-dimensional matrices. The thresholds σ_h, σ^+ and σ^- remain constant for each run file and they are achieved as presented in equation 2.3, from chapter 2 and equations 5.36 and 5.37, from this chapter.

To help in the event detection, four matrices, Q_{out}, Q_{ej}, Q_{in} and Q_{sw}, were produced, corresponding to the four kinds of events, such as outward, ejection, inward and sweep events, that are the same size of $u'w'$ but holding ones or zeros in each element. The ones stand for every position where the correspondent event occurs. These matrices will later be used as filtering masks when compared to the shear stress time series matrix, to keep only the desired event amongst all. These matrices are built according to the conditional sampling applied to the correspondent event, as explained in chapter 2.4.

After detecting events, and for each sort of event, several parameters are subject to be computed, such as, Duration (T_k), Transported momentum (M_k), maximum Reynolds shear stress (A_k) and Period (P_k). The filtering masks are applied to the $u'w'$ separating each kind of events and then the the characteristics of each single event are calculated.

As a first approach, V_t and V_{uw}, respectively the abscissas and ordinates referring to each particular k event. Once having these data it is simple to compute the desired parameters for each k event.

The event duration, T, is computed by subtracting the lowest to the highest abscissa in V_t. The maximum shear stress, A, is calculated by finding the maximum value in the ordinates V_{uw}. The transported momentum, M, results from computing the area delimited by the function defined by the set of abscissas and ordinates that define each event, respectively V_t and V_{uw}.

To calculate M it was used the trapezoidal rule embedded in a Matlab function, as shown in equation 5.26, and the *period P* is computed in two separate ways. In one hand, it represents the time between maximum values of consecutive events, as in 5.28 and in the other hand, it represents the time between centroids of consecutive events, as shown in equation 5.29. The event centroid position C_x is computed by using the following equation 5.27.

$$M = \sum \frac{(b_{i+1} - b_i)}{2} \cdot (t_{i+1} - t_i) \tag{5.26}$$

$$C_{xk} = \frac{\sum_{i=1}^{n} (x_i + x_{i+1}) \cdot [x_{i+1} \cdot y_i - x_i \cdot y_{i+1}]}{6 \cdot \Omega} \tag{5.27}$$

where Ω is the area inside the polygon that define each event. And x_i and y_i represent, respectively, the array with the abscissas and the respective ordinates of the same event. This algorithm requires the input of all the polygon vertices and it must be closed.

$$P_m = t_{k+1} - t_k \tag{5.28}$$

$$P_c = C_{xk+1} - C_{xk} \tag{5.29}$$

where k stands for the identification of each event.

Fig. 5.9 shows the physical definition of the parameters which are considered to characterize the events in the flow.

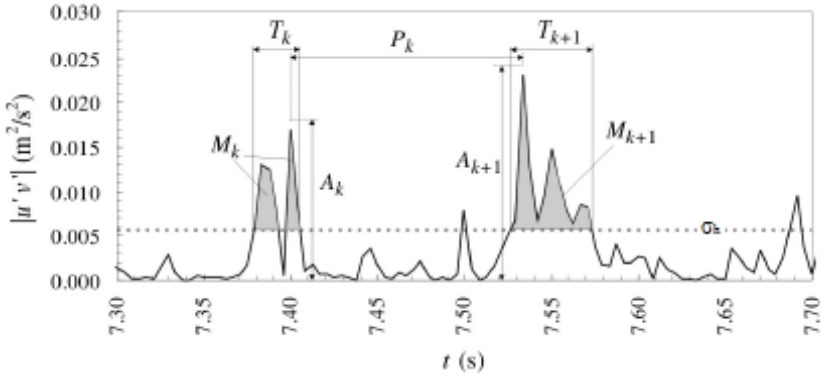

Figure 5.9: Definition of the parameters that characterize events in a $u'w'$ time series. The figure corresponds to the data in a unique reference position plotted against time. Adapted from Ferreira et al. (2009).

Because this process is a time consuming task, it is only performed for ejection and sweep events. These parameters are stored in a data structure with the abscissa and ordinate arrays for each k event distributed trough every spatial position (m,n).

Data interpolation

The available data correspond to values of displacement in particular instants, separated by a small time interval. However, an interpolation method must be performed in order to find the interception of the data with a considered threshold. A linear interpolation appears to be a wise decision, because it is completely unknown how a function of this nature behaves.

A way to decrease the importance of this particular problem would be increasing the data acquisition frequency during the laboratory experiment, because with a higher frequency there would be more points in each event set and consequently decreasing the error. However, the employed acquisition method, PIV, is limited to 15 Hz which corresponds to the frequency used in these laboratorial experiments.

Based on the previous explanation, a possible solution lays on linearly interpolate the data in the initiation and finishing coordinates of each event. Fig. 5.10 presents a detailed section of a time series, which corresponds to the evolution of the flow velocity with time, for a particular spatial position.

Because the time series matrix $u'w'$ results from the multiplication of the u'_i by w'_i element by element, these matrices elements are subject of being plotted against each other, as applied in the quadrant threshold analysis. Using this plot, a linear relation can be established between both extreme points of each segment to be interpolated, in this case initial and ending segments. A segment between two consecutive points in the quadrant analyses plot is related to the time interval between data points in the $u'w'$ time series. Thus, the distance between the two points, P_1 and P_2, in the quadrant analysis is measured and compared to the time interval that separates both points in the shear stress time series. This is illustrated in Fig. 5.11.

The implementation of this method consists of, for each event, consider its first point and the previous one, as shown in Fig. 5.11, plotting U'_i against W'_i. f_1 is the function that defines the

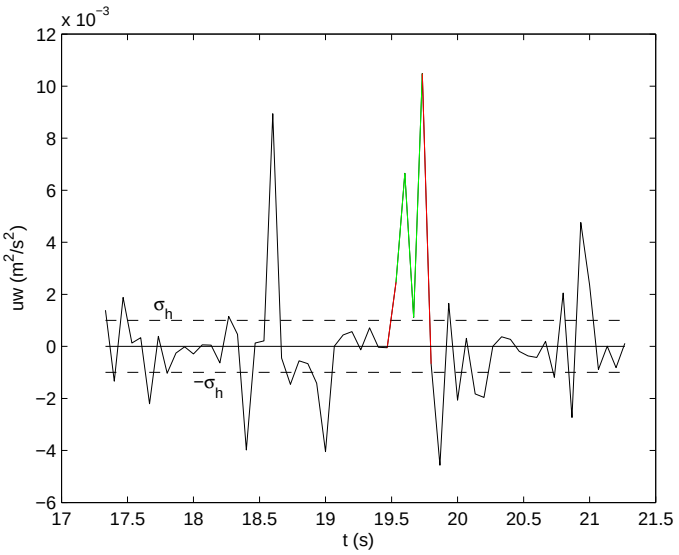

Figure 5.10: Detailed event in a time series. The red segments have to be sliced because the event only starts over the threshold. Green segments are intermediate data.

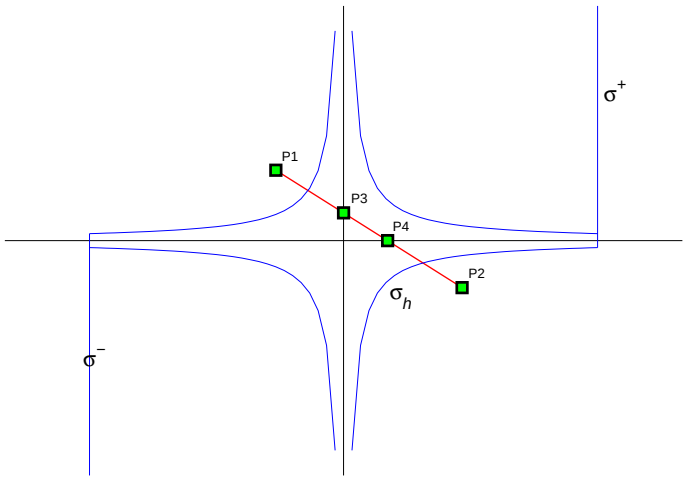

Figure 5.11: Quadrant plot of the initial segment of an event. P2 is in the sweep event area but the sweep event starts with the interception between the segment P1P3 and the threshold σ_h.

straight line which intercepts both points, P_1 and P_2 and it is represented by equation 5.30.

$$f_1 = w' = s \cdot u' + w'_0 \tag{5.30}$$

where s is the function slope which results from the following equation 5.31

$$s = \frac{P_{2w'} - P_{1w'}}{P_{2u'} - P_{1u'}} \tag{5.31}$$

Functions f_2 and f_3, shown in equations 5.32 and 5.33, represent the thresholds of the considered quadrant. f_2 is controlled by σ_h, f_3 is controlled directly by σ^+ or σ^- depending on the quadrant.

$$f_2 = w' = \frac{\sigma_h}{u'} \tag{5.32}$$

$$f_3 = \sigma^- or f_3 = \sigma^+ \tag{5.33}$$

The interceptions between f_1 and, f_2 or f_3, are considered and it is chosen the interception point, t_x, which is the one existing in the interval $[P_1, P_2]$ and closer to point P_2, if there is more than one interception point in that interval. P_2 is the point of the interval that clearly belong to the considered segment.

Regarding to the data acquisition period, $\delta t_s = 1/15\,s$ and that this time period corresponds to the distance between P_1 and P_2, time period equivalent to the distance between P_2 and t_x can be achieved and it is represented by $\delta t^{'}$, as shown in equation 5.34.

$$\frac{\delta t^{'}}{\Delta P_2 t_x} = \frac{\delta t}{\Delta P_2 P_1} \rightarrow \delta t' = \frac{\delta t \cdot \Delta P_2 t_x}{\Delta P_2 P_1} \tag{5.34}$$

Achieving this new initial point, it is added to the vectors that define the abscissas and ordinates of the event concerned. The new value t_0 added to the abscissas vector is calculated in 5.35, and in the ordinates vector it is added a 0 in the same position.

$$t_0 = P_2 - \delta t^{'} \tag{5.35}$$

This procedure is also made in the other extremity of the event concerned, resulting in a rebuild of the two vectors that define the abscissas and ordinates of each event.

Sensitivity analysis

Before running the event detection script, previously described, a sensitivity analysis over the behaviour of transported momentum with the value of the hole size was carried out. This value sets the positioning of the threshold σ_h in the quadrant analysis and it is important to establish the boundaries to the event detection and validation.

This sensitivity test performs the event detection as previously described, but computing only the transported momentum (M_k) of each event. These calculations are made inside a loop that goes through a continuous increase of the hole size value, H, starting in zero and ending in 3 with a step of 0.1.

The events cumulative values of the transported momentum are stored in four matrices, each one for a kind of event, where the orthogonal direction represents the value of H, continuously increasing. The first and second directions are kept to spatial locations. These matrices are then expressed in rate of transported momentum dividing them by the total transported momentum of the correspondent spatial position (m,n) which was produced during the experiment. This approach compares the persistence of each kind of event in the experiment sample.

The choosing process for the hole size value is based on the rate of outward and inward inte-

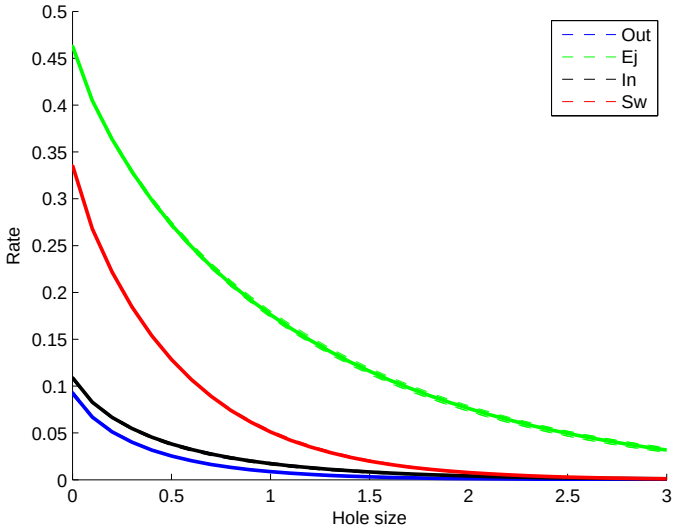

Figure 5.12: Example of a sensitivity curve of the transported momentum to the hole size.

ractions. It was set that the hole size must correspond to a rate of outward and inward interactions of 10%. This is a task that depends on the user sensitivity.

After averaging the five H values, the average hole size is used to compute the σ_h value, the threshold applied in the event detection and consequently in the identification of the parameters that characterize the flow.

Two other thresholds are introduced in the event detection criteria, which are described in chapter 2.4. The thresholds σ^+ and σ^- depend on the u' value and are kept constant for each of the experiments. They are calculated as shown in equations 5.36 and 5.37.

$$\sigma^+ = 2.5 \times u_{rms} \tag{5.36}$$

$$\sigma^- = -2.5 \times u_{rms} \tag{5.37}$$

Event Statistics

The event statistics are computed using the data structures build in the event detection phase. To compute the event statistics, the script inputs the data previously stored in the event detection phase, such as, the data structures and the matrix with the number of events in each data structure position. These data structures carry the vectors that define each k event and its characterization by maximum shear stress (A_k), transported momentum (M_k), duration (T_k) and period calculated in the two different ways, P_{ck} and P_{mk}, respectively calculated between consecutive events centroid and maximum value.

In this phase data from both tests S3 and S4, respectively for mobile and immobile bed conditions, are input regarding to combine ejection and sweep events from the same spatial position. In each sort of event both tests parameters are considered and placed in histograms that compare them statistically. Figure 5.13 presents an example of a histogram showing the parameters which are being analysed for a reference point standing in the pythmenic region of the flow structure.

The histograms are built accordingly to the Matlab histogram embedded function using 10

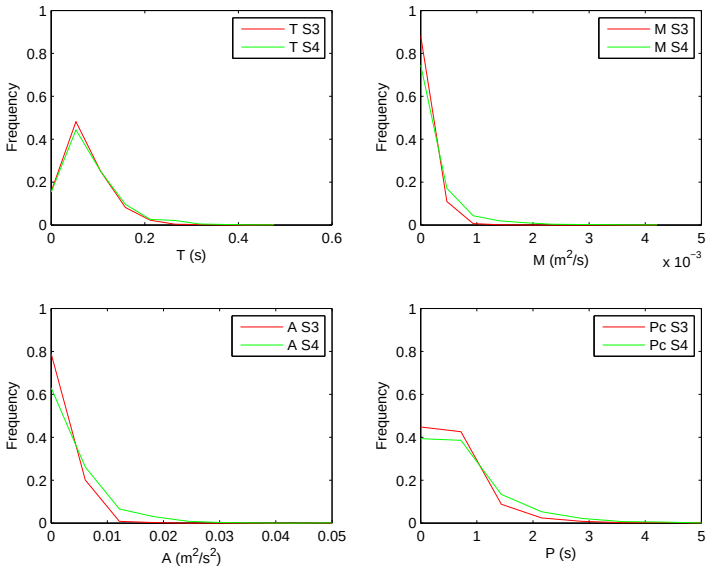

Figure 5.13: Example histograms of duration (T), maximum shear stress (A), transported momentum (M) and period (P), of sweep events at reference point $(5,4)$. Comparison of data sets S4, immobile bed in green and S3, mobile bed in red.

bins. The number of bins results from a heuristically attempt to provide a smooth curve. The bins size, h_b, is set in function of the maximum value of the considered parameter, between both tests, S3 and S4, as shown in equation 5.38.

$$h_b = \frac{max\{X^{S3}, X^{S4}\}}{Nr.Bins} \tag{5.38}$$

where X stands for the parameter that is being considered, with superscript indicating tests, S3 and S4, and the *Nr.Bins* is 10 as previously stated.

Chapter 6

Results and Discussion

6.1 Introduction

The approach followed to compare the differences between flows with and without sediment transport comprises two steps. Firstly, a sensitivity analysis on how the transported momentum is affected by the hole size in the quadrant threshold analysis. Then, the statistical distribution of the considered parameters that characterize sweep and ejection events are assessed in both immobile and mobile bed conditions.

The statistical distribution of the parameters was performed with dimensional and non-dimensional values. The non-dimensional parameters can be divided in two different analysis resulting from the use of two normalizing factors, as it will be explained in chapter 6.4.

These analysis were made for several points of the flow velocity maps. The considered points are identified in Fig. 6.1, regarding immobile bed conditions, and in Fig. 6.2, for mobile bed conditions.

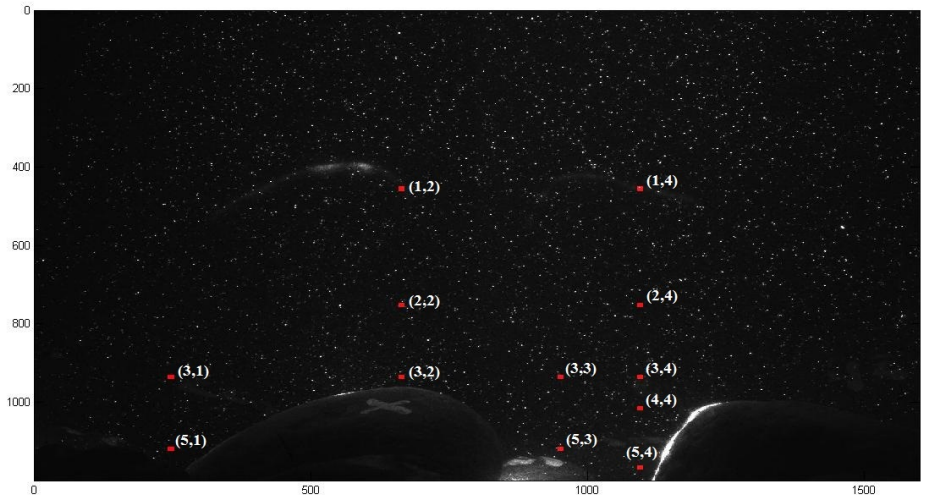

Figure 6.1: Location of the reference points considered in test S4, in immobile bed conditions

The points considered for results were chosen accordingly to the physical system proposed by

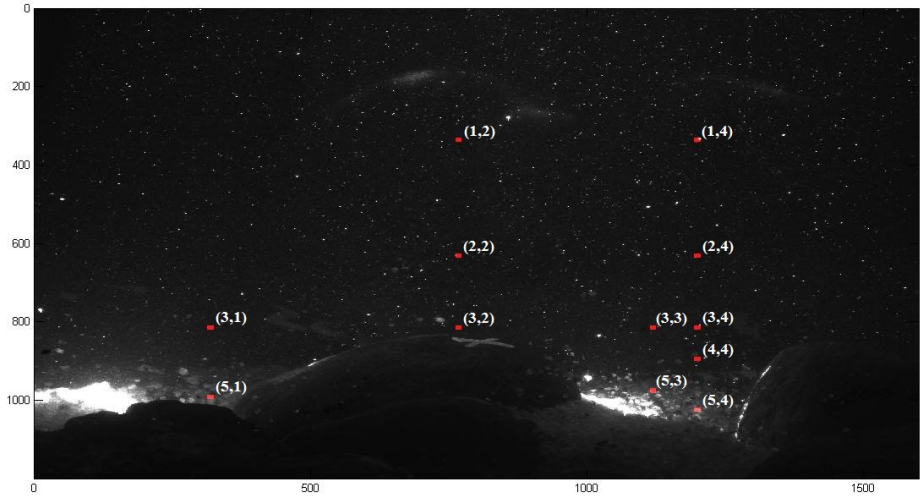

Figure 6.2: Location of the reference points considered in test S3, in mobile bed conditions

Ferreira et al. (2012) which is indicated for porous mobile beds in steady free-surface flows with transported sediments as bed load.

The points marked as (1,2) and (1,4) were adopted because they are far enough from the bed, standing clearly in the outer region where the flow structure does not depend on the wall. Points (2,2) and (2,4) coincide with the logarithmic region, which in the Ferreira et al. (2012) corresponds to the interception between the outer layer and the inner layer regions. Points (3,1), (3,2), (3,3) and (3,4) are standing at the highest crest level at the interface between inner and pythmenic layers. They can evaluate the influence over the flow, caused by the crest itself and by the mobile bed effects. Other points were chosen into the troughs and because they are undoubtedly in the pythmenic layer they establish a comparison between the effect of the trough itself and the effect of a mobile bed. Point (4,4) was considered because it is standing in the trough but not close to the bed. The effects of the hiporeic and pythmenic regions can be noticed in points (5,1), (5,3) and (5,4) because they were chosen at the closest available points to the bed, where data is acquirable by PIV means.

Despite the flow was analysed at all of these reference points by the following methods, only five points are presented in detail, which are (1,4), (3,2), (3,3), (5,3) and (5,4). These five points constitute a sample of the remaining points, as they stand in different regions of the flow and are representative of the remaining ones.

6.2 Sensitivity analysis

In this chapter it is intended to relate the sensitivity of the transported momentum with the value of the hole size. The value of H is increased between 0 and 3 at a rate of 0.1 while the values of transported momentum are being registered. These results are shown as follows for a point in each of the considered regions.

(1) In the outer region

In the outer region, the evaluation of the hole size shows that the flow is mainly governed by ejection events. The sweep events also stand out but those are not as important as ejection events in the turbulence production processes. By comparing Fig. 6.3(a), without bed load, to Fig. 6.3(b), where bed load is present, it is obvious that they are very similar, supporting the thesis that in the outer region the flow is controlled by the free-surface conditions, remaining undisturbed independently of the conditions of the bed.

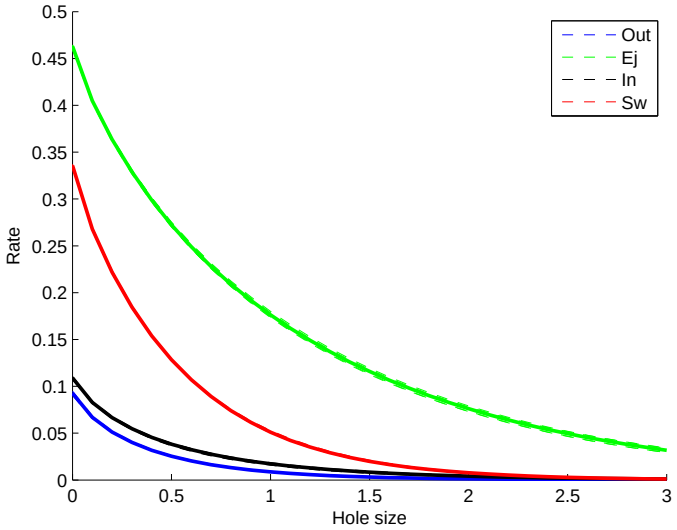

(a) S4 - Immobile bed

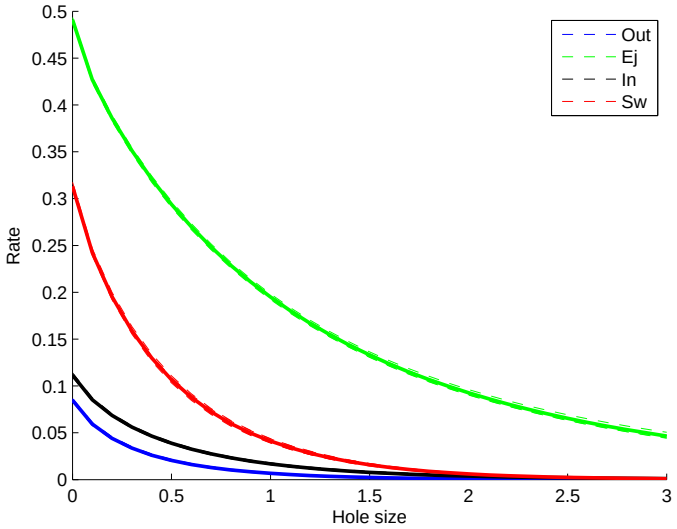

(b) S3 - Mobile bed

Figure 6.3: Hole size sensitivity analyses to transported momentum in position (1,4)

(2) Over the crest, in the overlapping between inner and pythmenic regions

Fig. 6.4(a) and Fig. 6.4(b) show the shear stress over the crest in the nearest measured point, respectively, for immobile and mobile bed conditions. According to Ferreira et al. (2012) it corresponds to the region where inner and pythmenic regions characteristics are governing the flow. They show that the importance in the shear stress production processes is transferred from ejection and sweep events to outward and inward events, which results in a tendency to isotropy in the quadrant threshold analysis. This is stated for both cases of immobile and mobile bed conditions.

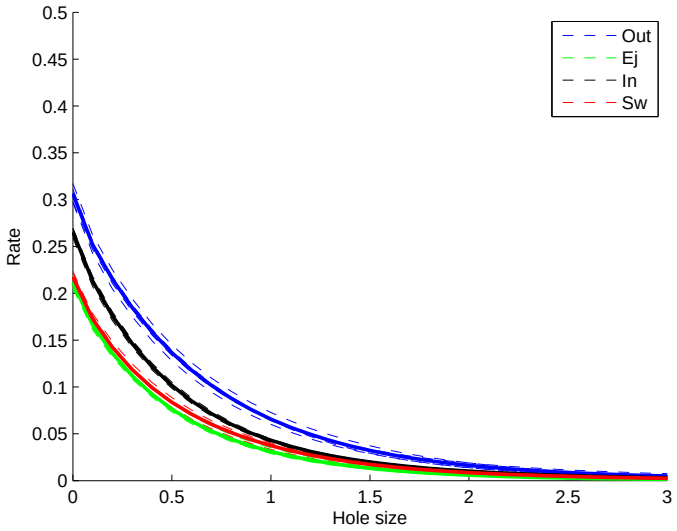

(a) S4 - Immobile bed

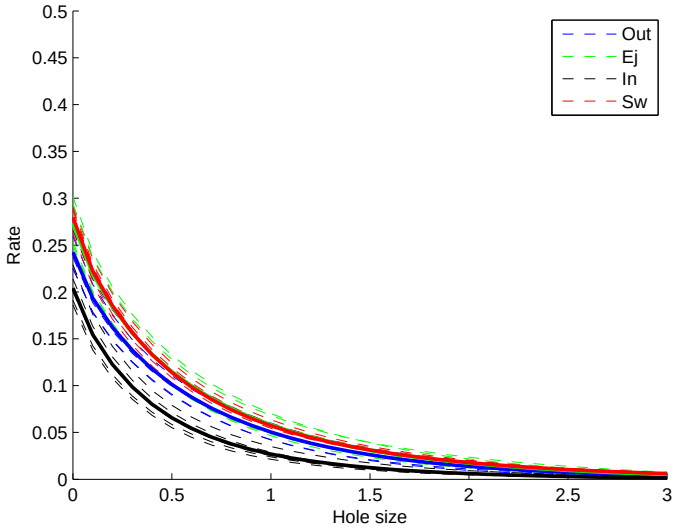

(b) S3 - Mobile bed

Figure 6.4: Hole size sensitivity analyses to transported momentum in position (3,2)

(3) At the crest level but over the through

This reference point stands in the overlapping between inner and pythmenic regions but over

the through. The quadrant threshold analysis at this point shows a clear reorganization of the flow, with ejection and sweep events assuming responsibilities in the shear stress production process. The mobile bed does not seem to affect the flow organization at this level, over the trough as it is presented in figures 6.5(a) and 6.5(b), respectively for immobile bed and mobile bed conditions.

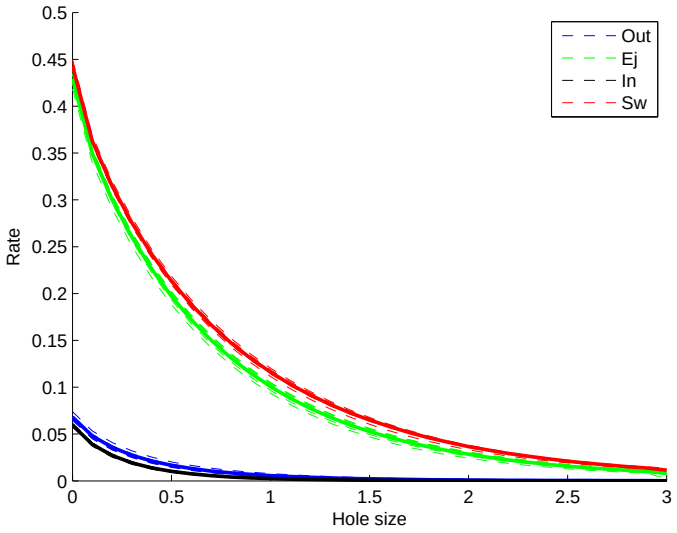

(a) S4 - Immobile bed

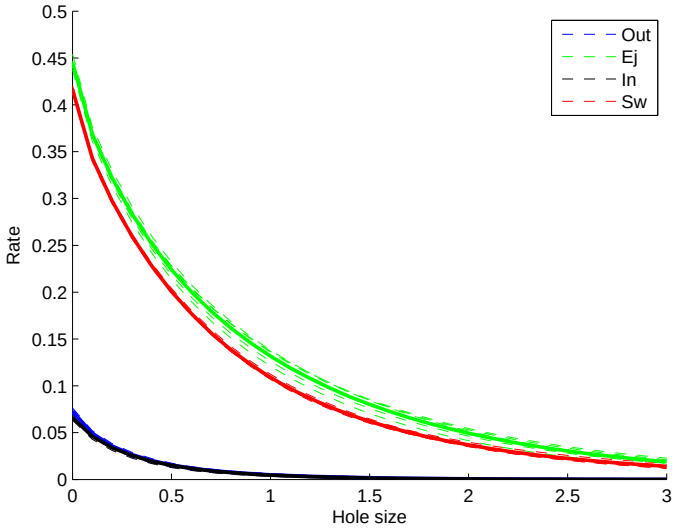

(b) S3 - Mobile bed

Figure 6.5: Hole size sensitivity analyses to transported momentum in position (3,3)

(4) In the pythmenic region

At this point, standing clearly in the pythmenic region, considering immobile bed conditions, the ejection and sweep events share importance in shear stress production processes. However, when in mobile bed conditions, the ejection event decreases its contribution to the shear stress production processes while sweep events stand out and assumes a main role in the same processes

as shown in Fig. 6.6(a) and Fig. 6.6(b), respectively for immobile bed and mobile bed.

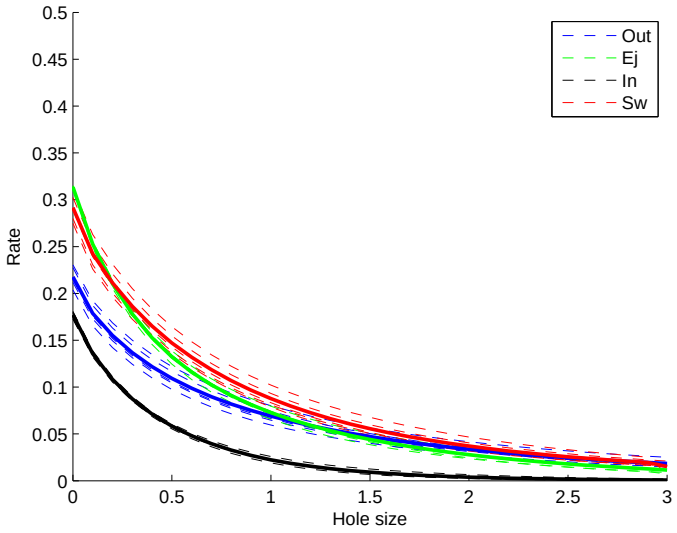

(a) S4 - Immobile bed

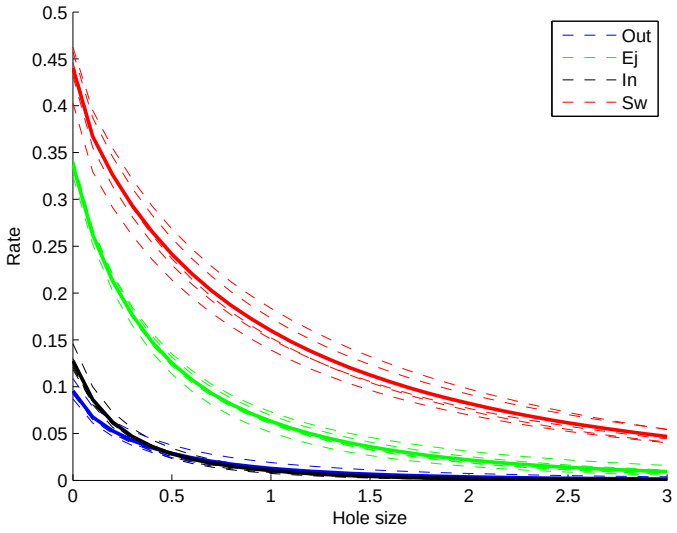

(b) S3 - Mobile bed

Figure 6.6: Hole size sensitivity analyses to transported momentum in position (5,3)

(5) In the overlapping between pythmenic and hiporeic regions

Fig. 6.7(a) and Fig. 6.7(b), respectively standing for immobile and mobile bed conditions, show the sensitivity analysis of the transported momentum to the hole size in the deepest trough. At this level, the flow is governed by the characteristics of both the hiporeic and pythmenic regions.

Fig. 6.7(a) shows that in immobile bed conditions, the sweep events assume the major contributions to the shear stress production processes, and they even increase their contribution in the mobile bed case, as shown in Fig. 6.7(b). However, in immobile bed conditions, contributions

from ejection and inward events cannot be neglected at all as they stand out from the outward events.

Despite this reference point is placed in front of a pebble, the flow presents characteristics similar to those found at other reference points placed in the trough, however it is more clear at this reference point. For example, in comparison with the reference point shown previously in Fig. 6.6(b) where sweep events assume clearly the main contribution the shear stress production, when in mobile bed conditions.

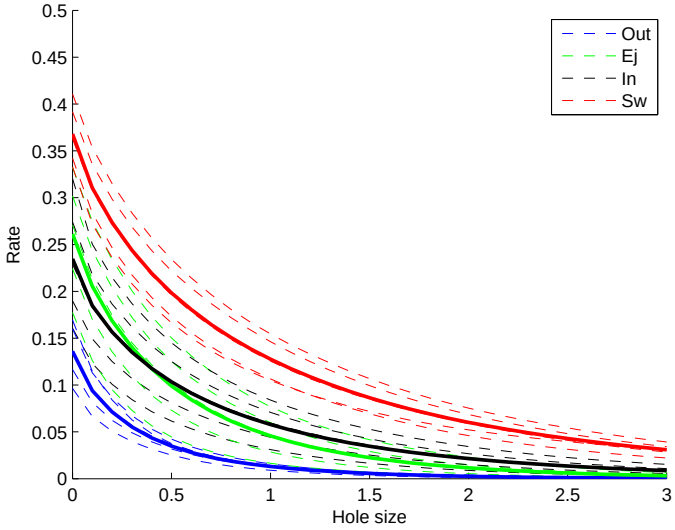

(a) S4 - Immobile bed

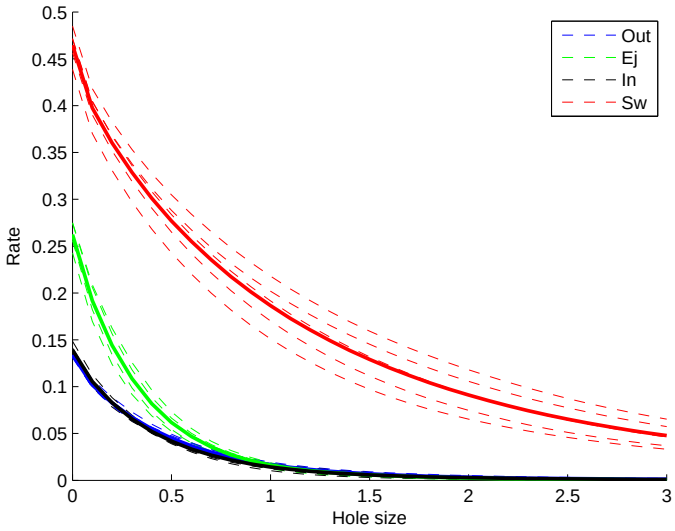

(b) S3 - Mobile bed

Figure 6.7: Hole size sensitivity analyses to transported momentum in position (5,4)

6.3 Statistical analysis of ejection and sweep events

As the value of the hole size is important to establish a threshold in the quadrant analysis method, it was chosen based on a criteria that makes a correspondence between the percentage of outward and inward interactions that remain above a certain threshold which depends on the hole size.

The used criteria was to choose a hole size which considers that the transported momentum produced by outward and inward interactions is not greater than 10% of the its total value at that reference point. The adopted hole size corresponds to a value of $H = 0.4$ and this hole size was used to compute the statistics of ejection and sweep events shown in the remaining results.

As a first approach, the average and extreme values of the considered parameters, namely, event duration, maximum shear stress, transported momentum and period, were considered and analysed. Then, a statistical analysis was employed to complete the characterization of the flow.

The ejection and sweep events were computed for mobile and immobile bed, obtaining the statistical distribution of flow parameters that characterize these events and allowing to compare them between the experiments in both bed conditions.

The comparative analysis is made at the same reference points as in sub-chapter 6.2, but now regarding a statistical approach as previously explained.

(1) In the outer region

Fig. 6.8 presents the statistics of the parameters from ejection events at the first reference point, which clearly stands in outer region, comparing both immobile and mobile bed conditions. In Fig. 6.9, the same parameters statistics are presented for sweep events.

Table 6.1 shows the average and maximum values of the same parameters, for both ejection and sweep events.

Tabela 6.1: Average and extreme values of the parameters calculated at reference point (1,4) in both mobile (S3) and immobile (S4) bed conditions. Where T represents the duration, A is the maximum shear stress, M is transported momentum and P is the period of events.

Reference point (1,4)					
Ejections					
		T (s)	A (m^2/s^2)	M (m^2/s)	P_c (s)
Average	S3	0.0875	0.0046	0.0003	0.6123
	S4	0.0918	0.0087	0.0006	0.6017
Maximum	S3	0.4403	0.0319	0.0037	4.0565
	S4	0.4884	0.0668	0.0101	3.9881
Sweeps					
		T (s)	A (m^2/s^2)	M (m^2/s)	P_c (s)
Average	S3	0.0758	0.0018	0.0001	0.5438
	S4	0.0848	0.0048	0.0003	0.5563
Maximum	S3	0.4369	0.0132	0.0011	4.4605
	S4	0.4849	0.0336	0.0035	4.3029

At this reference point ejection and sweep events behave equally when switching from an immobile to a mobile bed. In table 6.1, the values of T and P do not present important changes but

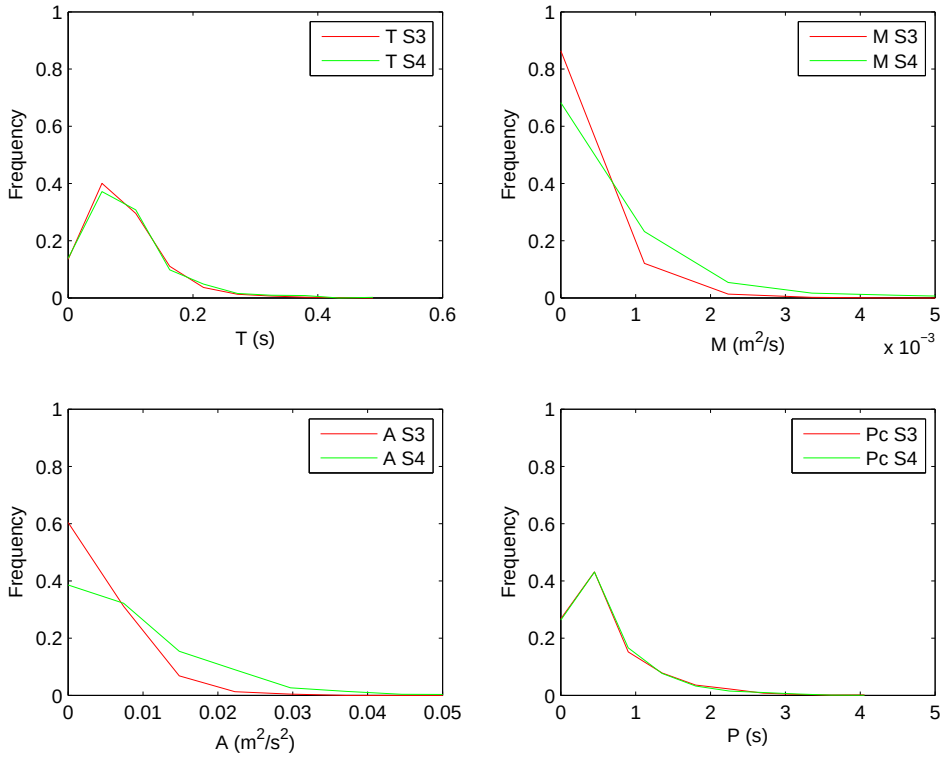

Figure 6.8: Histograms of duration (T), maximum shear stress (A), transported momentum (M) and period (P), of ejection events at reference point $(1,4)$. Comparison of data sets S4, immobile bed in green and S3, mobile bed in red.

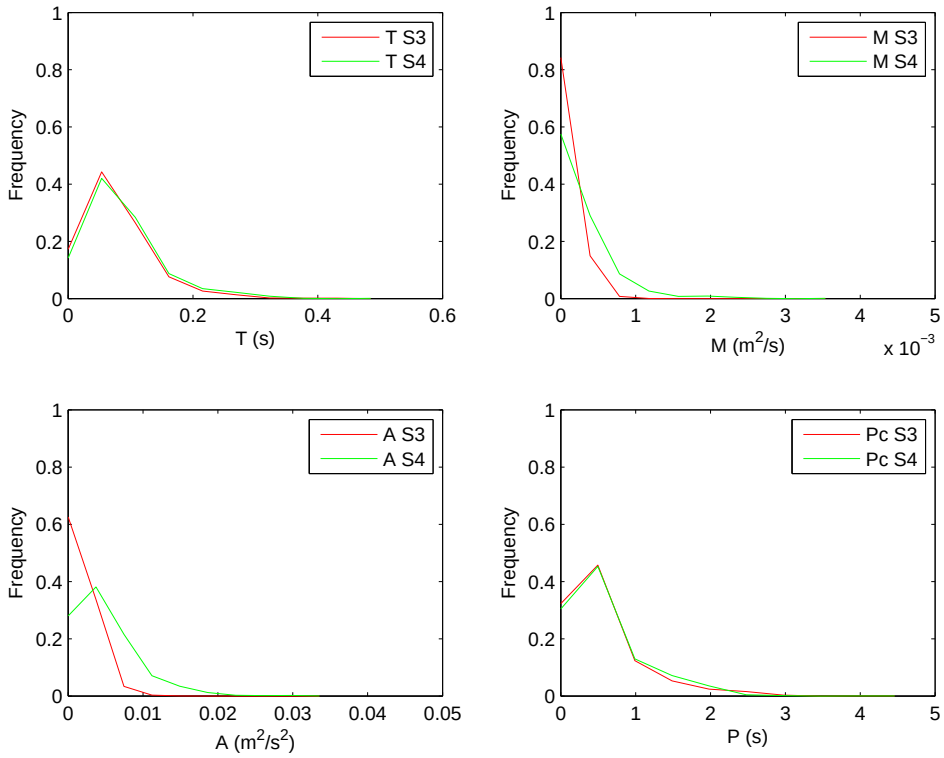

Figure 6.9: Histograms of duration (T), maximum shear stress (A), transported momentum (M) and period (P), of sweep events at reference point $(1,4)$. Comparison of data sets S4, immobile bed in green and S3, mobile bed in red.

the values of A and M, in both ejection and sweep events, present a clear decreasing of around an half. This is supported by the histograms presented in Fig. 6.8 and Fig. 6.9 where T and P remain similar, when comparing immobile to mobile bed while A and M show a deflection to the left. This behaviour indicates that in the experiment with bed load, the events in general have lower maximum shear stress and transported momentum.

(2) Over the crest, in the interception between outer and inner regions

Fig. 6.10 and Fig. 6.11 represent the statistical distribution of the parameters over the crest, respectively for ejection and sweep events.

Looking at Fig. 6.10, it is observed a deflection to the left in the parameters A and M, when switching from immobile to mobile bed conditions, in accordance with the reference position standing in the outer region.

Tabela 6.2: Average and extreme values of the parameters calculated at reference point (3,2) in both mobile (S3) and immobile (S4) bed conditions. Where T represents the duration, A is the maximum shear stress, M is transported momentum and P is the period of events.

Reference point (3,2)					
Ejections					
		T (s)	A (m^2/s^2)	M (m^2/s)	P_c (s)
Average	S3	0.0671	0.0019	0.0001	0.7009
	S4	0.0638	0.0036	0.0002	0.6719
Maximum	S3	0.3675	0.0157	0.0013	4.6834
	S4	0.3083	0.0525	0.0020	5.8695
Sweeps					
		T (s)	A (m^2/s^2)	M (m^2/s)	P_c (s)
Average	S3	0.0669	0.0018	0.0001	0.6549
	S4	0.0654	0.0041	0.0002	0.6962
Maximum	S3	0.3934	0.0195	0.0019	4.1579
	S4	0.4058	0.0455	0.0037	5.1745

At this reference position, table 6.2 shows that the duration of events do not present major differences between immobile and mobile conditions, but the frequency of sweep events slightly increases and the frequency of ejection events slightly decreases.

It is also noticed that, at this reference position, the average values of the parameter M are generally lower, if compared to reference position $(1,4)$.

(3) At the crest level but over the through

This reference point stands in the region governed by characteristics of the inner and pythmenic layers. At this reference point, the flow does not seem to be perturbed by the sediment bed load, as shown previously in Fig. 6.5(a) and Fig. 6.5(b).

Table 6.3 is consistent with it by showing a slight increase in the average values of event duration and period. However, the average values of maximum shear stress and transported momentum in both ejection and sweep events, show a decrease of about an half while switching from immo-

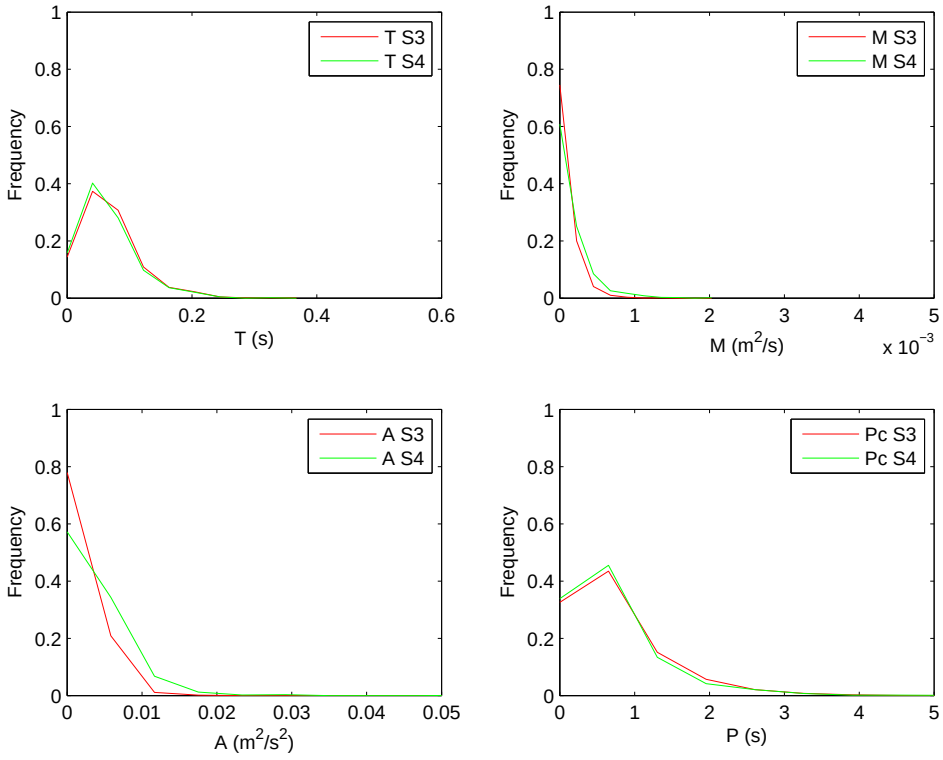

Figure 6.10: Histograms of duration (T), maximum shear stress (A), transported momentum (M) and period (P), of ejection events at reference point $(3, 2)$. Comparison of data sets S4, immobile bed in green and S3, mobile bed in red.

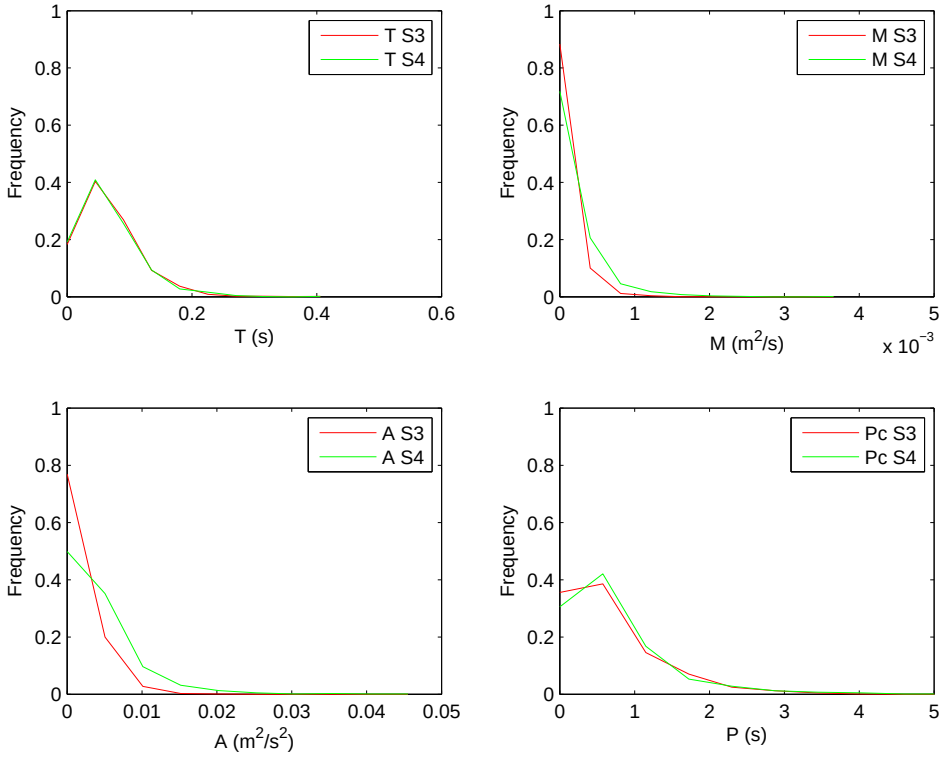

Figure 6.11: Histograms of duration (T), maximum shear stress (A), transported momentum (M) and period (P), of sweep events at reference point $(3, 2)$. Comparison of data sets S4, immobile bed in green and S3, mobile bed in red.

bile bed conditions to the sediment bed-transport case.

Tabela 6.3: Average and extreme values of the parameters calculated at reference point (3,3) in both mobile (S3) and immobile (S4) bed conditions. Where T represents the duration, A is the maximum shear stress, M is transported momentum and P is the period of events.

Reference point (3,3)					
Ejections					
		T (s)	A (m^2/s^2)	M (m^2/s)	P_c (s)
Average	S3	0.0737	0.0056	0.0003	0.4805
	S4	0.0717	0.0091	0.0005	0.4232
Maximum	S3	0.4732	0.0481	0.0035	3.2573
	S4	0.5101	0.0586	0.0063	2.9300
Sweeps					
		T (s)	A (m^2/s^2)	M (m^2/s)	P_c (s)
Average	S3	0.0755	0.0045	0.0003	0.4728
	S4	0.0725	0.0107	0.0005	0.4454
Maximum	S3	0.4904	0.0357	0.0036	4.0010
	S4	0.3483	0.0762	0.0076	4.4043

Regarding the extreme values of the four parameters analysed, the maximum shear stress and transported momentum values keep the behaviour from the average values, while the event duration slightly increases in the sweep event case and decreases for ejections. The maximum values of period invert, as it decreases for sweep events and present an increase for ejection events.

Fig. 6.12 is in accordance with Table 6.3, in the way that ejection durations and frequency of occurrence are not perturbed at all, by mobile bed. Values of A and M show a deflection to the left, when in mobile bed conditions, which indicates a clear decrease in the maximum shear stress and transported momentum values, even with the duration remaining still.

Fig. 6.13 shows a similar behaviour between sweep and ejection events.

(4) In the pythmenic region

This reference point stands in the layer where inner and pythmenic regions characteristics coexist, but in the trough.

In Table 6.4 it can be attested that a slightly decrease in the frequency of ejection events is followed by an average duration slightly lower when comparing test S4 to S3.

The greatest difference remains in the extreme values, those present a decreasing in the ejection event duration which is not followed by a decreasing in the frequency of the same event. The values of A and M, maximum shear stress and transported momentum, respectively, present a general and marked decrease between immobile and mobile bed conditions.

By analysing Fig. 6.14 the same characteristics are attested. The duration, T, shows a deviation to the left while in mobile bed case and it is in agreement with period, P, which indicates an increase in the frequency of ejection events. It can be interpreted as if the mobile bed splits

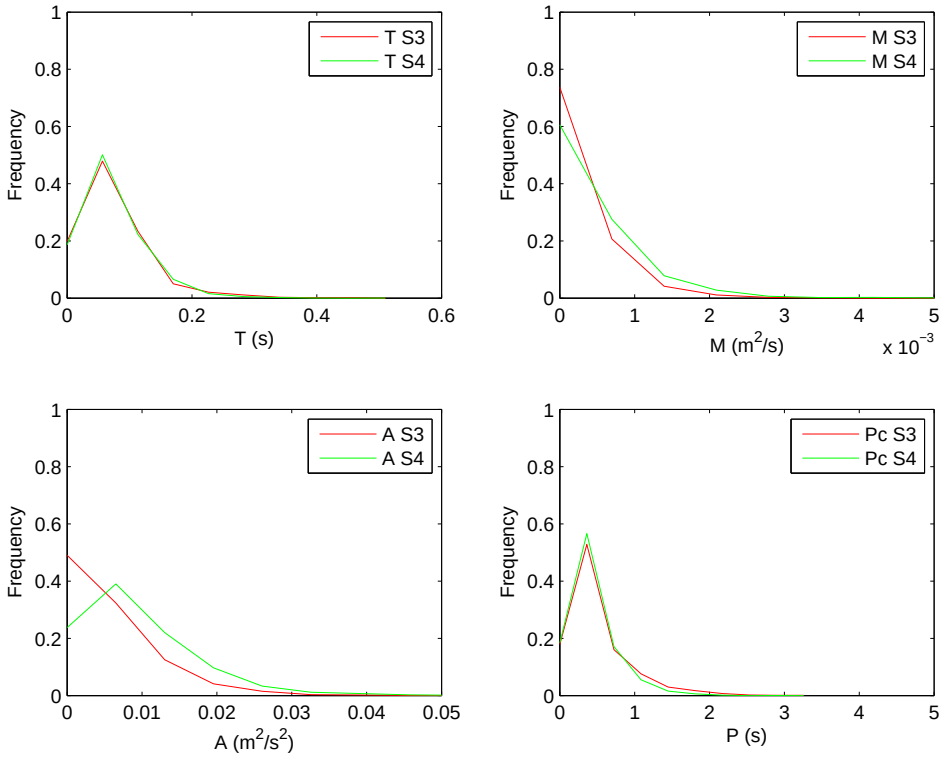

Figure 6.12: Histograms of duration (T), maximum shear stress (A), transported momentum (M) and period (P), of ejection events at reference point $(3,3)$. Comparison of data sets S4, immobile bed in green and S3, mobile bed in red.

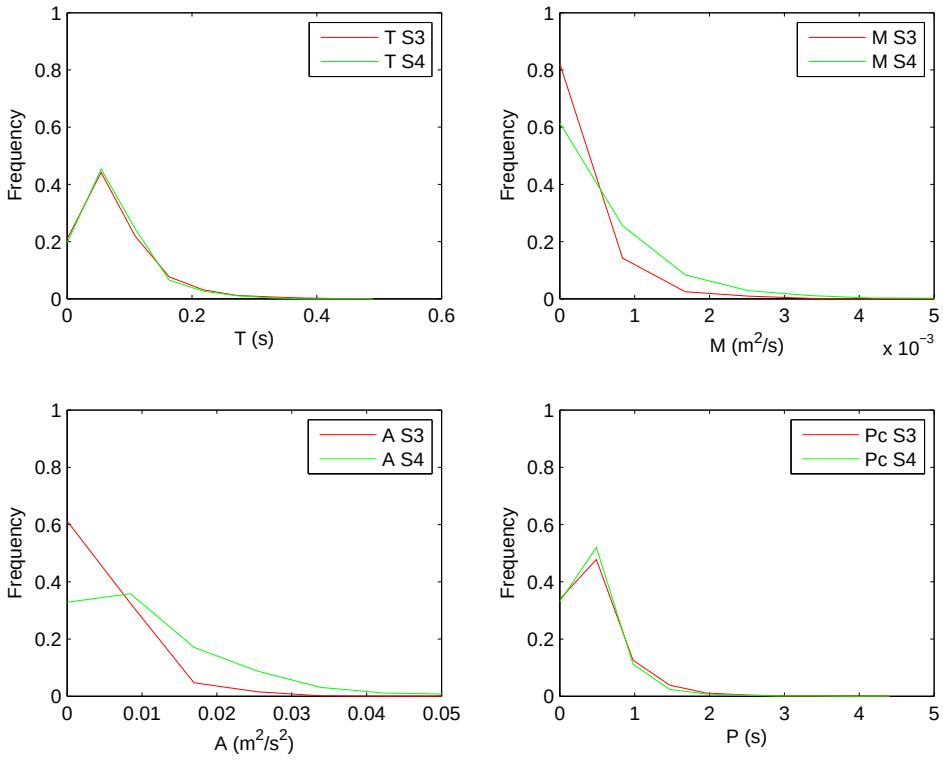

Figure 6.13: Histograms of duration (T), maximum shear stress (A), transported momentum (M) and period (P), of sweep events at reference point $(3,3)$. Comparison of data sets S4, immobile bed in green and S3, mobile bed in red.

Tabela 6.4: Average and extreme values of the parameters calculated at reference point (4,3) in both mobile (S3) and immobile (S4) bed conditions. Where T represents the duration, A is the maximum shear stress, M is transported momentum and P is the period of events.

Reference point (5,3)					
Ejections					
		T (s)	A (m^2/s^2)	M (m^2/s)	P_c (s)
Average	S3	0.0635	0.0008	0.0001	0.5735
	S4	0.0860	0.0024	0.0002	0.7362
Maximum	S3	0.2843	0.0101	0.0006	5.9874
	S4	0.7290	0.0242	0.0030	5.8934
Sweeps					
		T (s)	A (m^2/s^2)	M (m^2/s)	P_c (s)
Average	S3	0.0702	0.0016	0.0001	0.6343
	S4	0.0739	0.0039	0.0002	0.7314
Maximum	S3	0.4946	0.0248	0.0019	4.6619
	S4	0.3632	0.0581	0.0032	7.2679

the ejection events into more frequent ones but with less durability. The same observation can be made for maximum shear stress and transported momentum produced by ejection event.

Regarding sweep events, the parameters shown in Table 6.4 are consistent with those of ejection events. However, in the case of sweep events, they are less perturbed with the presence of mobile sediments in the near wall region.

Sweep events show the more important differences in their extreme values, being less dispersed around the parameters average.

(5) In the overlapping between pythmenic and hiporeic regions

At the reference point placed in the deepest trough, where pythmenic region overlaps the hiporeic region, there is a close resemblance to the previous reference point, (4,3). Regarding the ejection event, while the average values of duration and period present a light decrease from immobile to mobile sediment conditions, the values of maximum shear stress and transported momentum show a marked decrease.

The average values of the same parameters, from the sweep event, show also the same tendency, but not as marked as the ones from the ejection event. Table 6.5 shows that extreme values present the same tendency as average values.

Fig. 6.16 shows a decrease in the contribution of the ejection event to the shear stress production process with a marked deflection to the left when in bed load conditions. While the event durations and periodicity decreases, the same tendency is followed by the values of A and M, which results in a smaller contribution of this event to the total shear stress.

When analysing Fig. 6.17, regarding sweep events, there is a similar behaviour as described for ejections, but Table 6.5 proves that despite the decrease in duration and transported momentum of sweep events, it globally represents a less decrease or sometimes an increase in its contribution to shear stress production, through an increase in its frequency.

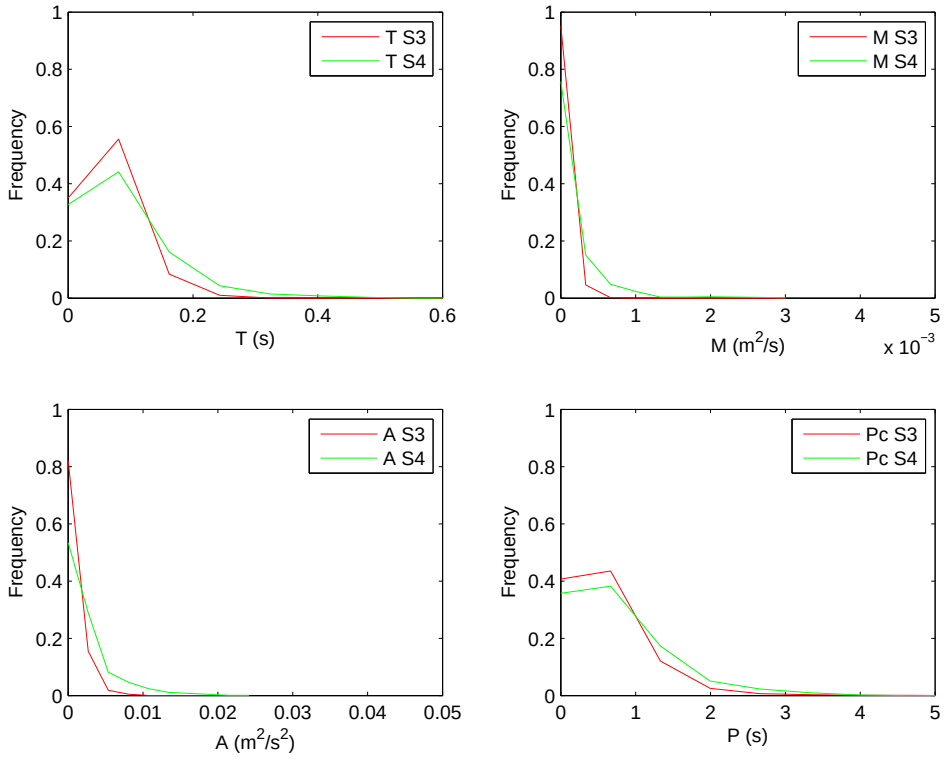

Figure 6.14: Histograms of duration (T), maximum shear stress (A), transported momentum (M) and period (P), of ejection events at reference point $(5, 3)$. Comparison of data sets S4, immobile bed in green and S3, mobile bed in red.

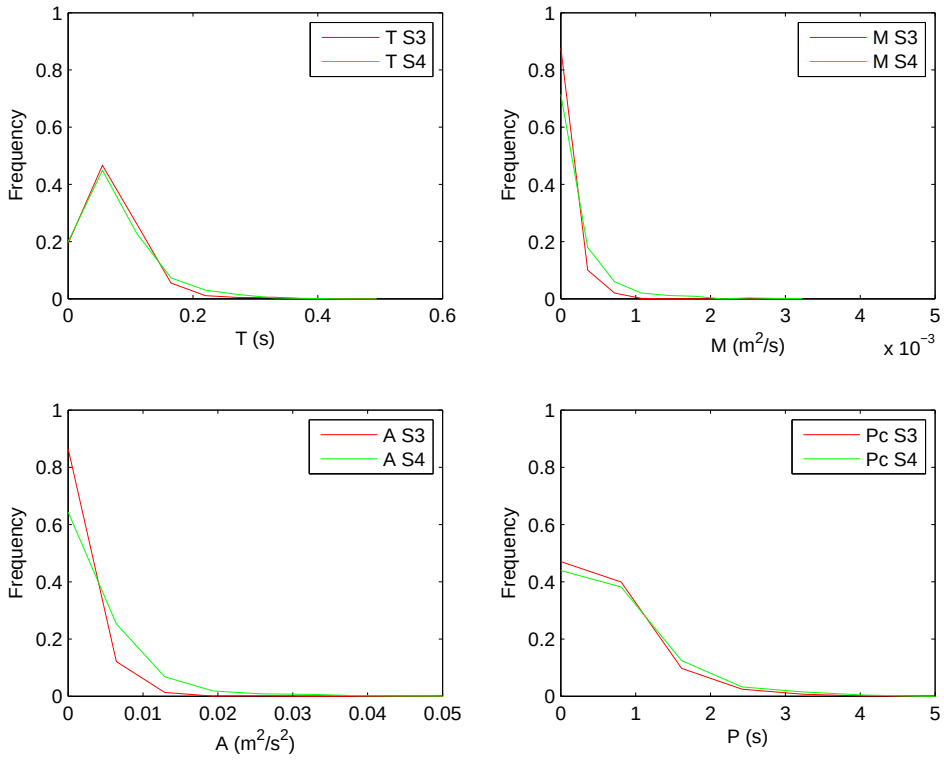

Figure 6.15: Histograms of duration (T), maximum shear stress (A), transported momentum (M) and period (P), of sweep events at reference point $(5, 3)$. Comparison of data sets S4, immobile bed in green and S3, mobile bed in red.

Tabela 6.5: Average and extreme values of the parameters calculated at reference point (5,4) in both mobile (S3) and immobile (S4) bed conditions. Where T represents the duration, A is the maximum shear stress, M is transported momentum and P is the period of events.

Reference point (5,4)					
Ejections					
		T (s)	A (m^2/s^2)	M (m^2/s)	P_c (s)
Average	S3	0.06149	0.00054	0.00002	0.51566
	S4	0.07535	0.00273	0.00014	0.71122
Maximum	S3	0.52436	0.00674	0.00050	9.53714
	S4	0.62511	0.02596	0.00277	4.50351
Sweeps					
		T (s)	A (m^2/s^2)	M (m^2/s)	P_c (s)
Average	S3	0.0727	0.0019	0.0001	0.5862
	S4	0.0798	0.0038	0.0002	0.7309
Maximum	S3	0.4631	0.0209	0.0018	6.4657
	S4	0.4763	0.0546	0.0042	5.3355

If comparing the average values of M between this reference position, $(5,2)$ and the one in the outer region, $(1,4)$ it confirms that while the near surface region is mainly governed by ejection events, the near wall region is governed by sweep events.

The experiment with mobile sediments shows that the sweep and ejection events are equally affected, however, the same is not valid for ejections, which are much more affected in the pythmenic region.

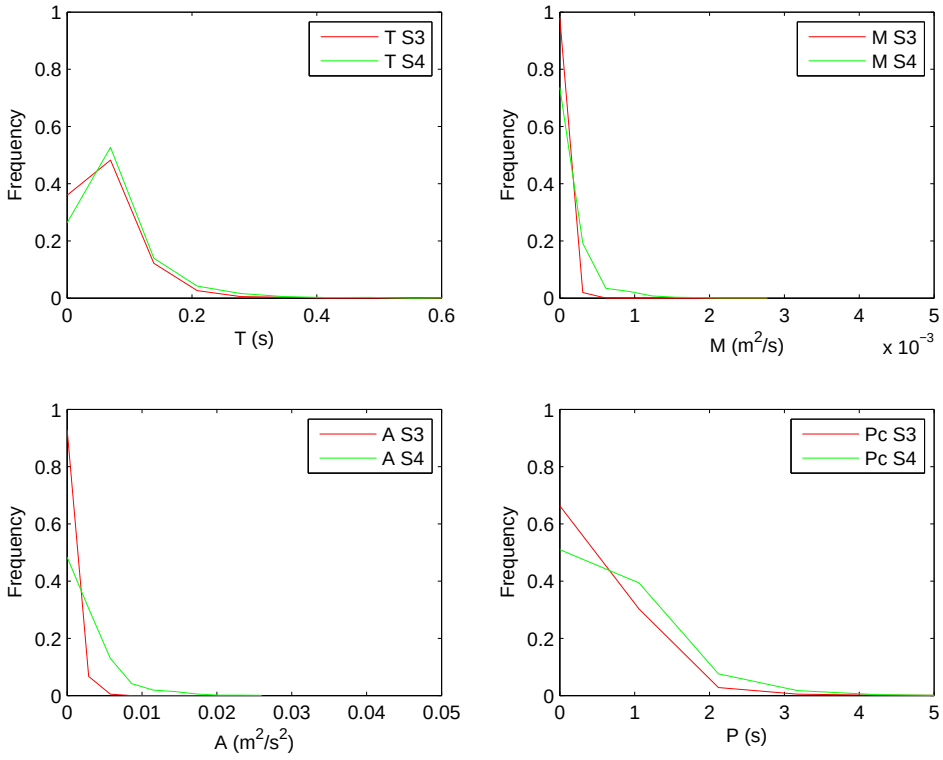

Figure 6.16: Histograms of duration (T), maximum shear stress (A), transported momentum (M) and period (P), of ejection events at reference point $(5,4)$. Comparison of data sets S4, immobile bed in green and S3, mobile bed in red.

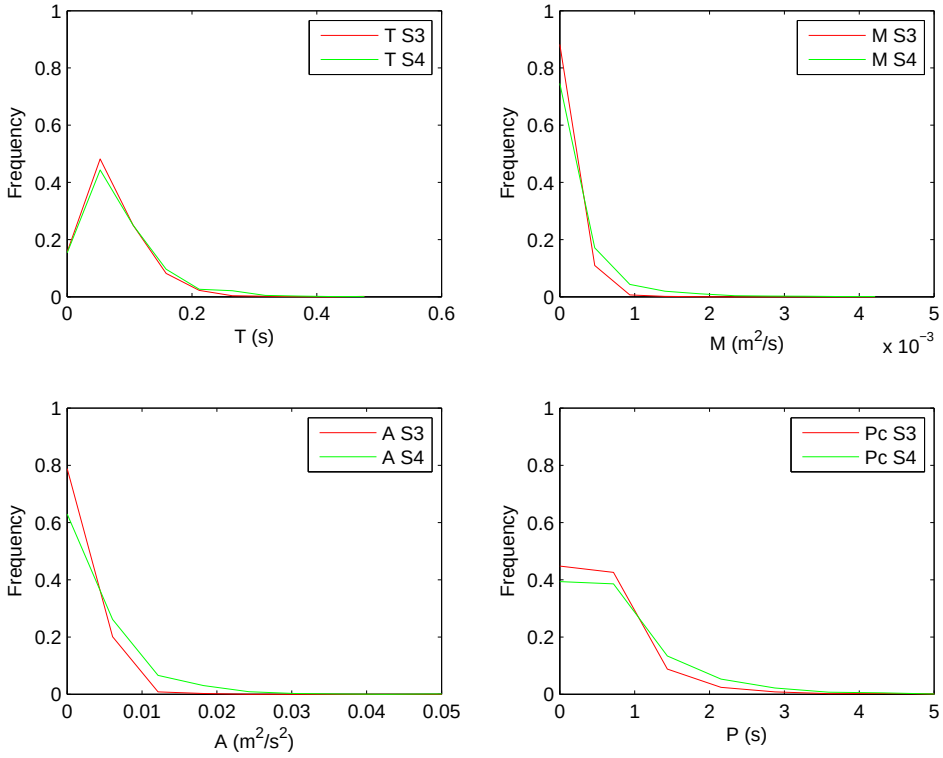

Figure 6.17: Histograms of duration (T), maximum shear stress (A), transported momentum (M) and period (P), of sweep events at reference point $(5,4)$. Comparison of data sets S4, immobile bed in green and S3, mobile bed in red.

6.4 Statistical analysis of non-dimensional parameters

Flow characteristics, such as, average shear stress, frictions velocity or even the mean flow velocity can induce differences between both tests, S4 and S3, respectively in immobile and mobile bed conditions. In order to help eliminating the effect of these variables which are particular characteristics of each test, a different approach is performed. This is turning the parameters that are between analysed, not dependent on these particular variables.

Thus, two distinct approaches are presented, as follows, where that same analysed parameters are normalized by two different basic variables.

In one hand, the parameters are normalized by $|\overline{u'w'}|$, the average shear stress at the particular reference position which is being analysed and, in the other hand, by the friction velocity, u^*, of that particular experiment, S4 or S3. Both experiments are also dependent on the distance to the wall, z, which is important to locate the analyses position in the structure of the flow.

The basic variable $|\overline{u'w'}|$, average shear stress, and z, distance to the wall, are chosen because using these variables to normalize the parameters, they make these parameters become independent on the characteristics that govern a generic flow in that region. Using these normalized parameters, any stand out in the flow characteristics is due to the mobile sediment presence and not due to its positioning in the flow structure. This allows to compare reference points within the same experiment, in this case S3.

On the contrary, using u^*, friction velocity, and z, distance to the wall, as basic variables, the differences between tests, in this case S4 and S3, become more perceptive. This approach is more indicated to highlight differences between tests S4 and S3, respectively immobile and mobile sediment conditions, keeping the same reference position in the flow structure.

As follows, the two described approaches are going to be performed, starting by presenting the normalization factors of each one and for the parameters that are being considered.

6.4.1 Normalized parameters based on the average shear stress, $|\overline{u'w'}|$, and z, distance to the wall

In this approach, equations 6.2, 6.1 and 6.3 represent that normalization factors, respectively for the maximum shear stress, A, transported momentum, M and period, P.

$$f_A = \frac{1}{|\overline{u'w'}|} \tag{6.1}$$

$$f_M = \sqrt{\frac{1}{|\overline{u'w'}| \times z^2}} \tag{6.2}$$

$$f_P = \frac{\sqrt{|\overline{u'w'}|}}{z} \tag{6.3}$$

where $|\overline{u'w'}|$ is achieved by calculating the absolute average value of shear stress at each specific reference point and z represents the distance from the reference point to the referential origin which is considered to be at the deepest point in the through.

A comparison is established between two reference positions, over the crest, $(3,2)$, and into

the through, $(5,4)$, respectively in Fig. 6.18 and Fig. 6.20 for ejection events and in Fig. 6.19 and Fig. 6.21 for sweep events.

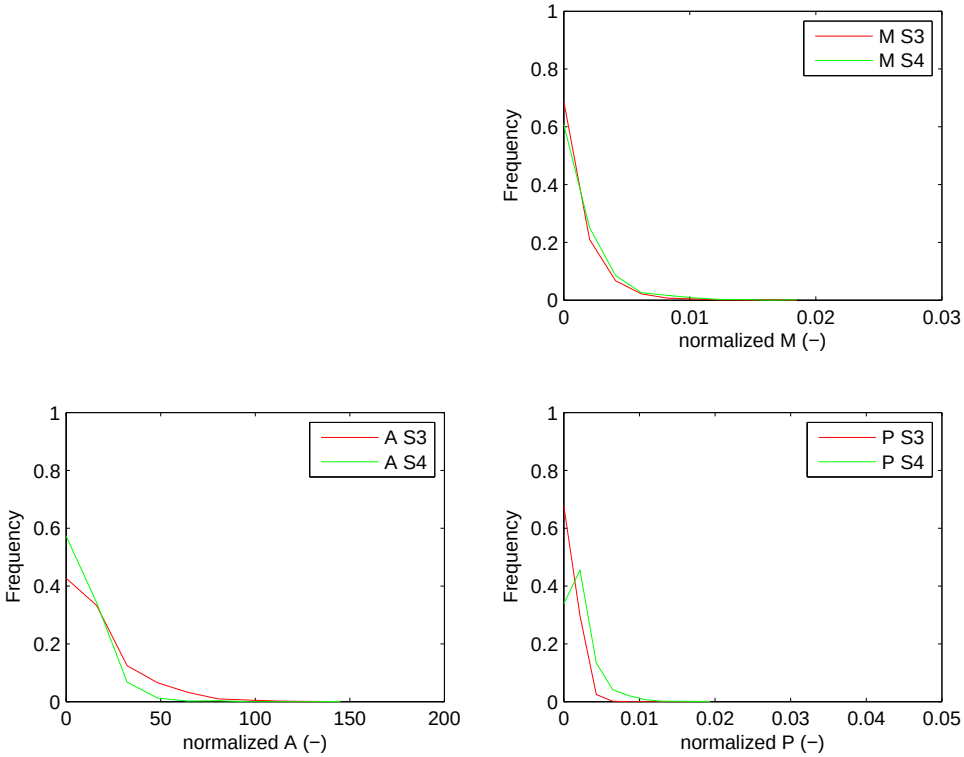

Figure 6.18: Histograms normalized using $|u'w'|$, average shear stress and z, distance to the wall, of duration (T), maximum shear stress (A), transported momentum (M) and period (P), of ejection events at reference point $(3,2)$. Comparison of data sets S4, immobile bed in green and S3, mobile bed in red.

For ejection events, in Fig. 6.18 and Fig. 6.20, the transported momentum presents a deflection to the left in the S3 curve, when comparing reference position $(3,2)$ to $(5,4)$, which indicates that into the through, events become of lower magnitude. However, the period of ejection events has exactly the same behaviour, which indicates that despite the lower transported momentum, interactions in the second quadrant become more frequent.

For sweep events, in Fig. 6.19 and Fig. 6.21, the transported momentum curve deflects slightly to the right at reference position $(5,4)$, showing that mobile sediment transport in the vicinity of the wall is more controlled by sweep events. The period also deflects to the left, for S3 at reference position $(5,4)$, indicating that the mobile sediment makes the sweep events more frequent.

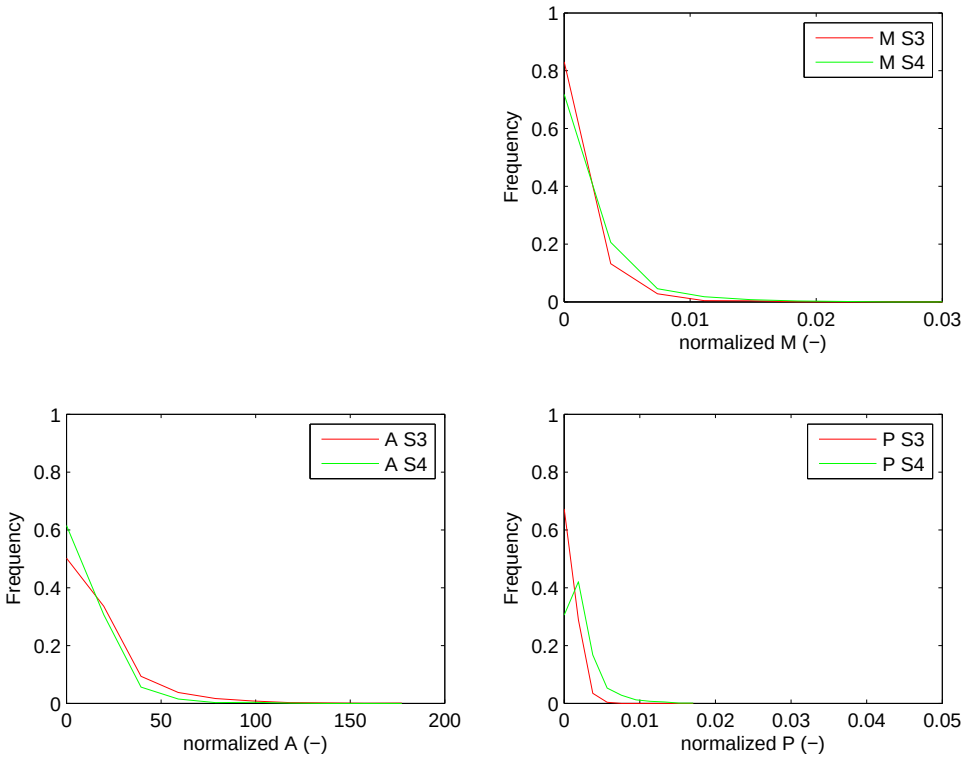

Figure 6.19: Histograms normalized using $|u'w'|$, average shear stress and z, distance to the wall, of duration (T), maximum shear stress (A), transported momentum (M) and period (P), of sweep events at reference point $(3,2)$. Comparison of data sets S4, immobile bed in green and S3, mobile bed in red.

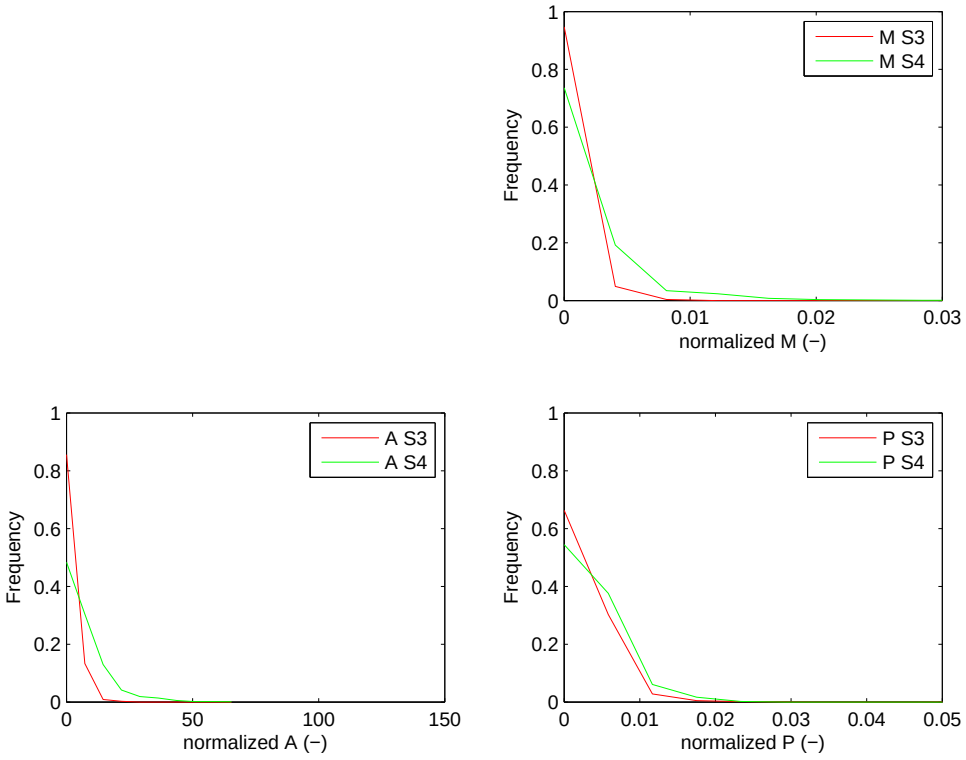

Figure 6.20: Histograms normalized using $|u'w'|$, average shear stress and z, distance to the wall, of duration (T), maximum shear stress (A), transported momentum (M) and period (P), of ejection events at reference point $(5,4)$. Comparison of data sets S4, immobile bed in green and S3, mobile bed in red.

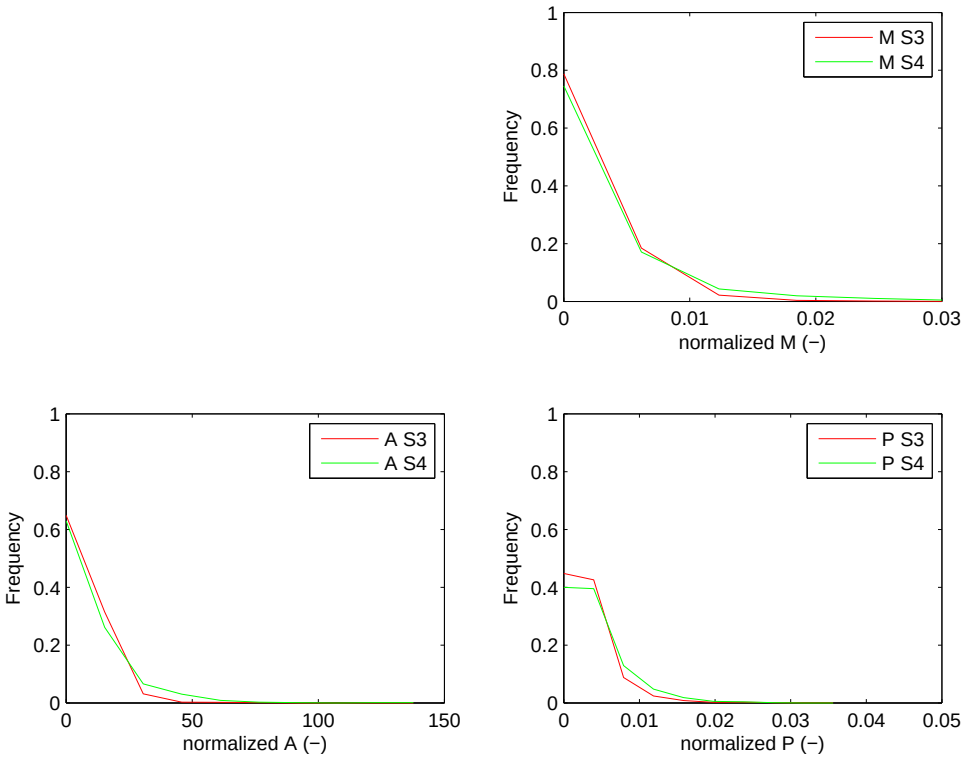

Figure 6.21: Histograms normalized using $|u'w'|$, average shear stress and z, distance to the wall, of duration (T), maximum shear stress (A), transported momentum (M) and period (P), of sweep events at reference point $(5,4)$. Comparison of data sets S4, immobile bed in green and S3, mobile bed in red.

6.4.2 Normalized parameters based on friction velocity, u^*, and z, distance to the wall

The normalization factors, in this case, are calculated as presented in equations 6.5, 6.4 and 6.6, respectively to normalize the maximum shear stress, A, transported momentum, M, and period, P.

$$f_{A^*} = \frac{1}{(u^*)^2} \tag{6.4}$$

$$f_{M^*} = \frac{1}{u^* \times z} \tag{6.5}$$

$$f_{P^*} = \frac{u^*}{z} \tag{6.6}$$

The histograms achieved for these normalized parameters are analysed, aiming to improve its comprehension by establishing a comparison between immobile and mobile bed conditions in the through region and using both reference points (5,3) and (5,4) that are placed in the same through.

Although the results of this analyses in normalized parameters are not very different from the ones made using parameters in their real values, these two reference positions are presented because it is where the greatest differences are noticed.

These reference positions are respectively presented, for ejection events in Fig. 6.22 and Fig. 6.24, and for sweep events in Fig. 6.23 and Fig. 6.25.

By comparing these results to those presented in sub-chapter 6.3, at the same reference positions, it is noticed that in normalized parameters they seem to show a slight convergence between immobile and mobile bed conditions. This indicates that the effect of sediment transport as bed load may be less expressive than it is shown in the parameters real values and this is valid to both ejection and sweep events.

The major differences are noticed over the period, in both ejection and sweep events and for both reference positions $(5,3)$ and $(5,4)$.

It is also noticed that specially in the case of sweep events, when in mobile bed conditions, the period curve slightly deflects to the right relatively to the same curve in the case of immobile bed conditions, as shown in Fig. 6.23 and Fig. 6.25.

This behaviour indicates that in mobile bed conditions, the frequency of sweep events in the near wall region decreases, which is not consistent with previous results, obtained for parameters in their real values, as shown in Fig. 6.15 and Fig. 6.17.

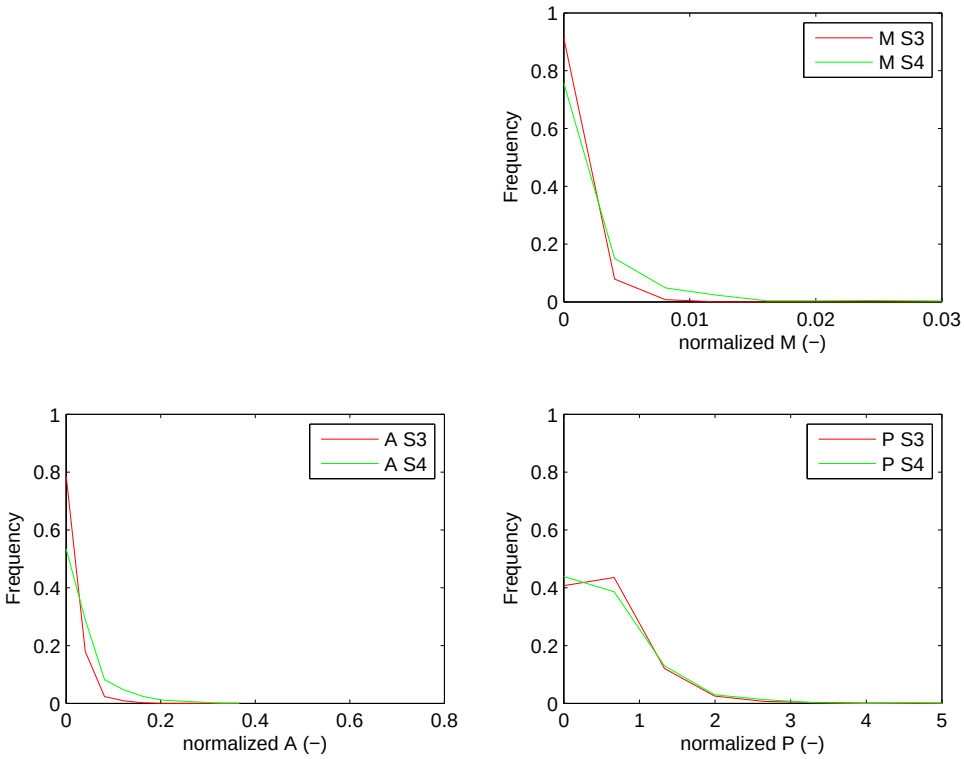

Figure 6.22: Histograms normalized using u^*, friction velocity and z, distance to the wall, of duration (T), maximum shear stress (A), transported momentum (M) and period (P), of ejection events at reference point $(5,3)$. Comparison of data sets S4, immobile bed in green and S3, mobile bed in red.

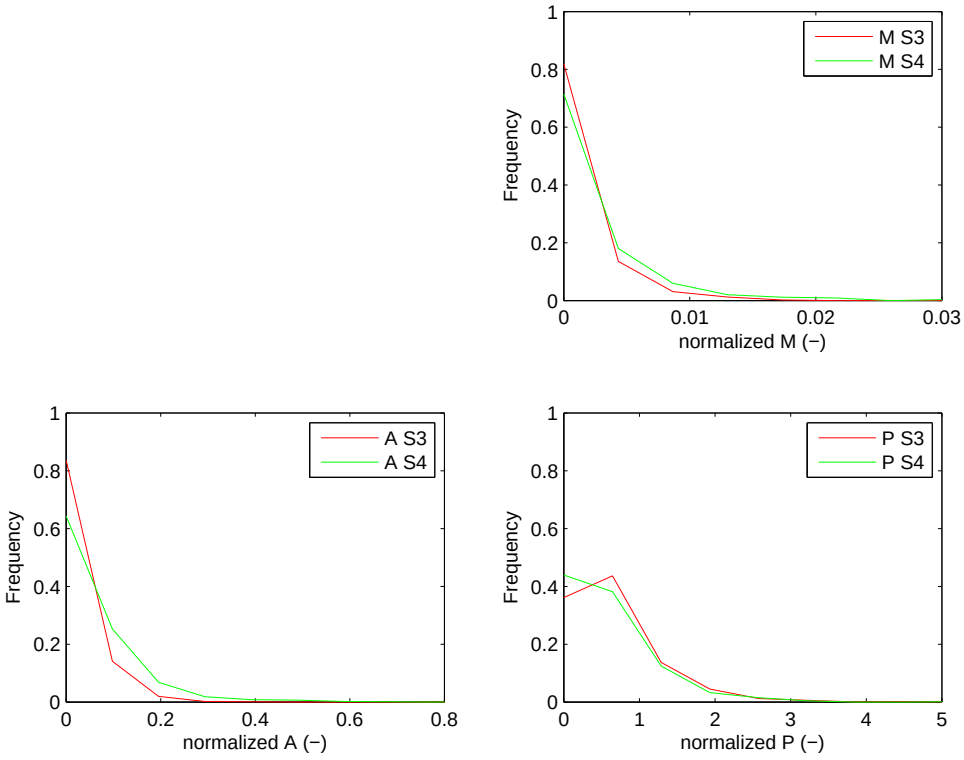

Figure 6.23: Histograms normalized using u^*, friction velocity and z, distance to the wall, of duration (T), maximum shear stress (A), transported momentum (M) and period (P), of sweep events at reference point $(5,3)$. Comparison of data sets S4, immobile bed in green and S3, mobile bed in red.

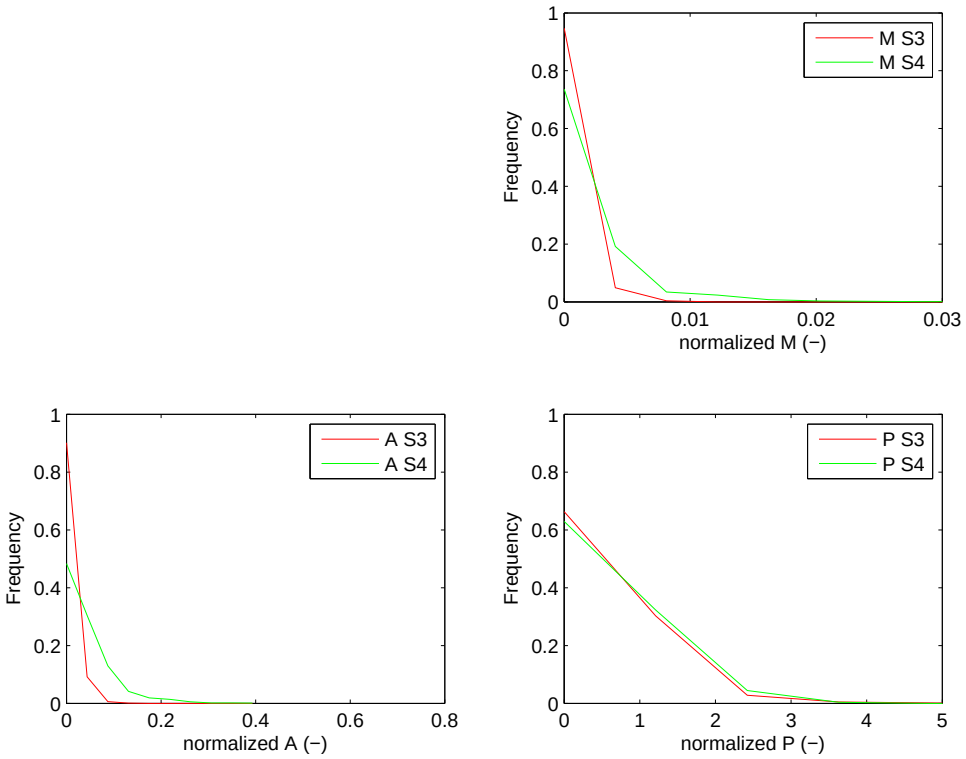

Figure 6.24: Histograms normalized using u^*, friction velocity and z, distance to the wall, of duration (T), maximum shear stress (A), transported momentum (M) and period (P), of ejection events at reference point $(5,4)$. Comparison of data sets S4, immobile bed in green and S3, mobile bed in red.

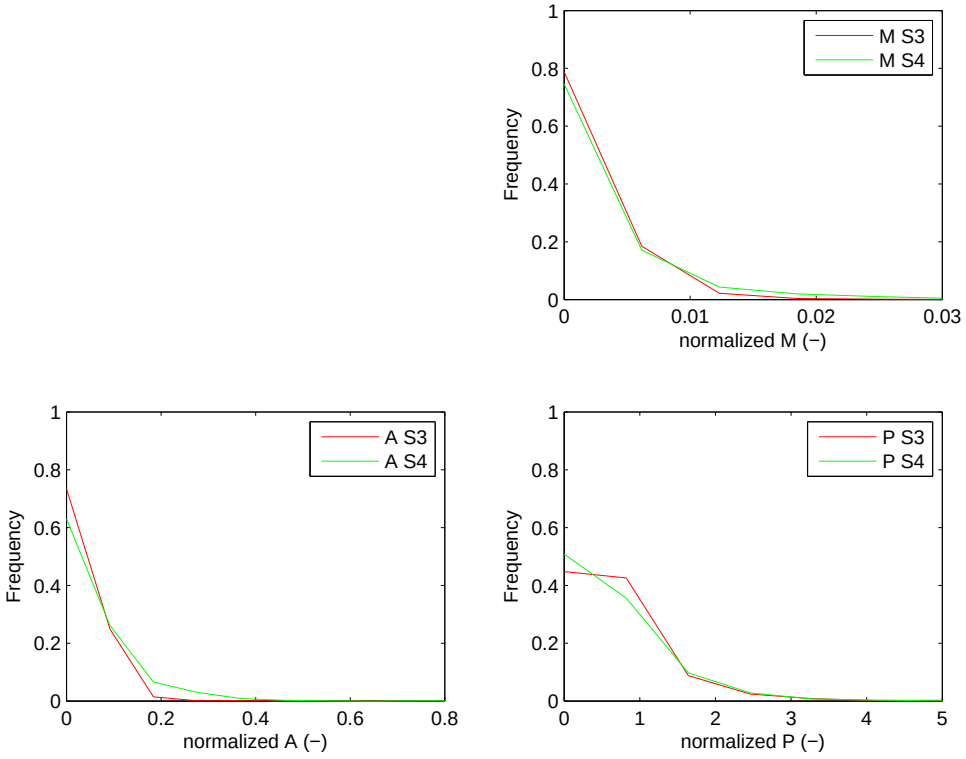

Figure 6.25: Histograms normalized using u^*, friction velocity and z, distance to the wall, of duration (T), maximum shear stress (A), transported momentum (M) and period (P), of sweep events at reference point $(5,4)$. Comparison of data sets S4, immobile bed in green and S3, mobile bed in red.

Chapter 7

Conclusions and further developments

The analysis of the laboratorial data, including instantaneous flow velocity fields, were considered to evaluate the effect of sediment transport in the near-bed region over the coherent structures that characterize the flow. The two tests were performed in conditions of open-channel flow with porous rough bed and poorly sorted gravel-sand mixture.

The data was processed by apply the quadrant analysis method, leading to an approach through the statistics of the duration, maximum shear stress, transported momentum and period of each event.

The use of normalized parameters introduces improvements in the understanding of these statistics aiming at eliminating, in one hand, the particular characteristics of both tests, using friction velocity and distance to the wall, and in the other hand, the particular characteristics of the flow at the specific reference point, using the average shear stress in that position and the distance to the wall.

The discussion of these results lead to the following main conclusions:

- In the overlapping layer, between inner and pythmenic regions, which stands over the crest, the flow tends to be isotropic in mobile bed conditions. The events are equally distributed between the four quadrants and share responsibilities in the processes of shear stress production;

- In the pythmenic region, standing into the through, mobile bed conditions lead to a situation where ejection and sweep events are responsible for the shear stress production processes with sweep events assuming the a main role, in opposition to the situation in the upper regions of the flow;

- Generally, the sediment transport of sand decreases the transported momentum and maximum shear stress values but increases their frequency of occurrence in time;

- The analysis of the probability distribution function (pdf) of both ejections and sweeps, especially in the pythmenic region, it is apparent that the effect of sediment transport is the reduction of the frequency of large events and the increase of the frequency of small events. This may be due to breaking of eddy coherence by sediment motion;

- Scaling the pdf with local variables indicates that, in the same location, mean shear stress may vary due to sediment transport. In that case, the larger magnitude of large events without bedload motion may be a consequence of the overall greater local shear stress under those conditions;

- It is also concluded that the ejection events suffer the more important decreases due to sediment transport in the near bed region. This happens generally in the pythmenic region.

Further studies must be performed in the scope of this thesis. Having that in mind, some suggestions for future developments in this same subject are presented as follows.

The study of the same parameters may be undertaken in a different approach, for example, studying statistics over the two-dimensional maps, instead of isolated reference points. The use of double-average technique, mainly in the interception between inner and outer layer, may lead to interesting results. This can bring a more wide approach that is suitable of revealing interesting results to complement those presented in this thesis.

Improving the filtering method, which in this case was the Phase-Space thresholding method, adapted for PIV measurements. This can be made by extending the substitution criteria to both components of instantaneous velocity once a spurious point in identified. Currently, the process is performed independently between both velocity orthogonal components.

Perform experiments in other planes across the width of the flume. This approach can roughly lead to build horizontal maps of instantaneous velocity, enabling the possibility to study the flow in the cross section too.

The bed roughness has an effect over the moving particles and it would be interesting to perform the same study in different bed conditions.

"In situ" experiments are always interesting and at the same time difficult to perform. It would be interesting to acquire some data in these conditions to compare with the results of this dissertation.

The flow rate is one of the variables that would be interesting to change, specially if it could be used the same value in both tests. It would improve the information given by dimensional results avoiding to use normalized parameters.

Other variables can be studied, such as, changing the sediment transport quantity introduced in the flow.

The use of 2 CCD cameras in future experiments, may introduce a third component in the flow velocity maps. It would improve the available data quantity and quality, allowing to study the flow in three dimensions. It would also be interesting because of the fact that the data would

result from the same experiment in the three orthogonal directions and acquired at the same time and conditions, in opposition to the data which is available comprising flow velocity maps in two dimensions at different vertical planes.

Bibliography

Amatruda, M. (2009). Effects of sediment transport in gravel-bedded rivers. Master's thesis, Universita degli study di Napoli - Frederico II, Napoli.

Campbell, L. J. (2005). *Double-Averaged open-channel flow over regular rough beds*. Ph. D. thesis, University of Aberdeen, Aberdeen.

Chao, B. T. (1964). Turbulent transport behaviour of small particles in a turbulent fluid. *Osterreichisches Ingenieur-Archiv 18*(7).

Corino, E. R. and R. S. Brodkey (1969). A visual investigation of the wall region in turbulent flow. *Journal of Fluid Mechanics 37*(01), 1–30.

Dawson, T. P., N. Butt, and F. Miller (2002). The ecology of forest fires. *ASEAN Biodiversity 1*, 18–21.

Ferreira, L. S. M. (2008). Impact of sediment overfeeding in gravel-bedded river's salmonid habitats. Master's thesis, Instituto Superior Técnico - Universidade Técnica de Lisboa, Lisboa.

Ferreira, R. L., L. M. Ferreira, A. M. Ricardo, and M. J. Franca (2010). Impacts of sand transport on flow variables and dissolved oxygen in gravel-bed streams suitable salmonid spawning. *River Research and Applications 26*(10), 414–438.

Ferreira, R. M. L. (2011). Turbulent flow hydrodynamics and sediment transport. laboratory research with lda and piv. In P. R. E. (in press) (Ed.), *Experimental methods and techniques in hydraulic research*.

Ferreira, R. M. L., M. J. Franca, and J. G. A. B. Leal (2008). Flow resistance in open-channel flows with mobile hydraulically rough beds. In *River Flow 2008 - Vol. 1*, pp. 385–394.

Ferreira, R. M. L., M. J. Franca, J. G. A. B. Leal, and A. H. Cardoso (2012). Flow over rough mobile beds: Friction factor and vertical distribution of the longitudinal mean velocity. *Water Resources Research 48*(W011126).

Ferreira, R. M. L., M. J. Franca, J. G. B. Leal, and A. H. Cardoso (2009). Organized turbulence over mobile and immobile hydraulically rough boundaries. In *35rd IAHR Congress*, Vancouver, British Columbia, Canada, pp. 36–43. IAHR.

Goring, D. G. and V. I. Nikora (2002). Despiking acoustic doppler velocimeter data. *Journal of Hydraulic Engineering 28*(1), 117–126.

Grass, A. J. (1971). Structural features of turbulent flow over smooth and rough boundaries. *Journal of Fluid Mechanics 50*(02), 233–255.

Gyr, A. and A. Schmid (1997). Turbulent flows over smooth erodible sand beds in flumes. *Journal of Hydraulic Research 35*(4), 525–544.

Hjemfelt, A. T. and L. F. Mockros (1996). Motion of discrete particles in a turbulent fluid. *Applied Science Research 16*, 149–161.

Kim, H. T., S. J. Kline, and W. C. Reynolds (1971). The production of turbulence near a smooth wall in a turbulent boundary layer. *Journal of Fluid Mechanics 50*(01), 133–160.

Kline, S. J., W. C. Reynolds, F. A. Schraub, and P. W. Runstadler (1967). The structure of turbulent boundary layers. *Journal of Fluid Mechanics 30*(04), 741–773.

Lory, J. (2011). Estudo laboratorial de escoamentos em leitos com vegeta(c)ão emersa e rígida. Master's thesis, Faculdade de Ciências e Técnologia - Universidade Nova de Lisboa, Lisbon.

Lu, S. S. and W. W. Willmarth (1973). Measurements of the structure of the reynolds stress in a turbulent boundary layer. *Journal of Fluid Mechanics 60*(03), 481–511.

Melling, A. (1997). Tracer particles and seeding for particle image velocimetry. *Measurement Science and Technology 8*, 1406–1416.

Nakagawa, H. and I. Nezu (1977). Prediction of the contributions to the reynolds stress from bursting events in open-channel flows. *Journal of Fluid Mechanics 80*(01), 99–128.

Nezu, I. and H. Nakagawa (1993). *Turbulence in Open-Channel Flows*, Volume Monograph Series. Balkema, Rotterdam: International Association for Hydraulic Research.

Nikora, V., D. Goring, I. McEwan, and G. Griffiths (2001). Spatially averaged open-channel flow over rough bed. *Journal of Hydraulic Engineering 127*(2), 123–133.

Nogueira, H. (2007). Pilares de pontes em leitos móveis. Master's thesis, Instituto Superior Técnico - Universidade Técnica de Lisboa, Lisboa.

Prasad, A. K. (2000). Particle image velocimetry. *Current Science Association - Indian Academy of Sciences 79*(1).

Raffel, M., C. E. Willert, and J. Kompenhans (1998). *Particle Image Velocimetry: A Pratical Guide*. Germany: Springer.

Raupach, M. R., R. A. Antonia, and S. Rajagopalan (1991). Rough-wall turbulent boundary layers. *Appl. Mech. Rev. 44*(1), 1–25.

Ricardo, A. M. C. (2008, Dezembro). Caracterização do escoamento turbulento em canais com vegetação emersa rígida. aplicação ao estudo da resistẽncia hidráulica. Master's thesis, Instituto Superior Técnico - Universidade Técnica de Lisboa, Lisboa.

Schlichting, H. (1968). *Boundary - Layer Theory* (6th ed.). McGraw Hill.

Sechet, P. and B. Le Guennec (1999). Bursting phenomenon and incipient motion of solid particles in bed-load transport. *Journal of Hydraulic Research 37*(5), 683–696.

Simão, J. G., A. M. Ricardo, and R. M. L. Ferreira (2009). Análise de sensibilidade a medições piv para a caracterização de escoamentos hidraulicamente rugosos com moderada submersão relativa. In *3a Conferência Nacional em Mecânica de Fluidos, Termodinâmica e Energia*.

Sveen, J. K. and E. A. Cowen (2004). *Quantitive Imaging Techniques and Their Applications to Waavy Flows*. Chapter 1. University of Oslo, Norway.

Tropea, C., A. Yarin, and J. Foss (2007). *Springer handbook of experimental fluid mechanics*. Springer Verlag.

Wereley, S. T. and C. D. Meinhart (2000). Accuracy improvements in particle image velocimetry algorithms. In *10th International Symposium on Applications of Laser Techniques to Fluid Mechanics*. Fundação Calouste Gulbenkian - Centro de Estudos em Inovação, Tecnologia e Políticas de Desenvolvimento (IST). (available at http://in3.dem.ist.utl.pt/conflaser/).

Westerweel, J. (1997). The effect of a discrete window offset on the accuracy of cross-correlation analysis of digital piv recordings. *Experiments in Fluids 23*, 20–28.

Willmarth, W. W. and S. S. Lu (1972). Structure of the reynolds stress near the wall. *Journal of Fluid Mechanics 55*(01), 65–92.

Appendix A

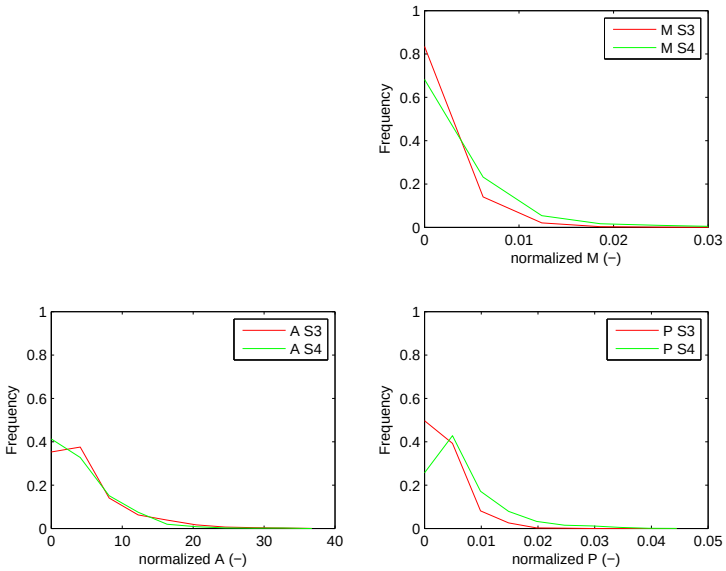

(a) Ejection events

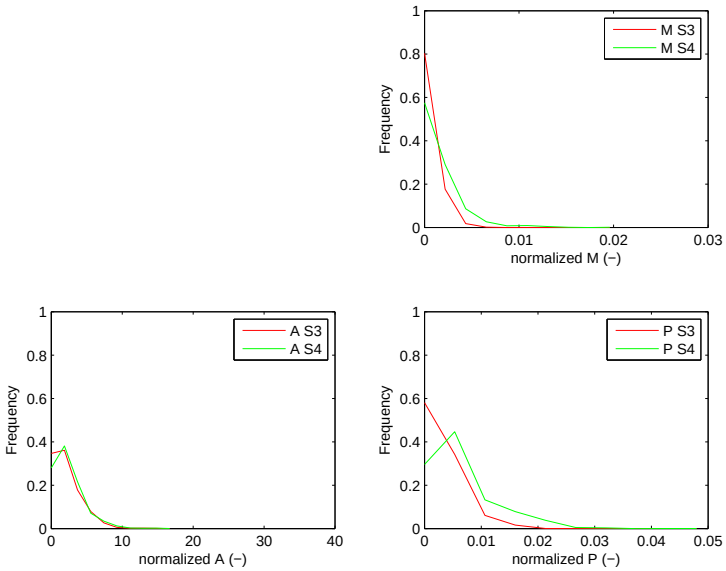

(b) Sweep events

Figure A.1: Histograms normalized using $|u'w'|$, average shear stress and z, distance to the wall, of duration (T), maximum shear stress (A), transported momentum (M) and period (P), of ejection and sweep events at reference point $(1,4)$. Comparison of data sets S4, immobile bed in green and S3, mobile bed in red.

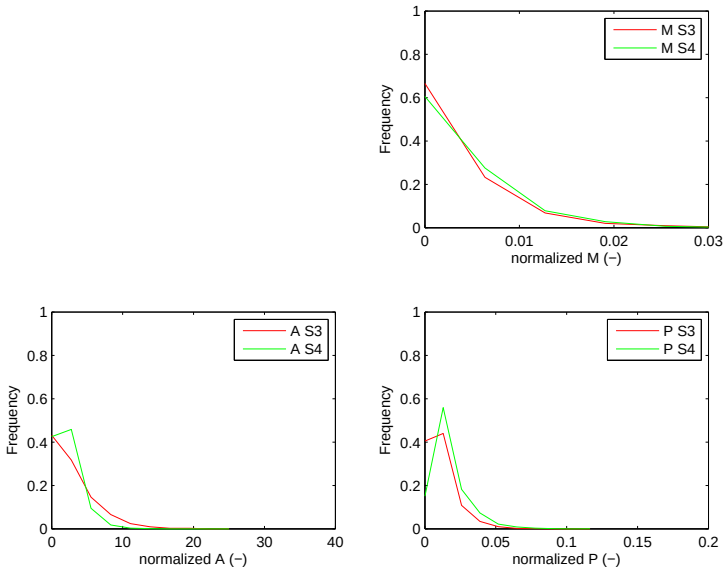

(a) Ejection events

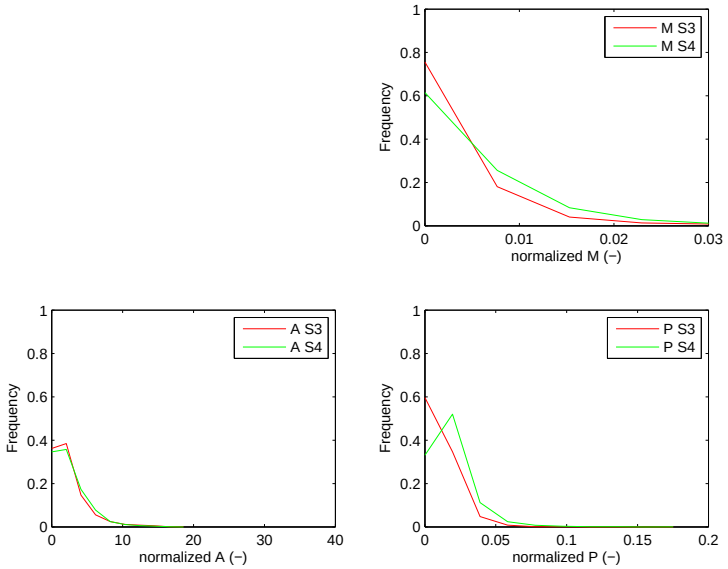

(b) Sweep events

Figure A.2: Histograms normalized using $|u'w'|$, average shear stress and z, distance to the wall, of duration (T), maximum shear stress (A), transported momentum (M) and period (P), of ejection and sweep events at reference point $(3,3)$. Comparison of data sets S4, immobile bed in green and S3, mobile bed in red.

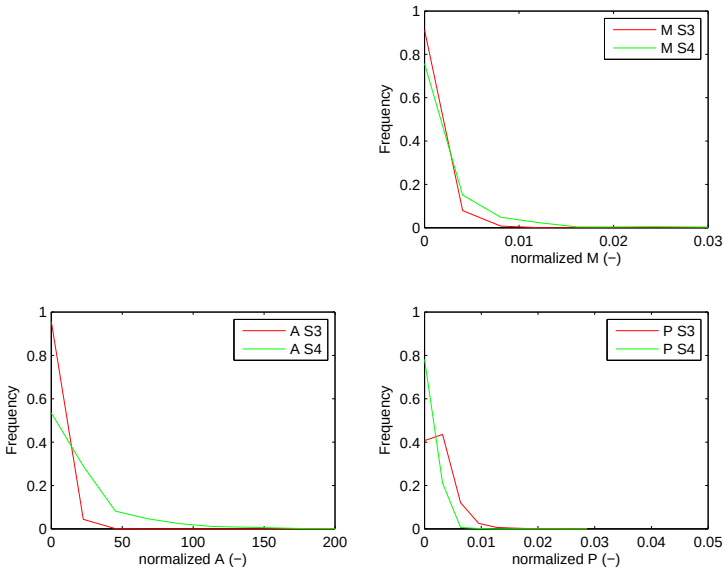

(a) Ejection events

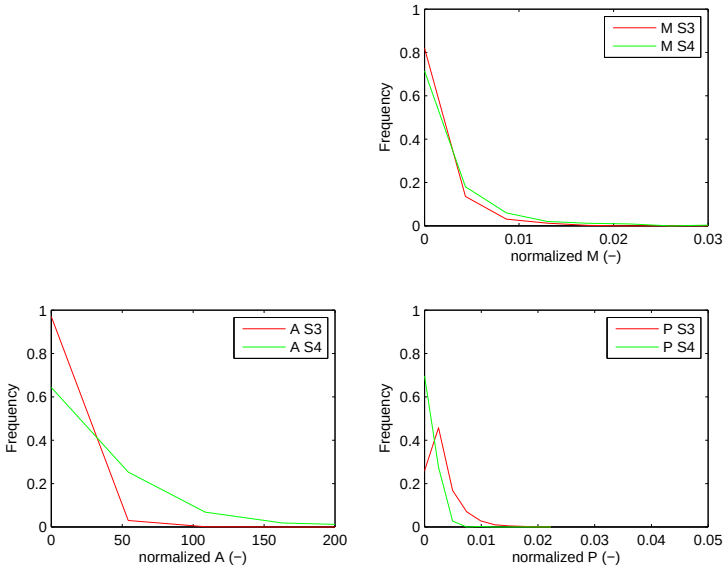

(b) Sweep events

Figure A.3: Histograms normalized using $|u'w'|$, average shear stress and z, distance to the wall, of duration (T), maximum shear stress (A), transported momentum (M) and period (P), of ejection and sweep events at reference point $(5,3)$. Comparison of data sets S4, immobile bed in green and S3, mobile bed in red.

Appendix B

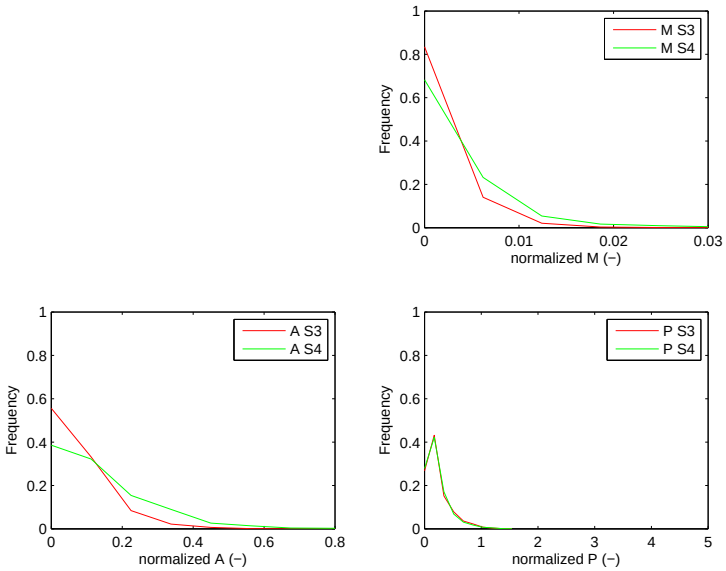

(a) Ejection events

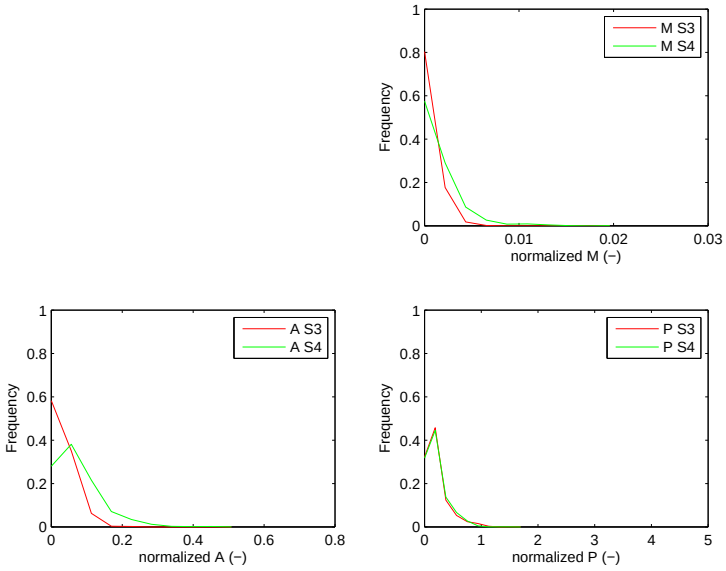

(b) Sweep events

Figure B.1: Histograms normalized using u^*, friction velocity and z, distance to the wall, of duration (T), maximum shear stress (A), transported momentum (M) and period (P), of ejection and sweep events at reference point $(1,4)$. Comparison of data sets S4, immobile bed in green and S3, mobile bed in red.

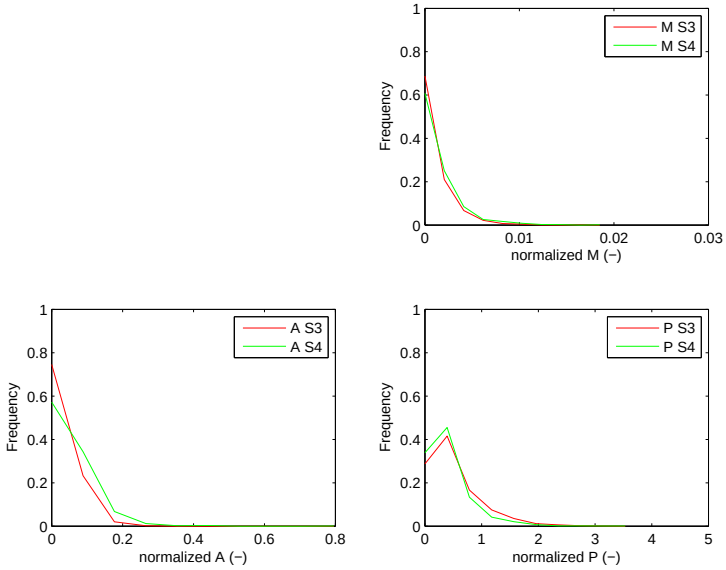

(a) Ejection events

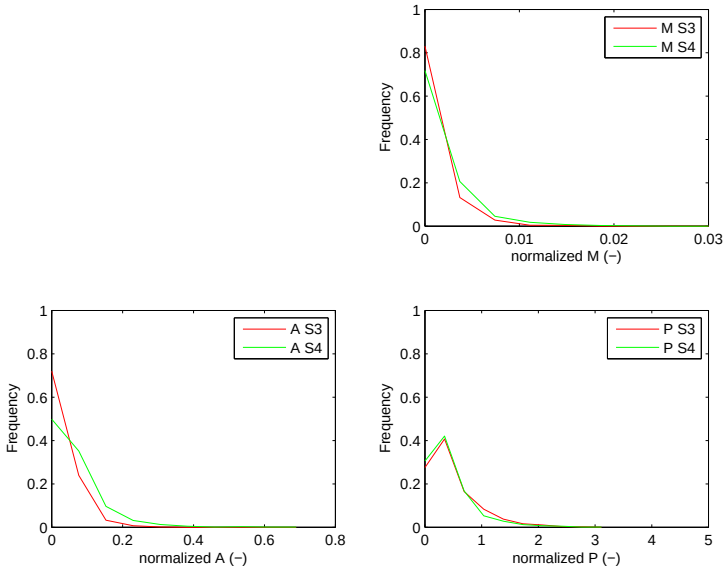

(b) Sweep events

Figure B.2: Histograms normalized using u^*, friction velocity and z, distance to the wall, of duration (T), maximum shear stress (A), transported momentum (M) and period (P), of ejection and sweep events at reference point $(3, 2)$. Comparison of data sets S4, immobile bed in green and S3, mobile bed in red.

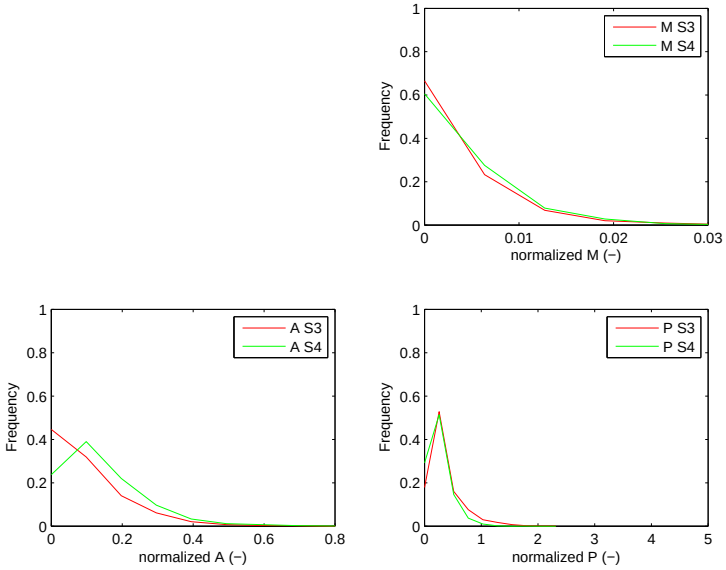

(a) Ejection events

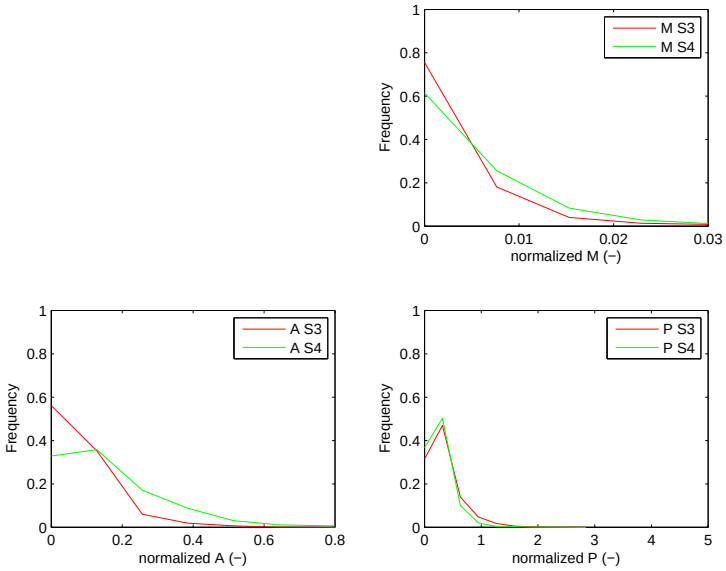

(b) Sweep events

Figure B.3: Histograms normalized using u^*, friction velocity and z, distance to the wall, of duration (T), maximum shear stress (A), transported momentum (M) and period (P), of ejection and sweep events at reference point $(3, 3)$. Comparison of data sets S4, immobile bed in green and S3, mobile bed in red.